Space Sci Rev (2013) 174:49–111
DOI 10.1007/s11214-012-9948-3

Long-Term Evolution of the Martian Crust-Mantle System

M. Grott · D. Baratoux · E. Hauber · V. Sautter · J. Mustard · O. Gasnault · S.W. Ruff · S.-I. Karato · V. Debaille · M. Knapmeyer · F. Sohl · T. Van Hoolst · D. Breuer · A. Morschhauser · M.J. Toplis

Received: 24 April 2012 / Accepted: 2 November 2012 / Published online: 30 November 2012

Abstract Lacking plate tectonics and crustal recycling, the long-term evolution of the crust-mantle system of Mars is driven by mantle convection, partial melting, and silicate differentiation. Volcanic landforms such as lava flows, shield volcanoes, volcanic cones, pyroclastic deposits, and dikes are observed on the martian surface, and while activity was widespread during the late Noachian and Hesperian, volcanism became more and more restricted to the Tharsis and Elysium provinces in the Amazonian period. Martian igneous rocks are predominantly basaltic in composition, and remote sensing data, in-situ data, and analysis of the SNC meteorites indicate that magma source regions were located at depths between 80

M. Grott (✉) · E. Hauber · M. Knapmeyer · F. Sohl · D. Breuer · A. Morschhauser
Institute of Planetary Research, German Aerospace Center, Rutherfordstr. 2, 12489 Berlin, Germany
e-mail: matthias.grott@dlr.de

D. Baratoux · O. Gasnault · M.J. Toplis
Institut de Recherche en Astrophysique et Planétologie, Université Toulouse III, Toulouse, France

D. Baratoux
e-mail: david.baratoux@irap.omp.eu

V. Sautter
Département Histoire de la Terre Muséum National d'Histoire Naturelle, Paris, France

J. Mustard
Department of Geological Sciences, Brown University, Providence, RI 02912, USA

S.W. Ruff
School of Earth and Space Exploration, Arizona State University, Tempe, AZ, USA

S.-I. Karato
Department of Geology and Geophysics, Yale University, New Haven, CT, USA

V. Debaille
Laboratoire G-Time, Université Libre de Bruxelles, 1050 Brussels, Belgium

T. Van Hoolst
Royal Observatory of Belgium, Brussels, Belgium

and 150 km, with degrees of partial melting ranging from 5 to 15 %. Furthermore, magma storage at depth appears to be of limited importance, and secular cooling rates of 30 to 40 K Gyr^{-1} were derived from surface chemistry for the Hesperian and Amazonian periods. These estimates are in general agreement with numerical models of the thermo-chemical evolution of Mars, which predict source region depths of 100 to 200 km, degrees of partial melting between 5 and 20 %, and secular cooling rates of 40 to 50 K Gyr^{-1}. In addition, these model predictions largely agree with elastic lithosphere thickness estimates derived from gravity and topography data. Major unknowns related to the evolution of the crust-mantle system are the age of the shergottites, the planet's initial bulk mantle water content, and its average crustal thickness. Analysis of the SNC meteorites, estimates of the elastic lithosphere thickness, as well as the fact that tidal dissipation takes place in the martian mantle indicate that rheologically significant amounts of water of a few tens of ppm are still present in the interior. However, the exact amount is controversial and estimates range from only a few to more than 200 ppm. Owing to the uncertain formation age of the shergottites it is unclear whether these water contents correspond to the ancient or present mantle. It therefore remains to be investigated whether petrologically significant amounts of water of more than 100 ppm are or have been present in the deep interior. Although models suggest that about 50 % of the incompatible species (H_2O, K, Th, U) have been removed from the mantle, the amount of mantle differentiation remains uncertain because the average crustal thickness is merely constrained to within a factor of two.

Keywords Mars · Volcanism · Geophysics · Geochemistry

1 Introduction

Following accretion and core formation, Mars may have been initially covered by a magma ocean, which would have crystallized within 50 Myr (Elkins-Tanton et al. 2003, 2005). The gravitationally driven overturn of unstably stratified magma ocean cumulates would then result in the formation of partial melts, thereby forming the 20–30 km thick primary crust of the planet (Halliday et al. 2001; Nyquist et al. 2001; Norman 1999) and establishing the primary geochemical reservoirs of the martian interior. The formation of these reservoirs (primary crust, primordial mantle, and core) is covered elsewhere in this volume (Mezger et al. 2012, this issue), and we will focus here on the evolution of the crust-mantle system on longer time-scales. In the absence of plate tectonics and crustal recycling, reservoir differentiation should be mainly driven by partial melting of the mantle. Indeed, the martian surface shows abundant evidence for the longstanding volcanic history of the planet.

The martian surface record is well preserved, and accessible surface units cover the timespan from the early Noachian around 4.2 Gyr ago to relatively young surfaces (Tanaka 1986; Neukum et al. 2004) which show cratering model ages of less than 10 Myr. While activity was widespread and essentially global in nature during the early evolution, very young volcanic surfaces are only observed in the Tharsis and Elysium volcanic provinces (Werner 2009).

Data to constrain the details of mantle differentiation come from a variety of sources, and the task of unraveling the magmatic history of the planet is truly multidisciplinary. Topography and image data at large scales are essential to identify and map the extent of volcanic provinces, and to estimate magma production rates as a function of time. Images with a

spatial resolution of up to decimeter scale (Jaumann et al. 2007; Malin et al. 2007; McEwen et al. 2007) may be used to characterize eruption parameters (e.g., presence of volatiles, lava rheology, effusion rates), and allow for the study of the geomorphological characteristics of volcanically emplaced surfaces in great detail. Mineralogical information based on spectroscopic images is available with resolutions of 100 m/pixel (Christensen et al. 2003; Bibring et al. 2006; Murchie et al. 2007), reaching 18 m/pixel in selected areas (Mustard et al. 2008), while observations in the infrared add a dataset with a resolution of 3×6 km per pixel (Bandfield et al. 2000). Furthermore, gamma ray spectroscopy (Boynton et al. 2007) constrains the elemental abundances of various elements, allowing for an estimation of the SiO_2 content of surface rocks (Boynton et al. 2007). This information is complemented by data obtained in-situ from the Mars exploration rovers, which performed chemical as well as mineralogical investigations (Squyres et al. 2004a, 2004b), as well as Mars Pathfinder (Rieder et al. 1997) and the Phoenix lander (Boynton et al. 2009).

Further information on the lithologies of martian igneous rocks comes from the Shergottite, Nahklite, Chassignite (SNC) clan of meteorites, generally accepted to come from Mars (Bogard and Johnson 1983). Shergottite samples in particular are predominantly basaltic in composition (McSween 1985; Treiman 2003; Bridges and Warren 2006), and their petrological investigations allow for an estimation of the conditions in the magma source regions during melting, including the pressure, degree of partial melting, and water content (McSween et al. 2001). This information can then be tied to numerical models, which aim at describing the thermo-chemical evolution of the planet from a global perspective. One of the main inputs to these models is the bulk silicate composition with respect to heat producing elements, which have been constrained from SNC meteorites (Wänke and Dreibus 1994) and remote sensing data (Taylor et al. 2006).

This review attempts to provide an extensive summary of our current knowledge of volcanic processes on Mars, and we will begin with a description of the volcanic surface record observed in imaging data. We will then summarize the petrological data on martian igneous rocks, which has been gathered from orbit, in-situ, and from the SNC meteorites. Subsequent chapters focus on results from geophysical and geodynamical investigations, and we will conclude by outlining future lines of investigation, which could contribute to further our understanding of the igneous evolution of Mars.

2 History of Martian Volcanism

2.1 Morphological Characteristics of Volcanism over Time

Global mapping on the basis of morphological (Tanaka et al. 1992) and spectral data (e.g., Christensen et al. 2001; Bibring et al. 2005) reveals that large parts of the martian surface are covered by volcanic products. To first order, spectral signatures of basaltic materials and minerals such as pyroxene (e.g., Poulet et al. 2007) and plagioclase (e.g., Rogers and Christensen 2007) are detected wherever dust mantling is absent (Poulet et al. 2007), suggesting an overall basaltic composition. Andesitic compositions have been proposed for the northern lowlands (Bandfield et al. 2000), but may be alternatively interpreted as weathered basalts (Wyatt and McSween 2002). This does not imply, however, that most of the present surface materials of Mars are pristine solidified lava flows or pyroclastic deposits. From a morphological perspective, volcanic landforms are not uniformly distributed across the surface of Mars. Most of them are concentrated at a few large volcanic provinces that

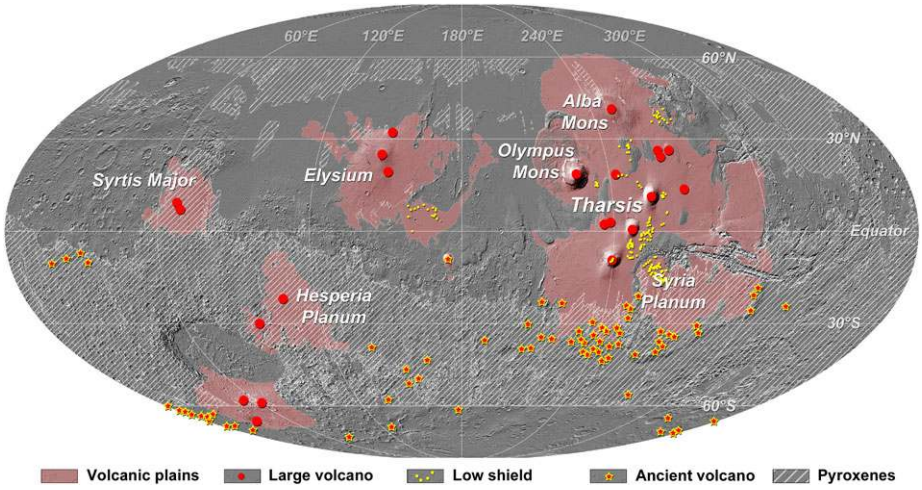

Fig. 1 Map of volcanic landforms on the basis of morphological observations. Background is a shaded digital elevation model derived from MOLA altimetry data in Mollweide projection. Low shields after Hauber et al. (2009), ancient volcanoes after Xiao et al. (2012), pyroxene-bearing surfaces after Ody et al. (2012)

are located at the Tharsis and Elysium rises (Hodges and Moore 1994), around the ancient Hellas impact basin (Williams et al. 2009), and at Syrtis Major (Fig. 1). By far the volumetrically largest of these provinces is the Tharsis bulge ($\sim 3 \times 10^8$ km^3; Phillips et al. 2001), a huge topographic rise centered near the equator which dominates almost the entire western hemisphere. Elysium is the second largest province, but its volume is much smaller than that of Tharsis ($\sim 3.5 \times 10^6$ km^3; Platz et al. 2010). Isolated volcanic edifices outside the large volcanic provinces are sparse and restricted to the cratered highlands (Xiao et al. 2012). The most prominent example is Apollinaris Mons, but there are a few dozen isolated highland massifs that are also interpreted to be of volcanic origin (Scott and Tanaka 1981). The spatial correlation between exposures of mafic minerals and morphological evidence of lava flows is not systematic, but does exist in the case of Syrtis Major and the circum-Hellas-Volcanic province (Fig. 1). However, the Elysium and Tharsis rises are covered by dust, generally precluding the detection of primary mineral phases other than those in the dust. Exposures of mafic materials also exist outside the major volcanic provinces (e.g., Valles Marineris, Noachian terranes). These mafic exposures may be associated with ancient magmatic systems whose surface expressions have been largely eroded, or they may also be attributed to reworked volcanic material that has preserved mafic signatures.

2.2 Styles of Volcanic Eruptions

Volcanic landforms can be subdivided into two broad categories: central volcanoes and volcanic plains. Central volcanoes on Mars have a size range covering at least two orders of magnitude. About 15 large shield volcanoes with diameters greater than 100 km are located in Tharsis and Elysium, the largest of which, Olympus Mons, has a basal diameter of $\sim$600 km and a height of $\sim$23 km. The morphometry of these large shields (Fig. 2(a)) is summarized by Plescia (2004). They share many morphological characteristics with large

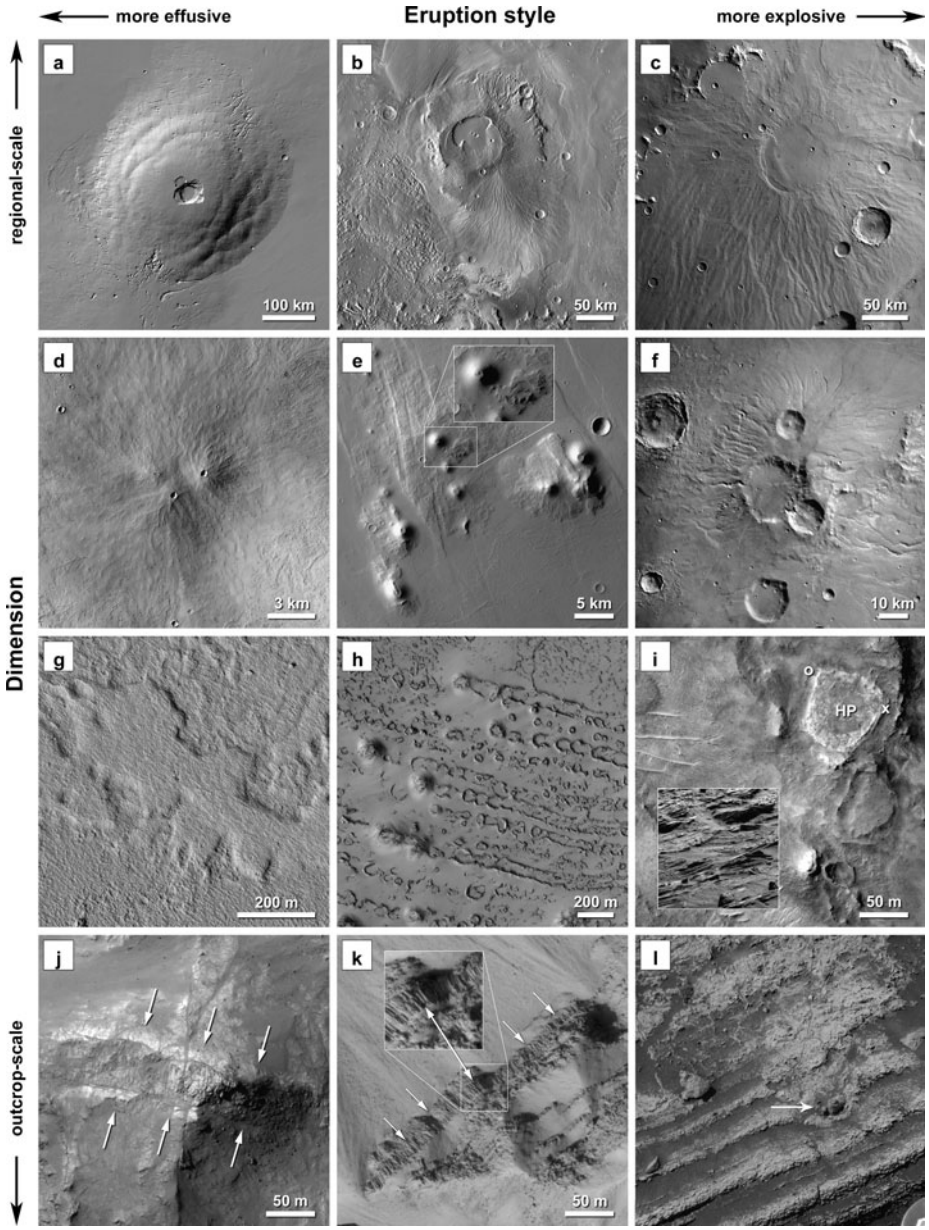
more effusive
Eruption style
more explosive
regional-scale
Dimension
outcrop-scale
a
b
c
d
e
f
g
h
i
j
k
l
100 km
50 km
50 km
3 km
5 km
10 km
200 m
200 m
50 m
HP
50 m
50 m

◀ **Fig. 2** Range of volcanic surface morphologies on Mars. The trends along the x- and y-axes represent inferred eruption style and scale of the volcanic landforms, respectively. (**a**) One of the large martian shield volcanoes, Ascraeus Mons, in the Tharsis volcanic province (center of caldera at ∼11.2°N/255.6°E). Image: Shaded version of gridded MOLA DEM. (**b**) Apollinaris Patera (8°S/174°E), a large volcano that might have produced effusive lava and pyroclastic material. Image: THEMIS-IR daylight mosaic. (**c**) Hadriaca Patera, a large shield with low relief northeast of the Hellas Basin (center of caldera at −30.18°S/92.8°E). The dissected flanks seem to be composed of easily erodible material, possibly indicating a significant contribution of pyroclastic material (e.g., volcanic ash; Williams et al. 2007). Image: HRSC mosaic of orbits h0528_0000 and h0550_0000. (**d**) Low shields with radial lava flows in Tharsis (2.4°S/252.05°E). Such edifices with very low relief (typically much less than a few hundred meters) and flank slopes $\ll 1°$ are thought to be built by lava flows with low viscosities (Hauber et al. 2009). Image: CTX P02_001906_1776. (**e**) Group of volcanic cones with associated lava flows (see *inset*) near the Ulysses Fossae, a set of extensional structures in Tharsis (center of image at 5.8°N/237.2°E). The morphology of this volcanic field is analogous to that of terrestrial fields of cinder cones (Brož and Hauber 2012). Image: HRSC h8396_0009. (**f**) Ancient, possibly volcanic construct in the plains of Thaumasia Planum (18.1°S/300.35°E). Although this and similar edifices elsewhere in the cratered highlands do not display primary volcanic features, their isolated high-standing topography, radial erosion patterns on the flanks, and some putative caldera structures suggest a volcanic origin. Image: HRSC h0449_0009. (**g**) Inflation features in lava flows in the Elysium volcanic province (7.741°N/164.410°E; illumination from the southwest, the feature in the image center has a positive topography). Such inflation features are well known on Earth and are typical for basaltic lava flows. They could be unambiguously identified on Mars in MOC and HiRISE images (Keszthelyi et al. 2008). Image: HiRISE PSP_003241_1880. (**h**) Alignment of rootless cones near southern Arcadia Planitia in the Tartarus Colles (26°N/173.7°E). Image: HiRISE PSP_006959_2060. The chain of cones is interpreted to be the result of successive steam explosions as solidified lava was moving over a fixed source of water (Keszthelyi et al. 2010). (**i**) Putative pyroclastic deposits of Home Plate (HP) in the Columbia Hills (Gusev Crater; center of Home Plate near 14.6°S/175.5°E). *Inset* shows cross-bedded layers (location marked by x in larger image), interpreted as pyroclastic deposits reworked by aeolian activity (Squyres et al. 2007). Image: HiRISE PSP_001513_1655, inset: MER Pancam 2P195076279). (**j**) Exposed dike (*arrows*) in the northern wall of Coprates Chasma (Valles Marineris, near 14.1°S/306.6°E). The dike displays the spectral characteristics of mafic material (Flahaut et al. 2011). Such dikes might have fed eruptions which constructed the km-thick accumulations of volcanic layers around the Valles Marineris region. (**k**) Columnar jointing (*arrows*) could be identified in a large, fresh, unnamed crater near Marte Vallis, centered at 21.52°N/184.35°E (Milazzo et al. 2009). The joints that separate the columns form as the lava contracts and fractures extend perpendicular to the cooling front (HiRISE image PSP_005917_2020). (**l**) Bomb sag-like structure (*arrow*, diameter ∼4 cm) in lower unit of Home Plate (location marked by o in panel (**i**)). The impact of the clast points to an explosive origin, either by volcanism or by an impact. Bomb sags are common in some terrestrial basaltic pyroclastic deposits (e.g., Walker and Croasdale 1971). Image: MER Pancam

terrestrial basaltic shields like those of Hawai'i and the Galapagos Islands, e.g., rift zones and nested caldera complexes (e.g., Crumpler et al. 1996; Mouginis-Mark et al. 2007; Carr and Greeley 1980), very low flank slopes (∼5°), and numerous large individual lava flows that can be channel-fed or tube-fed (Bleacher et al. 2007). Hundreds of much smaller low shield volcanoes, with diameters of a few km to tens of kilometers and heights of tens to hundreds of meters (Fig. 2(d)) are distributed across the wide plains between the large shields in Tharsis (Hauber et al. 2009). They share typical morphological characteristics with low basaltic shields on Earth, such as those in the Snake River Plain (Idaho, USA). To a lesser degree, some small shields are also observed in Elysium Planitiae (Vaucher et al. 2009) and on the Elysium bulge (Platz and Michael 2011). To our knowledge, no such low shields are found outside Tharsis and Elysium on Mars. Lava flows dominate both large and small shields, as well as the huge inter-shield plains in Tharsis and Elysium (Fig. 2(g)), indicating that at least the late stages of volcanism in these provinces were characterized by effusive eruptions.

Some large plains that are located peripherally to Tharsis do not display primary volcanic landforms such as lava flows, but are also thought to be emplaced by effusive volcanic eruptions, perhaps analogous to flood basalt eruptions on Earth. Examples of such

plains are Lunae Planum and other plains south of Valles Marineris or around Hellas (e.g., Hesperia Planum). They were typically deformed by contraction, as indicated by sets of wrinkle ridges. The interpretation as volcanic plains (Greeley and Spudis 1981; De Hon 1982) is based on their vicinity to volcanic centers such as Tharsis and by analogy with the basaltic plains of the lunar maria, which also exhibit wrinkle ridges that were formed due to compressional stresses during basin subsidence and cooling. Other evidence for a volcanic origin of these wrinkle-ridged plains comes from inspection of the walls of Valles Marineris, which provide a deep view into the upper crust. The wrinkle-ridged plains there seem to consist of at least 10 km-thick stacks of intact layers of competent material (McEwen et al. 1999). This observation is consistent with lava flows, while such voluminous sedimentary layers are not expected at this regionally high elevation without obvious sources for the sediment.

There may be many more unidentified volcanic plains on Mars. For example, the plains inside Gusev Crater were considered to be sedimentary before the arrival of the Mars Exploration Rover, Spirit, but were subsequently found to consist of low-viscosity basaltic lava flows (Greeley et al. 2005; McSween et al. 2006). Similarly, other smooth-appearing and level crater floors might consist of lava flows. Indirect evidence for igneous processes comes from sets of long and linear grabens radiating outward from Tharsis. One interpretation holds that they are the surface expression of dike swarms analogous to, for example, the Mackenzie dike swarm in the Canadian shield (Mège and Masson 1996; Wilson and Head 2002; Ernst et al. 2001). Further evidence for this idea is provided by direct observations of dikes in the walls of Valles Marineris (Flahaut et al. 2011, Fig. 2(j)).

The evidence for explosive eruptions on Mars is much less obvious than that for effusive eruptions. Several broad edifices with very gentle slopes ($<1°$) display flanks that are heavily eroded and seem to consist of friable material (Greeley and Crown 1990; Crown and Greeley 1993). Examples for such shields, e.g., Hadriaca Patera (Fig. 2(c)), are concentrated in the ancient southern highlands mainly around the Hellas impact basin (Fig. 1). They might consist of accumulations of pyroclastic material which were produced by large explosive eruptions, analogous to the Masaya Caldera Complex (Nicaragua) that produced large volumes of ash-fall deposits, ignimbrites, and surge deposits (Gregg and Williams 1996; Grott and Wieczorek 2012). Another area is the western flank of Hecates Tholus in Elysium, where pyroclastic deposits might have mantled the older substratum, creating a smooth-appearing surface (Mouginis-Mark et al. 1982; Hauber et al. 2005). Widespread layered deposits in equatorial regions, e.g., the Medusae Fossae Formation, may be the result of explosive eruptions (e.g., Hynek et al. 2003; Kerber et al. 2011), but this interpretation is controversial. The isolated volcanic highland massifs (Fig. 2(f)) might also be at least partly constructed from pyroclastic material.

Only a few smaller pyroclastic cones have been detected, and most of them are single and isolated features (e.g., Bleacher et al. 2007; Keszthelyi et al. 2008; Lanz et al. 2010). A notable exception is a field of relatively steep-sided cones with associated flows situated on an ancient, fractured window of older crust in Tharsis (Fig. 2(e)). This cone field is perhaps the morphologically closest analogue to terrestrial cinder cone fields (Brož and Hauber 2012). Evidence for explosive volcanic activity on Mars also comes from ground observations. In the Columbia Hills (Gusev Crater), a bright deposit with a roughly circular outline in plan view shows fine-scale layering and cross-bedding (Squyres et al. 2007) (Fig. 2(i)), similar to what is observed in terrestrial volcanic surge deposits formed by phreatomagmatic explosions. A feature resembling a bomb-sag (Fig. 2(l)) further contributes to the hypothesis that

this deposit, termed Home Plate, might have formed by explosive volcanism. Although the vent location could not be unambiguously identified, it seems likely that Home Plate formed by hydrovolcanic activity as a maar or tuff ring (Lewis et al. 2008) when the atmosphere was much denser than today (Manga et al. 2012).

Other volcanic surface features can also be explained by the interaction of magma with near-surface water or ice (Squyres et al. 1987; Smellie and Chapman 2002). A particularly convincing case is provided by pseudocraters or rootless cones that may have formed when lava flowed over a wet substrate, causing the water to vaporize and leading to steam explosions which disrupted the overlying lava blanket creating craters without magma conduits (Greeley and Fagents 2001; Lanagan et al. 2001; Fig. 2(h))

2.3 Environmental Effects on Eruption Style

It is well known that environmental conditions have a strong influence on the style of eruptions (Zimbelman and Gregg 2000), hence magma with a given composition and volatile content will erupt differently on Mars and Earth. Of the various factors controlling the behaviour of magma ascent and eruption (Whitford-Stark 1982), gravity and atmospheric pressure are the physical parameters that account for the most significant differences of volcanic processes on Mars and Earth. The lower surface gravity on Mars (only about 38 % that of the Earth) results in a smaller lithostatic pressure gradient and a lower lithostatic pressure at a given depth. This leads to differences in buoyancy-driven processes such as the ascent of magma diapirs. Since the density contrasts between magma and country rock are considered to be similar on Mars and Earth, magma bodies should rise more slowly on Mars. To avoid cooling and solidification, therefore, magma diapirs are required to be larger than on Earth to reach shallow crustal levels (Wilson and Head 1994). Gravity also influences the depth of neutral buoyancy levels, the vertical extent of magma chambers, the width of dikes and thus effusion rates, and the thickness of lava flows (Table 1). The lower lithostatic pressure leads to volatile oversaturation of magma and the nucleation of bubbles at greater depth (Wilson and Head 1994).

The atmosphere of Mars is currently about two orders of magnitude less dense (∼6–10 mbar) than that of the Earth. This difference has consequences on volcanic eruption styles. The pressure decrease during magma ascent leads to the exsolution of volatiles, which form gas bubbles that nucleate at depth (see above) and grow and coalesce as the magma rises, until the magma will be fragmented and disrupted into a mixture of pyroclasts and gas. The lower atmospheric pressure on Mars implies that after fragmentation the gas expansion is accelerated and the ejection velocities of magma clots and gas will be larger on Mars. Since gravitational acceleration is lower and drag forces on the ejected particles are smaller in the thinner atmosphere, ballistic trajectories will be longer and particles will be dispersed more widely around explosive eruption sites. Cinder cones and hydrovolcanic constructs such as maars should therefore be lower and wider, which would make their identification harder (Wilson and Head 1994). Basaltic plinian eruptions should also be quite common on Mars, and thick and widespread deposits of ash and accretionary lapilli could have formed (Wilson and Head 2007). Extensive blankets of (layered) mantling material (e.g., Mouginis-Mark et al. 1982; Grant and Schultz 1990; Hynek et al. 2003) might represent such products of plinian eruptions. It has to be noted, however, that these theoretical predictions on different environmental effects on eruption styles on Mars and Earth are only valid for a given volatile content. It is unknown if the volatile content of Martian magmas is high enough to favour explosive eruptions. Recent

Table 1 Environmental effects on selected volcanic processes on Mars as compared to Earth (after Wilson and Head 1994; Greeley et al. 2000; Parfitt and Wilson 2008)

Parameter	Physical effect	Result
Magma ascent		
Gravity	Smaller buoyancy forces lead to smaller ascent velocities	Rising magma bodies must be larger on Mars (to avoid cooling and solidification)
	Fluid convective motions, crystal settling, and diapiric ascent rates are slower	Larger diapirs can ascend to shallower depths
	Neutral buoyancy zones and magma reservoirs are deeper	Wider dikes and larger driving pressures are needed $\longrightarrow$ greater eruption rates and individual eruption volumes
	Lower stresses in magma reservoir of given vertical extent	Greater vertical extents of magma chambers before wall rock strength is exceeded
Role of volatiles		
Gravity	Lower lithostatic pressure at given depth (and lower lithostatic pressure gradient)	Volatile exsolution, bubble nucleation and magma disruption occur at greater depths
Atmospheric pressure	Larger gas expansion and more efficient energy release (see above)	Greater eruption velocities, more thorough magma fragmentation and smaller particle sizes: basaltic Plinian eruptions should be common on Mars
	Reduced aerodynamic drag forces	Long trajectories of pyroclasts, efficient cooling
		Wide dispersion of poorly consolidated fine-grained deposits
		Broader edifices with smaller heights, smaller ratios of height to basal diameter of pyroclastic edifices
		Larger ratio of crater diameter to basal diameter of pyroclastic edifices
Effusive eruptions		
Gravity	Reduced shear stress	Thicker lava flows with greater lengths (with sufficient volume)
	For a given volcanic load, the reduced gravitational acceleration causes less flexure of a lithosphere with given strength and thickness	Higher volcanic edifices possible
	Increase in dike widths by factor of two (see above)	Higher effusion rates by factor of five
Atmospheric pressure	Lower heat loss by natural and forced convection	Tendency towards longer (cooling-limited) flows

results from SNC studies indicate that their water content might be low (e.g., Filiberto and Treiman 2009; see also Sect. 3.3.5). In this respect, we note that unambiguous morphological evidence for explosive volcanism on Mars is sparse (e.g., Brož and Hauber 2012).

2.4 Chronology

Early chronological classifications of martian volcanic surfaces were provided on the basis of low-resolution images (e.g., Neukum and Hiller 1981). More recently, more standardized crater counts using images of higher spatial resolution together with improvements in cratering models (Hartman and Neukum 2001) have led to new compilations of volcanic ages (Fig. 3) (e.g., Werner 2009; Williams et al. 2009; Robbins et al. 2011; Hauber et al. 2011; Platz and Michael 2011; Vaucher et al. 2009).

In general, it appears that the oldest volcanic surfaces are roughly 4 to 3.7 Ga old. They are mainly present on the highland shields such as Hadriaca and Tyrrhena Montes, and on the heavily eroded volcanic highland massifs. Tharsis and Elysium show ancient surfaces too, but to a lesser degree. The volcanism in the highlands seems to have stopped at $\sim$1 Ga at the latest (Williams et al. 2009). More recent volcanism has been limited to Tharsis and to Elysium. The uppermost surfaces in Elysium have a very wide range of ages, spanning more than 3 billion years (Platz and Michael 2011). This diversity implies that the bulk of the Elysium bulge is very old and that the mean eruption rates in Elysium over time were low, because otherwise no old volcanic units should have survived at the surface without being buried by younger units. The youngest lavas in the Elysium province were emplaced in the Cerberus plains as recently as a few million years ago (Vaucher et al. 2009). The bulk of the Tharsis bulge is thought to be $>$3.8 Ga old, as indicated by uplifted old surfaces, the age of tectonic structures, and by ancient valley networks that seem to post-date the formation of the main topographic expression of Tharsis (Phillips et al. 2001). The voluminous volcanic material of the ridged plains is old too, with the latest (i.e. uppermost) units emplaced in the Early Hesperian. This apparent early Hesperian age of the ridged plains has been taken as evidence for a peak of volcanic activity in the late Noachian and early Hesperian, but since the bulk of the ridged plains, which can be $>$10 km thick (McEwen et al. 1999), is buried and only partly usable for age dating (Platz et al. 2010), the true age of ridged plains may be much older. On the other hand, however, the caldera floors and thus the last major phases of activity of the huge Tharsis shields are only a few hundred million years old (Neukum et al. 2004; Robbins et al. 2011). Even younger ages were measured for some lava flows on the large shields (Hartmann et al. 1999) and for many low shields in Tharsis (Hauber et al. 2011). It appears possible, therefore, that a certain level of volcanic activity persisted in Tharsis throughout most of Mars' history, perhaps up to the present day.

Overall, it appears that volcanism was intense in the early history of Mars at least during the late Noachian but that this activity gradually declined over time. This overall decline might have been punctuated by episodic periods of higher intensity (e.g., Wilson 2001; Neukum et al. 2004), as also discussed by Head et al. (2001).

2.5 Eruption Rates

The erupted volumes of volcanic materials are difficult to determine. Unless the subsurface can be accessed, for example by radar measurements, only the surface can be directly observed. In theory, radar sounding instruments can detect interfaces at depth, which might correspond to the basal surface of lava flows. For example, the Shallow Radar (SHARAD) on board the Mars Reconnaissance Orbiter mission is capable of detecting interfaces down to a depth of up to $\sim$1000 m, if there is a sufficient contrast in the dielectric constant of the adjacent layers. In reality, however, the detectability of subsurface echoes in non-icy environments is limited by several factors related to surface roughness and dielectric properties. Where lava flows are stacked without displaying a density contrast (a likely situation

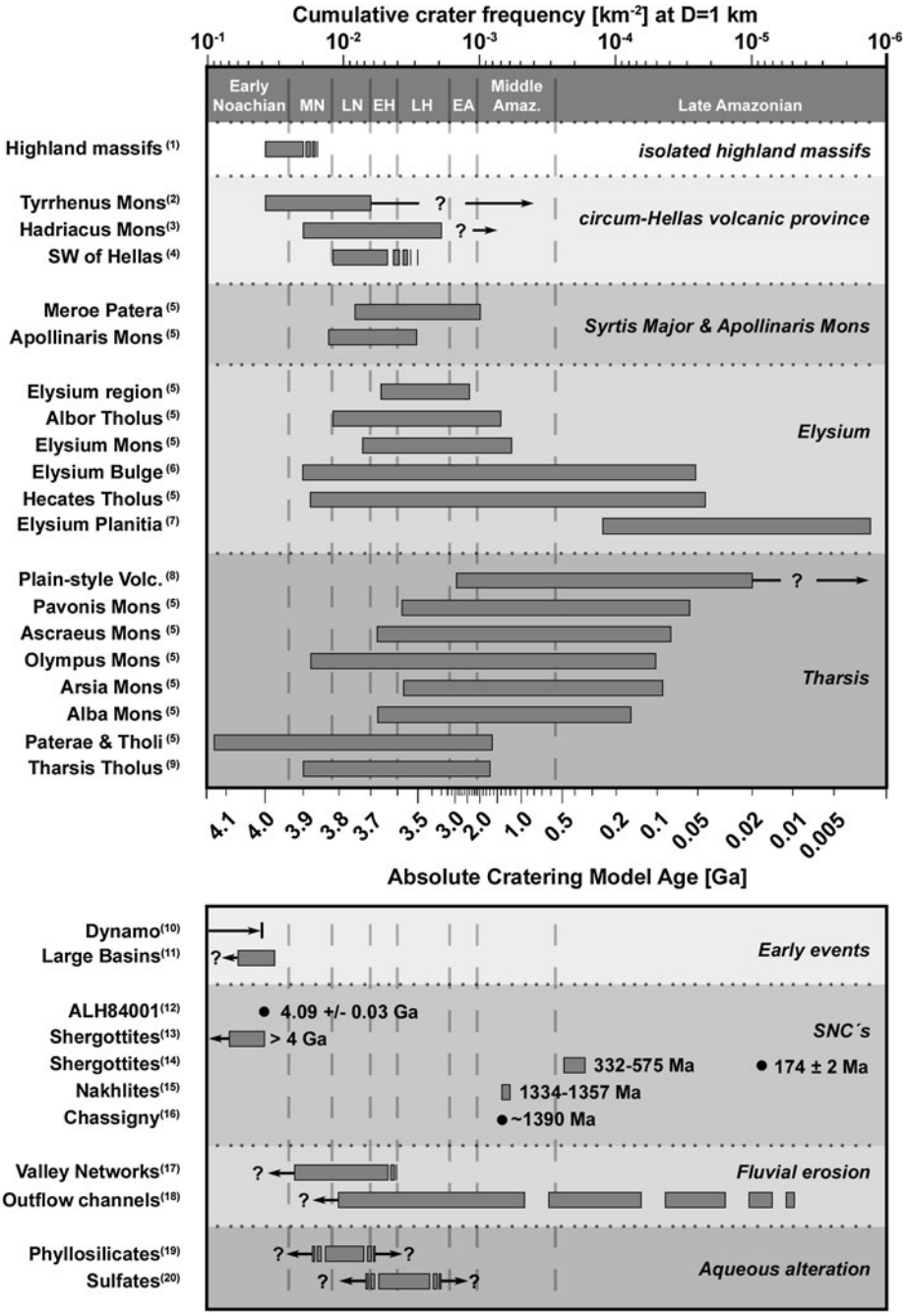
Cumulative crater frequency [km-2] at D=1 km
10-1
10-2
10-3
10-4
10-5
10-6
Early Noachian
MN
LN
EH
LH
EA
Middle Amaz.
Late Amazonian
Highland massifs (1)
isolated highland massifs
Tyrrhenus Mons (2)
Hadriacus Mons (3)
SW of Hellas (4)
circum-Hellas volcanic province
Meroe Patera (5)
Apollinaris Mons (5)
Syrtis Major & Apollinaris Mons
Elysium region (5)
Albor Tholus (5)
Elysium Mons (5)
Elysium Bulge (6)
Hecates Tholus (5)
Elysium Planitia (7)
Elysium
Plain-style Volc. (8)
Pavonis Mons (5)
Ascraeus Mons (5)
Olympus Mons (5)
Arsia Mons (5)
Alba Mons (5)
Paterae & Tholi (5)
Tharsis Tholus (9)
Tharsis
4.1
4.0
3.9
3.8
3.7
3.5
3.0
2.0
1.0
0.5
0.2
0.1
0.05
0.02
0.01
0.005
Absolute Cratering Model Age [Ga]
Dynamo (10)
Large Basins (11)
Early events
ALH84001 (12)
4.09 +/- 0.03 Ga
Shergottites (13)
> 4 Ga
Shergottites (14)
332-575 Ma
174 ± 2 Ma
Nakhlites (15)
1334-1357 Ma
Chassigny (16)
~1390 Ma
SNC´s
Valley Networks (17)
Outflow channels (18)
Fluvial erosion
Phyllosilicates (19)
Sulfates (20)
Aqueous alteration

◀ **Fig. 3** Schematic timeline of Martian volcanism as derived from crater statistics. It is not possible to determine the onset of volcanism for a particular area (i.e. the age of completely buried surfaces), so the start of volcanic activity is uncertain for all regions. Volcanism first ended in the southern highlands (isolated massifs, circum-Hellas province), and focused afterwards at Tharsis and Elysium, where it continued almost until present. The lengths of bars in the upper panel represent diverse ages in the respective volcanic provinces, i.e. they do not represent error bars. *The lower panel* shows the dated ages of Martian meteorites and some key events in Martian history that might have been related to volcanism. The lengths of bars of SNC meteorites represent error bars, since a given meteorite has, theoretically, a unique age. References: (1) (Xiao et al. 2012); (2) (Williams et al. 2008); (3) (Williams et al. 2007); (4) (Williams et al. 2010); (5) (Werner 2009); (6) (Platz and Michael 2011); (7) (Vaucher et al. 2009); (8) (Hauber et al. 2011); (9) (Platz et al. 2011); (10) (Lillis et al. 2008); (11) (Werner 2008); (12) (Lapen et al. 2010); (13) (Bouvier et al. 2008); (14) (Borg et al. 2005); (15) (Misawa et al. 2006); (16) (Park et al. 2009); (17) (Fassett and Head 2008); (18) (Neukum et al. 2010); (19) (Loizeau et al. 2010); (20) (Wray et al. 2009)

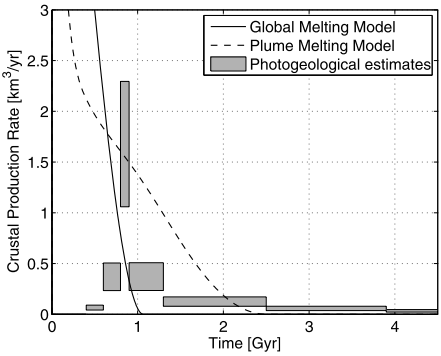

Fig. 4 Crustal production rate as a function of time as obtained from photogeological estimates based on Viking data (Greeley and Schneid 1991). The total amount of produced crust has been calculated using terrestrial ratios of extrusive to intrusive volcanism between 1:5 and 1:12 (White et al. 2006). For comparison, crustal production rates for two numerical models assuming melt generation in a global melt layer (*solid line*) and melt generation in localized plumes (*dashed line*) are also shown (Grott et al. 2011; Morschhauser et al. 2011). Total average thickness of produced crust in these models is ∼50 km

in the Tharsis region), radar instruments will not be able to detect any interface, and to date SHARAD has identified only a few subsurface interfaces in volcanic settings (Simon et al. 2012). The Mars Advanced Radar for Subsurface and Ionosphere Sounding (MARSIS) on board Mars Express has a longer wavelength than SHARAD and can probe the subsurface to greater depths, but the strong attenuation of radar signals in basalt prevents the large penetration depths required to see the base of km-thick lava sequences. For large-scale analyses it is therefore necessary to infer the thicknesses and volumes of geologic units from circumstantial evidence, such as the record of ancient crater populations not fully buried by more recent deposits (De Hon 1974). Another difficulty concerns the distinction between intrusive and extrusive materials. In the absence of subsurface knowledge, their volumetric ratio cannot be determined. Geophysical methods such as the analysis of the topography and gravity fields can help to assess magmatic volumes at very large scales (e.g., Phillips et al. 2001; Grott and Wieczorek 2012), but the limited spatial resolution of geophysical data sets prevents their application on more local scales.

The most comprehensive analysis of erupted volumes to date was performed using Viking data, i.e. prior to the detailed global topographic information from MOLA. According to this study (Greeley and Schneid 1991), the total volume of extrusive and intrusive magma generated over the last ∼3.8 Ga is about 654×10^6 km^3, or 0.17 km^3 per year (see Table 2 for

Table 2 Martian magma volumes (from Greeley and Schneid 1991; Exp.: Exposed; Extr.: Extruded; Thickn.: Thickness; Topogr.: Topography; LA: Late Amazonian; MA: Middle Amazonian; EA: Early Amazonian; LH:Late Hesperian; EH: Early Hesperian; LN: Late Noachian; MN: Middle Noachian; EN: Early Noachian). The magma volume extruded on plains was determined assuming that some portion of volcanic plains are covered by non-volcanic units, so the total area of volcanic plains is larger than the exposed area of volcanic plains. The total magma volume assumes a ratio of intrusive to extrusive magma of 8.5:1 (which is an average ratio for Earth, Crisp 1984)

Epoch	Area of plains [10^6 km^2]	Exp. plains volume [10^6 km^3]	Thick. of plains [km]	Extr. plains volume [10^6 km^3]	Volume from topogr. [10^6 km^3]	Total extr. volume [10^6 km^3]	Total magma volume [10^6 km^3]
LA	1.06	0.29	0.27	0.33	1.78	2.11	20
MA	3.28	1.04	0.32	1.42	7.07	8.49	81
EA	7.93	2.22	0.28	3.61	12.1	15.76	150
LH	7.63	1.87	0.24	4.54	11.0	15.63	148
EH	22.52	3.95	0.18	10.8	6.82	17.65	168
LN	9.31	1.28	0.14	4.31	3.46	7.77	74
MN	2.85	0.47	0.17	1.39	0.00	1.39	13
EN	?	?	?	?	?	?	?
Total	54.57	11.12	0.20	26.43	42.37	68.80	654

a summary). It has to be noted that the amount of intrusive igneous material was estimated in the study of Greeley and Schneid (1991) on the basis of terrestrial ratios of intrusive to extrusive volumes. Because erosion rates are low on Mars and large-scale exhumation by tectonic events is limited, however, direct observations of intrusive magmatic bodies are rare (Flahaut et al. 2011). Nevertheless, intrusives are expected to be common, since the lower buoyancy forces and the deeper levels of neutral buoyancy would seem to favor stalling of magma diapirs and dikes at depth. Recent analysis of magnetic and spectral data seem to indirectly confirm their existence (Lillis et al. 2009; Farrand et al. 2011). The rate of magma production reported by Greeley and Schneid (1991) is substantially lower than rates for the Earth (26 to 34 km^3 yr^1) or Venus (<20 km^3 yr^{-1}), but much higher than for the Moon (0.025 km^3 yr^{-1}), in qualitative agreement with what would be expected from a planet with intermediate mass. Importantly, this is an average rate over the entire history of Mars. The determination of eruption rates at specific times is complicated by the fact that the lowermost stratigraphic units of large volcanic edifices and provinces are not accessible for age determination. The relatively minor volumes of extruded material in the Noachian (Fig. 4) (Greeley and Schneid 1991) is likely an observational bias, since it is expected from thermal models that the Noachian was a period of intense magmatism (e.g., Morschhauser et al. 2011). Note, however, that it has also been suggested that there might have been a peak in magmatic activity during the Hesperian period (Bibring et al. 2006), which could have been caused by mantle heating following a relatively cold initial state after core formation. Improved methods to determine the volumes of volcanic provinces on the basis of accurate topographic data and crater populations (Vaucher et al. 2009; Platz et al. 2010) together with detailed chronologies (Platz and Michael 2011) will help to refine the rates of magmatism over time.

3 Martian Igneous Petrology

3.1 Chemistry and Mineralogy of Igneous Rocks from Orbit

3.1.1 Methods and Limitations

Several remote sensing methods are now available for characterizing the chemistry and mineralogy of igneous materials at the surface of solid planets. Here we include image-based morphometric analyses of lava flows, which provide clues to composition. Mineralogical information is generally obtained using the visible and infrared range of the electromagnetic spectrum (Bandfield et al. 2000; Poulet et al. 2009a), whereas abundances of chemical elements are principally derived from gamma-rays (Boynton et al. 2007) and neutron spectroscopy (Feldman et al. 2011). These methods offer advantages and disadvantages in terms of spatial resolution, depth of penetration, and sensitivity to the chemical and mineralogical parameters that are important for understanding magmatic processes. Deriving the chemical or mineralogical composition generally involves deconvolution algorithms to separate individual components, and some of these procedures are at different degrees of development. As a consequence, the degree of uncertainty varies between one method and another and is discussed below.

Chemistry from Nuclear Spectroscopy Elements that are both detectable and are major constituents of igneous rocks are Fe, Si, and Ca (Boynton et al. 2007; Boynton et al. 2008); also relevant are the incompatible elements K and Th (Taylor et al. 2006), and mobile elements such as Cl (Keller et al. 2006a). Three other interesting elements are detected, but their derived abundances are still preliminary: Al, S, and U (Evans et al. 2008). The specific case of hydrogen detection is discussed in the chapter by Lasue (2012, this issue). The Gamma Subsystem (GS), onboard the Mars Odyssey orbiter, measured the flux of gamma photons emitted by atomic nuclei with distinguishing energies (Evans et al. 2006). The analysis of these data provided elemental abundances (mass fractions) in the subsurface to decimeter depths (Boynton et al. 2007; Karunatillake et al. 2007). The surface is assumed to have a uniform composition over the sampling depth (several tens of centimeters). Attempts to detect layering signatures, by monitoring gamma-ray lines from a given element at different energies, did not reveal any obvious effect (Keller et al. 2006b), except for hydrogen (Maurice et al. 2011; Feldman et al. 2011) and chlorine (Diez et al. 2009). Because these observations were conducted from orbit and at high-energy (above 100 keV), the signal was not collimated and the spatial resolution is limited to about 500 km (corresponding to 50 % of the photon flux received from the surface). The data are usually reported on a cylindrical grid made of 5-deg. bins, based on cumulative spectra processed with a mean filter (Karunatillake et al. 2011). At these scales, the surface of Mars is seen as a mixture of materials of regional origin with variable amounts of the local bedrock, including mantling materials (fragments of rocks, sediments, and dust) (Newsom et al. 2007).

The intrinsic properties of the GS detection are appropriate to study the weakly altered basaltic materials that make up most of the surface of Mars. Five to eight broad homogeneous provinces can be defined, primarily driven by their chlorine and hydrogen contents, although some diversity is found in both mantled and less-mantled provinces (Gasnault et al. 2010; Taylor et al. 2010). In particular, the GS data reveal some variability in the spectrally uniform high-albedo areas (Newsom et al. 2007). The compositions detected in the volcanic regions are compatible with primary melts of the martian mantle and may be used to infer

the conditions of partial melting (El Maarry et al. 2009). However, secondary surficial processes must be invoked to explain the elemental composition in other areas (Karunatillake et al. 2009), which is consistent with the extensive alteration and sedimentary processes and the associated mineralogical diversity revealed by other instruments (Grotzinger and Milliken 2011).

Visible and Near-Infrared Spectroscopy Visible and Near-Infrared (VNIR) spectroscopy takes advantage of electromagnetic radiation in the wavelength region from 0.35 to 5.0 μm. The precise wavelength where VNIR ends and the thermal IR begins depends to some extent on the temperature of the surface, but the transition occurs where the fundamental electromagnetic radiance becomes dominated by reflected radiation from the sun versus the radiance emitted from a heated surface. For cold surfaces the transition is at longer wavelengths and for warmer surfaces it is at shorter wavelengths. Processes that lead to absorptions in the VNIR range are dominated by two categories: electronic absorptions and molecular vibrations (e.g., Clark 1999).

Electronic absorptions are first and foremost dominated by crystal field absorptions in iron-bearing mafic minerals. Electronic transitions between energy levels in the d-orbitals of iron in distorted octahedral sites in minerals such as olivine and pyroxene (Burns 1993a) lead to broad and diagnostic absorptions. For example, pyroxene shows two electronic transition absorptions near 1 and 2 μm, the exact wavelengths of which vary with Fe, Mg, and Ca cation concentration (Adams 1974; Cloutis et al. 1986). The systematics of how these absorptions vary with composition have been characterized empirically, allowing discrimination of low calcium pyroxene from high calcium pyroxene, their broad iron contents, and the iron content of olivine (e.g., Sunshine et al. 1990; Sunshine and Pieters 1993; Kanner and Mustard 2007; Isaacson and Pieters 2009). Charge transfer, where electrons transition between anions and cations or oxidation states (e.g., between Fe^{2+}–O^{2-} or Fe^{2+}–Fe^{3+}) have diagnostic absorptions in the 0.2–1.1 μm region, and are particularly useful for recognizing ferric oxides (Burns 1993b; Morris et al. 1985; Bell et al. 1990).

VNIR data contain a host of narrow, diagnostic absorptions due to overtones and combination tones of fundamental molecular absorptions. The most common of these are due to water and hydroxyl in crystal structures. For example, smectite clays show a diagnostic absorption near 1.9 μm due to the combination of the fundamental OH stretch and H-O-H bend in water. The position, shape and character of this absorption depends on water abundance and the particular mineral site it is held in. In the 2.0–2.5 μm region are numerous narrow absorptions due to the combination tones of hydroxyl band modes. The molecular absorptions are diagnostic of the common clays, phyllosilicates, carbonates, and sulfates.

VNIR absorption features are maximized when the particle size of the material being measured is in the size range of 45–125 μm. With larger particles there is less penetration of light into the material and thus the path length of photons is reduced leading to weaker absorptions. Conversely, with smaller particles there is more scattering of light because of increased first-surface Fresnel reflection leading to, again, less penetration of photons into the material and weaker absorptions. In general the penetration depth of photons is several hundred microns so the detection of minerals with VNIR is very much a surface measurement.

The majority of the analyses with VNIR data have been directed to the detection of mineral phases based on the molecular vibration bands and their characteristics and this has been very successful (e.g., Poulet et al. 2005; Bibring et al. 2005; Mustard et al. 2008). There has recently been an effort to calculate the phase assemblages from VNIR data (e.g., Poulet

et al. 2009a, 2009b) which has the potential of modeling mineral abundances to ±10 % with optical constants appropriate to the phases modeled. In addition, several studies have used the Modified Gaussian Model (MGM, Sunshine and Pieters 1993) to characterize the mafic mineral phases in martian VNIR data (Mustard et al. 1997; Baratoux et al. 2007; Skok et al. 2010).

There have been three VNIR imaging spectrometers on orbital platforms that have acquired data at Mars: (1) Imaging Spectrometer for Mars (ISM, Bibring et al. 1989), (2) Observatoire pour la Minéralogie, l'Eau, les Glaces, et l'Activité (OMEGA, Bibring et al. 2004) on the Mars Express spacecraft and (3) the Compact Reconnaissance Imaging Spectrometer for Mars (CRISM, Murchie et al. 2007) on the Mars Reconnaissance Orbiter. ISM was on the Phobos-II spacecraft and this instrument acquired a number of pioneering data sets for the martian surface at 22 km spatial resolution in the wavelength range 0.76–3.16 μm. OMEGA acquired data across three detectors from 352 contiguous channels covering 0.35 to 5.1 μm and the spectral sampling varied from 7 nm in the visible to 20 nm at 2.5 to 5.1 μm. Because Mars Express was in an elliptical orbit, the spatial resolution for OMEGA varied from 300 m to 4.8 km and it has acquired near global coverage at the lower resolution. CRISM's data covers the spectral range 0.36 to 3.92 μm in 522 channels. The spatial resolution varies from 16 m at the highest resolution, targeted mode, to 200 m in the multispectral survey mode.

Thermal Infrared Spectroscopy Spanning the wavelength range of ∼5 to 50 μm (2000 to 200 cm^{-1}), thermal infrared (TIR) spectroscopy offers the capability to identify and quantify the abundance of all primary igneous phases, including glasses. The technique is sensitive to the fundamental vibrational modes of molecules bound in crystal lattices; in short-range ordered molecules in amorphous phases; and unbound molecules in gases and liquids. Orbital measurements rely on the passive emission of TIR radiance produced by solar insolation. Radiance spectra are converted to temperature-independent emissivity spectra that typically display a range of broad overlapping bands and narrow discrete bands that are diagnostic of composition.

Because the vibrational frequencies of molecules are a function of both the anion and cation components and their relationship to adjacent molecules in a crystal lattice, TIR spectra are very sensitive to variations in composition and crystal structure. This leads to the ability to distinguish among different varieties of major rock-forming minerals like pyroxenes, olivines, and feldspars. Members of solid-solution series can be distinguished from endmember compositions in all cases. For example, members of the olivine series can be identified with a precision of Fo ±10 (e.g., Koeppen and Hamilton 2008).

In addition to compositional information, TIR spectra present features that are a function of particle size. As the size of unbound particles (e.g., regolith) approaches TIR wavelengths (<100 μm), the effect of multiple scattering is manifested in the spectra as a loss of contrast of the primary bands known as reststrahlen features and the introduction of secondary bands known as transparency features (e.g., Salisbury and Eastes 2008). On Mars, the relatively high albedo reddish dust is an example of fine particulate material that displays particle size effects in its TIR spectrum. This dust also obscures the underlying substrate as its thickness approaches TIR wavelength, such that as little as 100 μm precludes characterization of a dust-coated surface (e.g., Johnson et al. 2002).

The abundance of component phases present in mixtures can be determined from deconvolution (unmixing) of TIR spectra. Unlike at VNIR wavelengths, TIR spectra of intimate mixtures of mineral grains in a rock or coarse particles (>100 μm) in regolith have been shown to represent a linear combination of the individual components. A linear least squares

algorithm and a library of spectral endmembers can be applied to mixed spectra in order to identify components and their abundance (Ramsey and Christensen 1998). Non-linear effects arise from intimate mixtures of fine ($\ll$100 μm) and coarse particles in the field of view, which confounds deconvolution. Detection limits for component phases are variable because of the varying spectral contrast of different minerals, but are in the range of ∼5 to 15 % by area fraction (e.g., Christensen et al. 2001).

Two orbital TIR instruments have been sent to Mars to investigate surface mineralogy. The Thermal Emission Spectrometer (TES) on the Mars Global Surveyor spacecraft was a hyperspectral instrument (∼6–50 μm; 1670–200 cm^{-1}; ∼10 cm^{-1} sampling) with a 3 × 2 array detector with a spatial resolution of ∼3 × 6 km that operated from 1996 to 2006 Christensen et al. 2001). The Thermal Emission Imaging System (THEMIS) on the Mars Odyssey spacecraft is a multispectral (9 unique bands from ∼7 to 15 μm) imager capable of 100 m spatial resolution (Christensen et al. 2003). THEMIS spectral data typically are used in a complementary fashion with TES spectra (e.g., Christensen et al. 2005; Michalski and Fergason 2009).

3.1.2 Morphometric Analysis of Lava Flows

The morphology of lava flows can provide clues to their rheology, which in turn provides information on lava composition and eruption conditions. Temperature, effusion rate, magma composition and volatile content together with external parameters such as the surface atmospheric conditions and the slope of the underlying terrain all combine to give a lava flow a final morphological shape. The study of this shape and of the inferred rheological properties of a lava flow provides insights into these parameters. Even for terrestrial lava flows, however, it is far from straightforward to determine their rheological properties. On Mars it is more difficult yet, since there are no observations of active lava flows, no samples of known source regions, and, due to the ubiquitous dust cover, very little compositional information of the well-preserved lava flows of Tharsis and Elysium. Therefore, the only way to assess the rheology and nature of martian lava flows is the study of their morphometry. The foundations of these techniques were laid by Jefffreys (1925), who studied the purely viscous behaviour of water flowing on an inclined surface, and Hulme (1974), who described a method to determine the yield strength of a Bingham fluid, recognizing that lava typically displays a non-Newtonian behavior. A compilation of rheological interpretations of morphometric measurements in lava flows is given in Table 3. As pristine morphologies are required to apply the above methods, results are mostly confined to the Amazonian period.

It needs to be emphasized, however, that there are many caveats associated with studies of martian lava flow rheology from morphometry. An example is the process by which a lava flow is delivered to the surface. It can be fed directly from a vent that is linked to a magma chamber, but it can also be fed by a lava lake that originates from accumulation during a Hawaiian-style eruption of magma clots ejected in a fire fountain that are still sufficiently hot (i.e. molten) upon landing. In the latter case, the initial temperature of a lava flow will be lower. Rheology depends on temperature, and care must be taken to avoid misinterpretations of such temperature differences as compositional differences (Wilson and Head 1994). Moreover, most empirical models that link morphology to rheology are based on laboratory results, not on field studies, and they apply to terrestrial lava compositions, not to the Fe-rich compositions that are found at the surface of Mars.

3.1.3 Young Volcanism

Evidence for recent volcanism (see Sect. 2.4) is now well accepted and activity is concentrated in the Tharsis and Elysium provinces (Neukum et al. 2004; Jaeger et al. 2007;

Table 3 Viscosity η and yield strength τ for lava flows in different regions on Mars. Methods: a: The effusion rate is determined from Graetz and Jeffrey equations modified by Sakimoto et al. (1997) for a rectangular flow. b: Yield strengths determined from bingham flow equations (Hulme 1974), c: Effusion rate from the Graetz equation and viscosity from Wilson and Head (1983), d: Effusion rate from the Graetz equation and viscosity from Fink, Griffiths and Fink (1978, 1992). References: [1]Baptista et al. (2008), [2]Basilevskaya and Neukum (2006), [3]Hiesinger et al. (2007), [4]Vaucher et al. (2009), [5]Warner and Gregg (2003), Sakimoto et al. (1997), [6]Sakimoto et al. (1997), [7]Zimbelman (1985)

Region	Age	Methods	Results
Syria Planum[1]	Hesperian	a	$\eta = 6.7 \times 10^5$–4.2×10^6 Pa s
		b	$\tau = 7.9 \times 10^2$–1.7×10^3 Pa
Olympus Mons[2]	Amazonian	c	$\eta = 1.4 \times 10^3$–2.8×10^7 Pa s
		b	$\tau = 0.9 \times 10^3$–3.6×10^4 Pa
Ascraeus Mons[3]	Amazonian	c	$\eta = 1.8 \times 10^4$–4.2×10^7 Pa s
		d	$\tau = 2.0 \times 10^4$–4.2×10^7 Pa
Central Elysium Planitia[4]	Amazonian	a	$\eta = 1.0$–2.5×10^5Pa s
		b	$\tau = 100$–500 Pa
Arsia Mons[5]	Amazonian	a	$\eta = 10^4$–10^6 Pa s
		b	$\tau = 10^3$ Pa
Alba Patera[6]	Amazonian	a	$\eta = 10^2$–10^5 Pa s
Ascraeus Mons[7]	Amazonian	a	$\eta = 6.4 \times 10^5$–2.1×10^8 Pa s
		b	$\tau = 3.3 \times 10^3$–8.4×10^4 Pa

Vaucher et al. 2009; Hauber et al. 2011). Unfortunately, volcanic regions that were active during the Amazonian are often covered by dust, affecting the remote sensing analysis of the composition of the underlying igneous rocks. Morphologic studies of Martian lava flows in such regions indicate that they are characterized by low viscosities (Table 3) with rheologic properties that are most often similar to terrestrial basaltic flows, whereas exceptionally fluid flows, compatible with ultramafic compositions, have been also reported. GRS data have revealed substantial chemical differences between terrains mantled by dust, which suggests that superficial material has a local origin, rather than being homogenized at the global scale (Newsom et al. 2007). In this case, recent volcanic regions may have a chemical signature consistent with the partial melting of the mantle. This hypothesis has been tested for the case of the Tharsis region and the mantle composition proposed by Dreibus and Wänke (1985), leading to the conclusion that magma was likely produced from 3–10 % of partial melt at pressures of 1.5–2 GPa (corresponding to a depth of 125–170 km) (El Maarry et al. 2009). Based on GRS data, the chemistry of young volcanic regions is characterized by a Si-poor (42–45 wt%) composition, iron oxide being relatively variable (16–22 wt%) (Baratoux et al. 2011a).

At the resolution of CRISM and THEMIS, a few young and dust-free exposures of volcanic materials exist, such as Amazonis Planitia (Stockstill-Cahill et al. 2008), Noctis Labyrinthus, and Echus Chasma (Mangold et al. 2010). In addition, several dozens of domes in Acidalia Planitia have been interpreted as recent volcanic features or cryptodomes associated with volcanic intrusions (Farrand et al. 2005). This hypothesis is now supported by their association with mafic signatures in visible and near-infrared spectroscopy (Farrand et al. 2011). In general, the mineralogy associated with young volcanic material is dominated by a high-calcium pyroxene and plagioclase. Olivine has been detected as the dominant phase in low-albedo deposits at Amazonis Planitia, implying the occurrence of mafic to ultramafic

magmas (SiO_2 ~40–52 wt%) (Stockstill-Cahill et al. 2008). However, the silica abundance is higher than 45 wt% at the scale of GRS data, suggesting that ultramafic magmas do not spatially dominate. Examination of the morphology of the olivine-rich outcrops reveals that they are often associated with sandy surfaces, or sand dunes. An apparent olivine enrichment in the sand relative to the bedrock may be explained by aeolian sorting, as observed from basaltic sands on the Earth (Baratoux et al. 2011b) and on Mars (Sullivan et al. 2008), questioning the real occurrence of ultramafic magma. Although the modal abundance of mineral species may be explained by aeolian activity, it remains that the chemical composition of these melts must be compatible with the crystallization of olivine.

3.1.4 Hesperian Volcanism

In contrast to young volcanism, volcanic material of the Hesperian era is well exposed, and is typically represented by Syrtis Major and the Circum-Hellas volcanic province. Based on GRS data, Hesperian volcanic rocks appear to be richer in silica (SiO_2 ranging from 45 wt%–48 wt%), poorer in thorium (0.3 to 0.5 wt ppm), and have iron-rich compositions around 18–20 wt% (Baratoux et al. 2011a; Gasnault et al. 2010). Variations in silica, thorium, and iron content indicate variable degrees of partial melting (Baratoux et al. 2011a), and it has been shown that these trends in composition may be associated with global cooling of the Martian mantle. Results by Baratoux et al. (2011a), who investigated 12 major volcanic provinces of various ages, are compatible with a cooling rate of 30–40 K/Gyr, corresponding to a lithosphere thickening rate of 17–25 km/Gyr and a heat flow decrease from 44 to 32 mW m^{-2} from the Hesperian to the Amazonian period. Inferred values for the mantle temperature and lithospheric thickness are consistent with estimates from experimental studies of Adirondack-class basalt compositions measured in-situ at Gusev crater using the multiple-saturation strategy (Monders et al. 2007).

Spectroscopic observations systematically report the occurrence of two pyroxenes over Hesperian terrains (Bishop et al. 2009; Salvatore et al. 2010; Baratoux et al. 2007; Williams et al. 2010; Mustard et al. 2009) in agreement with the occurrence of clinopyroxene augite and pigeonite in the basaltic shergottites (McSween 1994). Plagioclase is present, as indicated by TES observations (Bandfield 2002) and accounts for the neutral component involved in the deconvolution of visible and near-infrared spectra. Olivine is locally present, but never dominates the mineral assemblage (Koeppen and Hamilton 2008). The pyroxenes are dominated by the calcium-rich end member, with a typical low-calcium pyroxene (LCP) to high-calcium pyroxene (HCP) ratio of $LCP/(HCP + LCP) = 0.2–0.3$ (Poulet et al. 2009a, 2009b). The composition of olivine is difficult to assess from visible and near-infrared spectroscopy as the spectrum of forsterite with large grains and that of fayalite with smaller grains can be similar (Mustard et al. 2005). Nevertheless, Poulet et al. (2009a) have defined spectral indices for both end-members and found that Hesperian pyroxene-rich regions are associated with Mg-rich olivine, consistent with TES observations (Koeppen and Hamilton 2008).

Syrtis Major is a broad 1100 km wide Hesperian-aged volcanic complex with an estimated flow thickness of 0.5–1 km (Schaber et al. 1981; Hiesinger and Head 2004). It has long been a target for studying the volcanic composition of Mars because of its large size and the relative lack of dust cover compared to other regions (e.g., Singer et al. 1982; Mustard et al. 1993). Using the near-infrared Imaging Spectrometer for Mars (ISM), Bibring et al. (1989) documented the presence of both low-calcium and high-calcium pyroxenes (Mustard and Sunshine 1995). Data from the Thermal Emission Spectrometer (TES)

(Christensen and Moore 1992) instrument yielded a regional modal mineralogy of 31 % plagioclase, 29 % HCP, 12 % high-silica phases, 7 % olivine, 4 % LCP, and 17 % other minerals for the low albedo regions of Syrtis Major (Rogers and Christensen 2007). Data from the near-infrared OMEGA instrument are consistent with these results. Poulet et al. (2009c) applied a radiative transfer model based on the Skuratov formulation and derived a modal mineralogy of 34 % HCP, 9 % LCP, 48 % plagioclase, <5 % olivine, and 8 % other. The results are broadly similar for Fe-bearing mafic minerals but differ for the other constituents due to varying sensitivities of the corresponding wavelength region.

Evidence for magmatic differentiation is found in the Nili Patera caldera of Syrtis Major. TES and THEMIS measurements of a small lava flow from a volcanic construct on the caldera floor indicate a dacite composition, which is significantly enriched in SiO_2 relative to the basaltic composition that dominates Syrtis Major (Christensen et al. 2005). The appearance of an eruptive sequence that evolved in composition from basaltic to dacitic suggests that fractional crystallization occurred in the magma chamber associated with the Hesperian Syrtis Major volcano. Although this appears to be an isolated example, it nevertheless makes the case that magmatic differentiation has occurred on Mars.

More extreme magmatic differentiation is suggested by TES and THEMIS observations of what appears to be quartz-rich materials found in craters in the Syrtis Major region (Bandfield et al. 2004; Christensen et al. 2005; Bandfield 2006). Although these materials spectrally resemble granitoid rocks, the possibility remains that secondary processes produced the identified quartz. On the other hand, the association with central peaks in at least two cases suggests excavation from depth and the possibility of a highly differentiated intrusive body.

3.1.5 The Noachian Crust

The originally igneous nature of the Noachian crust has been significantly modified and reworked by impact, erosion, and tectonic processes as well as chemical alteration forming phyllosilicate minerals (Bibring et al. 2006). It is therefore challenging to find unaltered remnants of the early crust. However, at the scale of orbiting spectrometers, it is possible to find significant sections of well-exposed Noachian crust, such as the surroundings of the Isidis basin, characterized by a strong signature of mafic silicates (Hoefen et al. 2003; Hamilton and Christensen 2005; Mustard et al. 2005; Tornabene et al. 2008) associated with phyllosilicates (Bibring et al. 2006; Poulet et al. 2005; Mangold et al. 2007; Mustard et al. 2008; Ehlmann et al. 2009). Concerning the mafic signatures, analysis of spectroscopic data has revealed a clear increase of the LCP/(HCP + LCP) ratio relative to younger volcanic terrains with values up to 0.5 (Poulet et al. 2009a, 2009b; Flahaut et al. 2011). Plagioclase is also present, and olivine-rich outcrops have been reported (Flahaut et al. 2011).

3.2 Chemistry and Mineralogy from in-situ Analysis of Igneous Rocks

3.2.1 Viking Landers

The two Viking landers, which operated from 1976 to 1980 (Viking Lander 2) and to 1982 (Viking Lander 1) in Utopia Planitia and Chryse Planitia, were the first spacecraft to measure the martian regolith in situ. Each was equipped with an X-ray fluorescence spectrometer that provided the first geochemical lander data from the surface of Mars (e.g., Toulmin et al. 1977). However, the capability of the arm-mounted scoop limited sampling to loose regolith rather than the local rocks. Typically described as martian fines or soil, this material is dominated by mafic silicates indurated to varying degree by sulfate-rich cement. Direct measurements of igneous rocks in situ would have to await subsequent rovers.

3.2.2 Mars Pathfinder

The Mars Pathfinder mission, which arrived in Ares Vallis in 1997 and operated for nearly 3 Earth months, combined an immobile lander with a small (<1 m long) mobile rover capable of driving a few 10s of meters. The Sojourner rover was equipped with an alpha proton X-ray spectrometer (APXS) that could be deployed directly onto rock surfaces (e.g., Rieder et al. 1997). Five different rocks were measured with the APXS. Although the measured compositions have significant differences, this is attributed to varying amounts of soil coating the rocks. If these rocks are of igneous origin, as is generally accepted, then their relatively high measured sulfur content (up to 2 wt%) can be attributed to a S-rich soil coating. A soil-free rock composition was determined using linear regressions of rock and soil compositions and the assumption of 0.3 wt% sulfur as the end point (e.g., Foley et al. 2003; Brückner et al. 2003). The result is a rock composition much more felsic (57 % SiO_2) than the mafic soils measured at the Viking and Pathfinder sites. This appears to be consistent with the more andesitic composition of materials concentrated in Acidalia Planitia first recognized from orbit with TES data (Bandfield et al. 2000). However, the possibility that surface alteration on the rocks is responsible for the elevated values of SiO_2 remains a viable alternative (McSween et al. 2009; Horgan and Bell 2012).

3.2.3 Mars Exploration Rovers

The two Mars Exploration Rovers Spirit and Opportunity landed on Mars in 2004, Spirit in Gusev crater, and Opportunity in Meridiani Planum. Both sites were chosen because of evidence in orbital data for the presence of liquid water at the surface during some time in martian geologic history (Squyres et al. 2003). Spirit ceased operating in 2010, while at the time of writing Opportunity continues to operate, although with diminished capabilities. Although neither landing site was chosen to address igneous geology, both have yielded chemical and mineralogical information on martian igneous rocks, most notably in Gusev crater.

Spirit encountered olivine-rich basaltic rocks, subsequently named Adirondack class, which are interpreted to be part of impact-disrupted lava flows on the plains of Gusev crater (Squyres et al. 2004a) and dated by morphological data and crater counts to be 3.65 Ga old (Greeley et al. 2005). These represent the largest occurrence of a single rock type observed by Spirit, but additional igneous rocks were encountered throughout the traverse of the adjacent Columbia Hills, which are embayed by the flows of Adirondack-class basalt. Of the hundreds of rocks observed by the Miniature Thermal Emission Spectrometer (Mini-TES) and 10s of rocks measured with the rover's arm-mounted instruments, five more classes are considered minimally-altered volcanic or volcaniclastic rocks, some in outcrop, others as float rocks. They are mostly basaltic in composition as determined from the rover's APXS instrument, but examples of picrobasalt, trachybasalt, and basanite tephrite have been observed (McSween et al. 2008). Three of the rock classes (Wishstone, Backstay, and Irvine) have alkalic compositions as determined by APXS, constituting the first definitive alkaline rocks on Mars and perhaps indicative of fractional crystallization at various depths of oxidized, hydrous basaltic magmas similar in composition to Adirondack-class rocks (McSween et al. 2006). The basalt compositions measured by Spirit have been used as the basis for laboratory studies of mantle melting conditions on early Mars, such as melting temperature, pressure range, and melt fraction (Monders et al. 2007; Filiberto et al. 2008, 2010).

Mineralogically, the igneous rocks in Gusev crater can be grouped according to the dominant silicate phase as identified with Mini-TES spectra (Arvidson et al. 2008). Olivine-rich rocks abound, represented by the Adirondack-class basalts and Algonquin-class picrobasalts. Pyroxene dominates the spectra of Backstay and Irvine class alkaline rocks. In a notable departure from any martian meteorites, plagioclase is the dominant phase in the Al-rich Wishstone-class tephrites found as cobbles and boulders covering the north side of Husband Hill (Ruff et al. 2006). These results are consistent with measurements by Spirit's Mössbauer spectrometer (MB), although only Fe-bearing phases are sensed with this technique. Among these, hematite typically is observed in much lower abundance relative to magnetite, a reflection of the generally low oxidation state of Gusev's minimally altered igneous rocks (Morris et al. 2008).

The Meridiani Planum landing site encountered by Opportunity along its >30 km traverse is dominated by sulfate-rich sedimentary outcrops covered by a lag of basaltic sand and gray crystalline hematite spherules that are likely to be groundwater-derived concretions (e.g., Squyres et al. 2004b; Grotzinger et al. 2005). Igneous rocks along the traverse are limited to various cobbles that were likely delivered by impact processes or are themselves meteorites (e.g., Schröder et al. 2008). A well-studied example of likely impact ejecta known as Bounce Rock is rich in pyroxene to the exclusion of all other Fe-bearing phases as determined from MB data, despite its basaltic composition (Squyres et al. 2004b). In both its chemistry and mineralogy, Bounce Rock is similar to the martian shergottite meteorite EETA79001 Lithology B, although not a direct match as determined by a comparison of Mini-TES and laboratory spectra (Christensen et al. 2004; Zipfel et al. 2011). There is evidence to suggest that Bounce Rock was ejected from a relatively fresh $\sim$25 km crater located 75 km southwest of Opportunity's landing site, which exposed volcanic material different from the basaltic sands that partially cover Meridiani Planum (Squyres et al. 2004b).

3.3 Martian Meteorites

Martian meteorites are called the SNC group after three of its end members, the shergottites, nakhlites, and chassignites. In the absence of other samples, these rocks are the only pieces of Mars that may be analyzed in the laboratory on Earth to study in detail the magmatic processes affecting the crust-mantle system, from its differentiation up to the most recent events represented in the present collection. At the time of writing, the SNC group is a set of 104 igneous rocks (including pairs) (Meyer 2009), all of which have oxygen isotope compositions related to each other by a common mass fractionation trend (Clayton and Mayeda 1996), indicating an origin from the same planetary body. The definitive link to Mars was made from the isotopic composition of trapped atmospheric gases extracted from shock melt pockets of shergottites, which is identical to the martian atmospheric composition as determined by the Viking landers (Bogard and Johnson 1983). Relatively young crystallization ages (Nyquist et al. 2001) of all the SNCs (shergottites between 450 and 175 Ma, nakhlites and chassignites 1.3–1.4 Ga, but see Sect. 3.3.6 for a discussion of shergottite ages) have been considered as indirect evidence for a martian origin. The exception is ALH 84001, for which age estimates range from 3.8–4 Ga (Ash et al. 1996) to 4.56–4.5 Ga (Jagoutz et al. 1994; Nyquist et al. 1995), with most recent studies narrowing the age to 4.091 ± 0.030 Gyr (Lapen et al. 2010).

The time of ejection of the SNC meteorites from the martian surface is estimated from Cosmic Ray Exposure data obtained from cosmogenic nucleide measurements (Christen et al. 2005), and exposure times between 1 and 20 Myr have been obtained. The entire

collection of martian meteorites appears to sample six different as yet undetermined localities (Meyer 2009). The most representative samples are the shergottites, which originate from four distinct sites and constitute 78 % of the SNCs discovered so far. However, despite the general assumption that the SNC meteorites have young crystallization ages young volcanic surfaces are remarkably sparse, representing less than 20 % of the planet's exposed surfaces (Hartman and Neukum 2001). Sampling of the martian crust by the SNCs would thus be highly biased towards young igneous rocks. Furthermore, it should be noted that spectral analysis of the martian surface does not provide a perfect match to the spectral signature of the SNC meteorites (Hamilton et al. 2003; Lang et al. 2009). However, this may be due in part to the fact that young volcanic rocks such as those found in Tharsis and Elysium are hidden by dust.

3.3.1 Petrology

The unpaired shergottites are sub classified on mineralogical grounds into three classes (McSween and Treiman 1998), and 46 different specimen have been discovered so far: 16 basaltic (Shergotty, Zagami, Los Angeles, 2 from Antarctica, 11 from Sahara); 10 lherzolitic (8 from Antarctica and 2 from Sahara) and 20 picritic (Tissint, 14 from Sahara, 2 from Antarctica, 2 from Oman and 1 from Libya).

Basaltic Shergottites have a tholeitic basaltic composition. They consist predominantly of coarse pyroxene crystals (augite and pigeonite) with lesser amounts of maskelynite (diaplectic glass formed from plagioclase during impact). The pyroxenes are typically zoned with Fe-rich rims. The proportion of pyroxene varies from 70 % in Shergotty to 44 % in QUE 94201, while that of maskelynite is 22–47 % (Meyer 2009). In more detail, pyroxenes are pigeonite 36–45 % and augite 10–34 %. Minor phases are oxides (titanomagnetite, ilmenite), sulfides (pyrrhotite) and accessory apatite, quartz, baddeleyite, and fayalite. Based on textures (coarse grain size) and high pyroxene/plagioclase ratio that cannot represent cotectic melt, most basaltic shergottites are considered as basaltic cumulates, which crystallized from fractionated melt (Usui et al. 2009). QUE 94201 is an exception as pyroxene core compositions are consistent with formation from a melt with the composition of the bulk sample (Kring et al. 2003). The shergottites range in oxygen fugacity from 3-log units below the Quartz-Fayalite-Magnetite (QFM) oxygen buffer to one log unit below QFM (QUE94201 < EET 790001, Zagami, Los Angeles, and Shergotty). QUE 94201 is the least oxidized shergottite (FMQ-3) (Herd et al. 2002; McSween 1994).

Picritic Shergottites are basalts containing up to 7–29 % large (1 to 3 mm across) olivine grains. Picritic shergottites as a whole seem to be the least affected by crystal accumulation processes. Goodrich (2002) described large zoned olivine grains ($Fo_{60–76}$) as phenocrysts, and pyroxene in picritic shergottites is richer in Mg compared to basaltic shergottites. At least 4 picritic shergottites (Y 980459, NWA 5789, NWA 2990, and NWA 6234) represent magma compositions (Musselwhite et al. 2006; Gross et al. 2012; Filiberto and Dasgupta 2011). LAR 06319, which has been suggested to represent a near magma composition, actually contains ~11 wt% excess olivine (Filiberto and Dasgupta 2011). Picritic shergottites contain chromites rather than Ti-magnetite and ilmenite as the main oxide phases. The sulfides are coarse blebs of pyrrhotite-pentlandite association (Lorand et al. 2005). DAG 476 is the least oxidized picritic shergottite (QFM-2.47 ± 0.73, Herd et al. 2002)

Lherzolitic Shergottites consist of medium grained olivine (40–60 %) and chromite, poikilitically enclosed by large (up to 5 mm) pigeonite / orthopyroxene crystals (9–25 %). Minor phases include maskelynite (less than 10 %), augite, whitlockite, and chromite filling the interstices. They are interpreted as olivine and pyroxene ultramafic cumulates possibly formed at depth.

Nakhlites and Chassignites are clinopyroxenite and dunite cumulates, respectively, and only represent 20 % of the meteoritic falls. The 8 nakhlites (Nakhla, Lafayette, Governador Valadares, 2 from antarticca, 3 from Sahara) are all olivine-bearing clinopyroxenites with cumulate textures defined by coarse augite and olivine crystals set in fine-grained mesostasis of silica-rich phases, oxides, sulfides, and phosphates. The coarse crystals hint at a rather slow growth over a relatively long period of time (>100 yr) within a single subsurface magma chamber or series of related but distinct flows (Lentz et al. 1999; Day et al. 2006), whilst the mesostasis corresponds to faster cooling as crystal mushes were extruded to the surface. Assuming a single thick lava flow or magma chamber environment, subtle mineralogical and chemical differences have been used to classify the 8 nakhlites in a stratigraphic order (Mikouchi and Miyamoto 2002). The nakhlites contain very small proportions of Cu-Ni-Fe sulfides. They thus show low modal sulfide abundances about five times lower than shergottite lavas (Lorand et al. 2005). The two Chassignites (Chassigny, Sahara) are olivine-rich cumulates with minor pigeonite, augite, alkali feldspar, chromite, troilite, pentlandite, chlorapatite, ilmenite, rutile, and baddeleyite (Floran et al. 1978; Beck et al. 2006). In the type specimen Chassigny, olivine is Fo_{68} whilst it is Fo_{78} in the only other known chassignite NWA 2737.

AllanHills (ALH 84001) is a unique sample that was added to the SNC classification (Mittlefehldt 1994). It is a coarse grained, cataclastic orthopyroxenite, consisting of 97 % orthopyroxene up to 5 mm long, 2 % chromite, 1 % maskelynite, and 0.15 % phosphate, with minor augite, olivine, and secondary Fe-Mg-Ca carbonates. Orthopyroxene is $En_{70}Fs_{27}Wo_3$, olivine is Fo_{65}, and maskelynite is $An_{35}Ab_{62}Or_3$.

3.3.2 Geochemistry

Shergottites Abundant geochemical data are available for the shergottites (see, e.g., McSween and Treiman 1998 and Meyer 2009) including trace element data (Treiman et al. 1986) and various isotopic ratios (Borg et al. 2002). The variation of mineralogy between the three groups translates into variable magnesium numbers Mg#, defined as $100 \times Mg/(Mg + Fe)$, where Mg and Fe are the magnesium and iron mole fractions. Basaltic shergottites vary from Mg# 23 (Los Angeles) to Mg# 52 (Zagami); picritic shergottites vary from Mg# 58 to Mg# 68, and lherzolitic shergottites have Mg# > 70. The Mg# of a rock is a function of both magmatic differentiation (liquids becoming more iron-rich as crystallization proceeds) and crystal content (mafic minerals having higher Mg# than their coexisting liquids). In the case of the Shergottites, the fact that Mg# correlates with decreasing SiO_2 concentration indicates significant olivine accumulation. Oxygen fugacities vary by 3 log units between the most and least reduced samples, the former of which have fO_2 equal to −3 log QFM units (close to the IW buffer) (Herd et al. 2002). All shergottites have low total alkali and Al_2O_3. A super-chondritic ratio of CaO/Al_2O_3 reflects a high pyroxene/plagioclase ratio. Sulfur concentrations in shergottites are high (from 500 to 3000 ppm) (Lorand et al. 2005 and references therein). The parallel decrease in pentlandite/pyrrhotite ratio, Ni concentration in pyrrhotite, and bulk rock Mg# indicates that: (1) sulfides are comagmatic; and (2) sulfide melts segregated from progressively more evolved (i.e. Mg- and Ni-depleted) silicate melts.

Shergottites may be sub classified into three groups based on Rare Earth Elements (REE) geochemistry: The Light REE (LREE)/Heavy REE (HREE) ratio varies from LREE highly depleted (HD) shergottites[1] (QUE 94201, DAG 476, Y 980459, NWA 5789, and NWA 6234) to moderately depleted (MD) shergottites and slightly depleted (SD) shergottites. Here, depletion refers to the incompatible behavior of Rare Earth Elements with respect to major minerals formed during igneous differentiation. Most HD shergottites are picritic, but QUE 94201 is a basaltic shergottite (Kring et al. 2003). Most MD are lherzolitic shergottites, and most SD shergottites are basaltic. This geochemical classification correlates only weakly with the mineralogical subclasses, but geochemical subclasses correlate with fO_2: less oxidized shergottites such as QUE 94201 and DAG 476 are HD, while the more oxidized ones are SD (Herd et al. 2002).

During igneous differentiation, the incompatible alkalis and LREE concentrate in the primary crust, leaving behind a depleted mantle. SD shergottites with flatter REE profiles correspond to an enriched reservoir that may reside inside the crust. The fO_2 variation would be due to mixing between reduced mantle-derived basalts and an oxidized crust-like reservoir. The correlation between the degree of geochemical contamination and magmatic oxidation state could be consistent with crustal assimilation (Herd et al. 2002), although Re/Os isotopic data argue for contamination in the mantle, (Brandon et al. 2000, 2012; Debaille et al. 2008). The geochemical characteristics of the shergottites have been modified by fractionation and/or assimilation during ascent, except for the HD shergottites QUE 94201, DAG 476, Y 980459, NWA 5789, and NWA 6234. These rocks are unfractionated and uncontaminated by enriched components. Therefore, the compositions of these samples represent equilibrium crystallization from the most primitive primary mantle melt, which could have equilibrated at a depth of 80–100 km in the martian mantle (Musselwhite et al. 2006).

Exposure ages (Nyquist et al. 2001) define at least four different groups of shergottites, excluding the interpretation that they would have been extracted by a single impact event. Rather, they likely correspond to four distinct sites on Mars.

Nakhlites, Chassignites and ALH84001 Nakhlites and chassignites represent a rather homogeneous set of meteorites. Sharing the same cosmic exposure age (11 ± 1.5 Ma), they likely originate from the same locality on Mars (Nyquist et al. 2001; Treiman 2005). Their Mg# is quite constant and around 50 for nakhlites, between 68 and 78 for chassignites, and 72 for ALH 84001. They are cumulate rocks which are not representative of the primary melt. Trapped melt inclusions in olivine and augite cumulus crystals are the only way to reconstruct the most primitive melt from which these cumulates crystallized (Treiman 2005 and references therein). In nakhlites, the recalculated parental melt has a Mg# of 29, much more iron rich than liquids produced by partial melting of the (Dreibus and Wänke 1985) mantle composition (DW85) at reasonable depths and degrees of partial melting (for which Mg# is typically 50) (Sautter et al. 2012). In contrast to the shergottites, nakhlites and chassignites are LREE-enriched (Nakamura et al. 1982), and they are depleted in sulfide components. ALH 84001 has an unusually old cosmic ray exposure age (15 Ma) for a martian meteorite, and a mineral composition similar to those of lherzolitic shergottites. It is LREE depleted, but its absolute abundances of REE are lower than in lherzolitic shergottites.

3.3.3 Comparison between SNCs and in-situ Analysis

The Gusev magmatic province is now the most thoroughly characterized igneous site on Mars. The Mars Exploration Rover Spirit has encountered mainly unaltered basalts, first

[1] It is of note that the following terminology is also often used: Depleted shergottites (equivalent to HD), Intermediate shergottites (equivalent to MD) and Enriched shergottites (equivalent to SD).

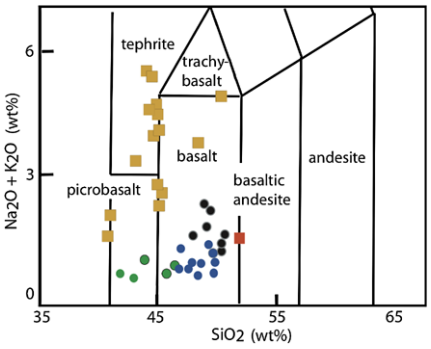

Fig. 5 Total alkali vs. silica (TAS) diagram used for the classification of volcanic rocks. Squares refer to rocks analyzed in situ by the Spirit and Opportunity rovers (Gusev rocks are indicated in *yellow*, while Bounce rock at Meridiani Planum is indicated in *red*). Dots refer to SNC meteorites, where *black dots* represent basaltic shergottites, *blue dots* represent picritic shergottites, and *green dots* represent lherzolitic shergottites

in the Gusev plain, and subsequently in the Columbia Hills. Major and minor elements were determined by APXS, Mini-TES investigated the mineralogy of rocks remotely in the thermal infrared, and Fe-bearing minerals were identified by the Mossbauer spectrometer. Most Gusev basalts are fine-grained with few olivine phenocrysts visible in the microscopic images down to about 100 microns resolution. They range from picritic basalts to alkali basalts (Fig. 5) and four classes are distinguished by element composition (McSween et al. 2008): (1) Adirondack-class basalts which consist of olivine and pyroxene bearing blocks on the Gusev plain (McSween et al. 2004). (2) Backstay-class basalts that include fine-grained olivine-, pyroxene-, ilmenite-, and magnetite bearing float rocks near the crest of Husband Hill. (3) Irvine-class rocks that include massive to vesicular pyroxene magnetite bearing rocks found on the flank of Husband Hill and in the inner basin of the Columbia Hills. (4) Algonquin-class rocks that are picritic basalt containing variable amounts of coarse crystals of cumulus olivine.

Gusev alkali and picritic basalts differ from the shergottites as they are all fairly silica-poor and generally have higher total alkali abundance as well as Al_2O_3 and Na_2O, and lower Al_2O_3/CaO relative to the shergottites. They are all fairly oxidized iron-rich basalts with a narrow range of Mg# from 51–55 (McSween et al. 2006) consistent with that calculated from primary melts in equilibrium with a DW 85 mantle (Mg# 75). All rocks from Gusev, except for Wishstone-class of P and Ti-rich basalts interpreted as pyroclastic rocks, can be related through fractional crystallization of a common parental magma at depths ranging from the mantle source at 85 km depth to the near surface. Adirondack class rocks only represent unfractionated picritic basalt while Algonquin class rocks accumulated olivine crystals on their way to the surface (McSween et al. 2006).

The Picritic shergottite that looks the most like Adirondack class rock with approximately the same proportion of olivine phenocrysts (10 to 20 %, Meyer 2009) is DAG 476. Olivine core composition (Fo76) is consistent with that expected from olivine crystallizing from primary magma derived from 15–20 % partial melt of a DW85 mantle source at 85 km depth (Bertka and Fei 1997; Schmidt and McCoy 2010; Baratoux et al. 2011a). Therefore, picritic basalts of Gusev (the Adirondack class) and picritic shergottite could be derived from the same source. Consequently olivine-phyric shergottites provide the most direct analogue to Gusev picritic basalt. The two basaltic shergottites EET 79001B (Steele and Smith 1982) and QUE 94201 are fine-grained with sub-ophitic textures. They are pyroxene-rich rocks dominated by low-Ca pyroxene (pigeonite) with subordinate high-Ca pyroxene (augite) similar to Bounce Rock.

All SNCs, except for the picritic shergottites such as DAG 476 and some of the basaltic shergottites (QUE 94201) are cumulates. Thus they are hypo-volcanic rocks (i.e., not surface rocks) as opposed to Gusev Adirondack-class rocks, which are extrusive olivine-rich

basalts very similar to the picritic shergottites. All SNCs, except for the chassignites, are pyroxene-rich and plagioclase-poor while the martian surface is dominated by true basaltic rocks in which pyroxene and plagioclase proportions are similar. This indicates some degree of differentiation at depth by fractional crystallization. Such a subsurface origin for the shergottites would explain why no spectral signature related to these lithologies has been found from orbital measurements. This implies limited erosional or tectonic exposure of the subsurface and sampling at depth during strong impacts. Moreover, cosmic ray exposure ages are short (a few million years) with respect to the age of the SNCs, indicating that the specimens were shielded from interaction with cosmic rays, and buried at some depth below the surface.

3.3.4 Magnetic Properties

Ultramafic cumulates (i.e. Chassigny, ALH 84001) and lherzolitic shergottites are too weakly magnetized to account for the observed crustal magnetization (Acuña et al. 2008), assuming that magnetization took place in an Earth like magnetic field (Rochette et al. 2005). Basaltic shergottites and nakhlites are the most strongly magnetized SNCs, and in nakhlites the magnetic carrier is titanomagnetite. However, magnetization in nakhlites may be shock induced or linked to their shallow emplacement, and therefore they may not be representative of deeper unshocked rocks. In most basaltic shergottites pyrrhotite—a magmatic phase composed of iron sulfide (Lorand et al. 2005)—is the carrier of magnetization (Rochette et al. 2001). However, pyrrhotite magnetization was likely acquired during post-impact pressure release, and not from thermal remanence (Rochette et al. 2001). Furthermore, it should be noted that apart from ALH 84001 the SNCs are apparently much younger (<1.2 Ga) than the inferred 4 Ga lifetime of the martian dynamo (Langlais et al. 2004).

3.3.5 Water Content

The bulk water content of the SNC meteorites is one of the few constraints available to estimate the amount of water in the Martian mantle. This is of importance as the solidus (Sect. 5.1) and rheology (Sect. 4.2) of mantle rocks strongly depend on water content. Even just a few tens of ppm water can significantly reduce viscosity, and water content above $\sim$100 ppm will notably reduce the mantle solidus. The bulk water content of the SNC meteorites is relatively small and ranges from 50 to 150 ppm (Leshin et al. 1996), indicating low mantle water contents in the source regions of the SNC meteorites between only 5 and 15 ppm (Filiberto and Treiman 2009). However, it has been argued that magmatic degassing could be responsible for the low bulk water content in the SNC meteorites (McSween et al. 2001), and the water content of the martian mantle could be considerably larger. As of now, the water content of the martian mantle remains the subject of ongoing debate, and while some studies argue that water contents could be as low as 1–36 ppm H_2O (Mysen et al. 1998; Filiberto and Treiman 2009), making the martian mantle dryer than that of the Moon (Hauri et al. 2011), others derive water contents of 55 to 220 ppm H_2O (McCubbin et al. 2010; McCubbin et al. 2012), values similar to that of the Earth's mantle.

Evidence for a high mantle water content comes from studies of the depleted shergottites, which have an unambiguous mantle origin, and which are derived from partial melt that has not been mixed with an enriched component (either crustal or metasomatic). Olivine and pyroxene hosted primary melt inclusions, which contain trapped apatite and amphibole crystals, directly sample the water reservoir of the martian mantle, provided they have not been altered by terrestrial or martian weathering. Apatites in basaltic shergottites span a

range of H_2O contents similar to those found in terrestrial mafic minerals (McCubbin et al. 2012), and based on apatite-melt partition coefficients for water, shergottite magmas should have contained 1.5 to 2.85 wt% H_2O at the time of apatite crystallization (McCubbin et al. 2012). This implies a much higher bulk water content in the parental melt than what is currently present in the shergottites, consistent with significant degassing. Taken together, apatite data indicate that water contents in the source regions of the depleted shergottites range from approximately 55 to 160 ppm H_2O (Watson et al. 1994; Leshin 2000; McCubbin et al. 2012), very similar to values estimated for the martian mantle from kaersutite in the Chassigny meteorite (McCubbin et al. 2010). For the enriched shergottites, a water content of 120–220 ppm H_2O has been estimated, although it remains controversial whether the source of this water is from a mantle or crustal reservoir (McCubbin et al. 2012). Taken together, evidence from the SNC meteorites indicates that rheologically significant amounts of water are likely present in the martian mantle, while it remains to be seen whether water content is also petrologically significant.

3.3.6 Dating the SNC Meteorites

The time of crystallization of the shergottites has been a controversial subject because discordant values have been obtained using different chronometric methods. As the mineralogy and chemistry of the shergottites have been used to infer the composition of their respective source regions as well as the conditions during partial melting, their crystallization age is highly relevant to the reconstruction of the composition and evolution of the crust-mantle system. If crystallization occurred relatively recently, derived water contents and melting conditions could represent a reservoir in the present-day martian mantle, while old ages would indicate the almost primordial state of the mantle shortly after core formation.

Young ages for the shergottites (late Amazonian period, 160–650 Ma) are obtained using U-Pb, Sm-Nd, Rb-Sr, Ar-Ar and Lu-Hf chronometers (Nyquist et al. 2001 and references therein), but an old late-Noachian to early Hesperian age of 4 Ga has been inferred from Pb isotope systematics in earlier studies (Chen and Wasserburg 1986; Jagoutz and Wänke 1986). Old crystallization ages have been confirmed by Bouvier et al. (2005, 2008, 2009) based on the same Pb geochronometer, and it has been argued that the young age isochrons for the shergottites date the last isotopic resetting due to impacts or acidic hydrothermal alterations (Bouvier et al. 2005, 2008, 2009), rather than the crystallization age. Different but still young Rb-Sr and Sm-Nd ages have been obtained for QUE 94201 (Borg et al. 1997) and DAG 476 (474 ± 11 Ma, Borg et al. 2000) interpreted as indicating that more than one perturbation event such as hydrothermal acidic leaching occurred on the martian surface (Bouvier et al. 2005).

The difference between old ^{206}Pb–^{207}Pb ages and young ages from other chronometers is not simple to interpret. Usually, a discordance between different chronometers is related to the robustness of their respective host-phases to contamination and disturbance events such as (shock) metamorphism. Bouvier et al. (2005, 2008, 2009) justified their hypothesis of the shergottites being old by arguing that Pb is mainly located in maskelynite that is robust to Pb diffusion during metasomatic events, while REE are mainly held in phosphates, a phase highly prone to disturbance. However, it is noteworthy that their very high content in REE makes metasomatic fluids less efficient for a complete resetting of their trace element contents. Also, other robust mineral phases, such as high-Ca pyroxene, can contain a substantial amount of REE (Wadhwa et al. 1994; Hsu et al. 2004). On the other hand, maskelynite is a glassy mineral resulting from the melting of plagioclase after a high-pressure shock event (Chen and El Goresy 2000), and glassy

structures in which crystallographic bounds have been broken would be more prone to disturbance following metasomatic and/or metamorphic events (Ostertag and Stoffler 1982; Gaffnee et al. 2011).

There is good agreement between Rb-Sr, Sm-Nd, and Lu-Hf chronometers, despite their being hosted by different minerals: For Rb-Sr, maskelynite and to a lesser extent low and high-Ca pyroxene indicate that minerals cannot have been randomly reset (e.g., Borg et al. 2002). Similarly, phosphates and to a lesser extent high-Ca pyroxene indicate the same for the Sm-Nd and Lu chronometers (e.g., Wadhwa et al. 1994), while maskelynite shows the same for the Hf chronometer (e.g., Bouvier et al. 2005, 2008). Given the different robustness of each host-phase, a shock event followed by metasomatism would have deeply perturbed the different chronometers, and no consistency would be observed between the derived ages. This is confirmed by shock and heating experiments in which Rb-Sr and Sm-Nd remain preserved after heating the samples to 1000 °C and exposing them to shocks of 55 GPa (corresponding to the inferred conditions suffered by the shergottites), while U-Pb and even more ^{207}Pb–^{206}Pb are perturbed (Gaffnee et al. 2011). Thus the geochronological evidence suggests a young age for the shergottites, but the old ^{206}Pb–^{207}Pb systematic still needs to be explained.

Apart from geochronological arguments, aluminum depletion of the SNCs relative to terrestrial rocks as well as the Hesperian rocks of Gusev crater has been used as a geochemical discriminant to argue that the SNCs result from an Al-depleted evolved mantle source region left behind after early extraction of a primitive aluminum-rich crust (McSween 2002). This would support a young age of the shergottites relative to Gusev rocks. However, this super-chondritic ratio in the shergottites could be a mineralogical effect due to clinopyroxene fractionation and accumulation rather than a geochemical feature inherited from the deep mantle source. On the other hand, several indirect lines of evidence may suggest that shergottites are late Noachian to early Hesperian. First of all, shergottites are magnetic and the magnetic crust on Mars is exclusively Noachian (Rochette et al. 2005 and references therein). Furthermore, being S-rich, shergottites are not devolatilized, whilst younger nakhlites and chassignites are S-poor (Lorand et al. 2005; Chevrier et al. 2011). Finally, the most primitive uncontaminated and unfractionated shergottites (QUE 94201 and DAG 476) appear to be derived from partial melt of a primitive mantle source with DW85 composition.

4 Rheology and Tides

4.1 Lithospheric Deformation

The lithosphere comprises the crust and upper mantle, and its susceptibility to deformation can be described by strength-depth profiles of the corresponding crustal and mantle materials, which indicate the amount of stress that can be supported. In the cold (shallow) regions, the strength is controlled by the fracture strength, whereas in the deep (hot) regions the strength is controlled by the resistance to ductile flow. Such general strength profiles were first proposed by Goetze and Evans (1979), and a schematic profile is shown in Fig. 6. In this model, the strength of materials in the brittle regime is controlled by the frictional strength along preexisting faults and is generally insensitive to the specific materials (except for sheet silicates that have a smaller resistance to friction).

Using this so-called yield-strength envelope model, the mechanical and elastic thickness of the lithosphere can be defined, where the former corresponds to the depth up to which the

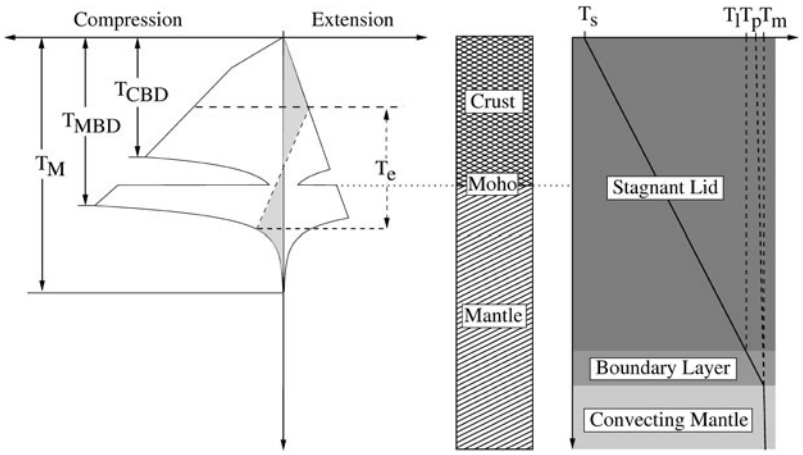

Fig. 6 Schematic diagram showing the relationship between elastic lithosphere thickness T_e, mechanical lithosphere thickness T_M, and the depth to the brittle-ductile transition in the crust (T_{CBD}) and mantle (T_{MBD}). T_e is defined by the depth range over which stresses are supported elastically, here indicated by shades. The chemical layering of the lithosphere is shown in the mid-column, while dynamical denominations are given in the right panel along with their corresponding temperatures: T_s is surface temperature, T_l is the temperature at the base of the stagnant lid, and T_m is upper mantle temperature. T_p is the mantle potential temperature, which is calculated by extrapolating T_m to the surface using the adiabatic temperature gradient in the mantle

lithosphere carries significant mechanical strength (usually assumed to be 10 to 50 MPa). Deformation of the lithospheric plate will then result in the generation of bending stresses, and brittle as well as ductile yielding will take place wherever stresses exceed the limits defined by the yield strength envelope. The elastic thickness of the lithosphere T_e can then be defined as the thickness of a purely elastic plate which carries the same bending moment as the real elasto-plastic plate defined by T_M.

For the two-layer rheology considered in Fig. 6, the yield strength envelope consists of two domains, each corresponding to one homogeneous chemical layer. Usually, crust and upper mantle are both part of the elastic and mechanical lithospheres, and both are generally part of the stagnant lid, in which heat is transported by conduction. Only deeper parts of the mantle located at depths larger than the stagnant lid thickness will convect, and temperatures in the convecting region will increase along the adiabatic temperature gradient.

Due to the reduced gravity on Mars and the associated reduced lithostatic pressure, the brittle strength of the lithosphere is only $\sim 1/3$ that of the Earth. Ductile deformation is governed by plastic flow laws of the corresponding material and is sensitive to temperature, but water content also plays an important role. Consequently, the transition from the strong lithosphere to a weak asthenosphere depends both on the temperature-depth and the water content-depth profiles, as indicated in Fig. 7.

The asthenosphere is situated directly below the lithosphere and comprises a region in the upper mantle which deforms plastically on geological timescales. Partial melting predominantly occurs at depths below the lithosphere, and the location of the lithosphere—asthenosphere boundary can be identified with an isotherm. The depth of the lithosphere—asthenosphere boundary is the depth below which deformation is dominated by viscous flow, and this region is characterized by a Maxwell time

$$\tau_M = \frac{\eta_{\text{eff}}(z)}{E} \tag{1}$$

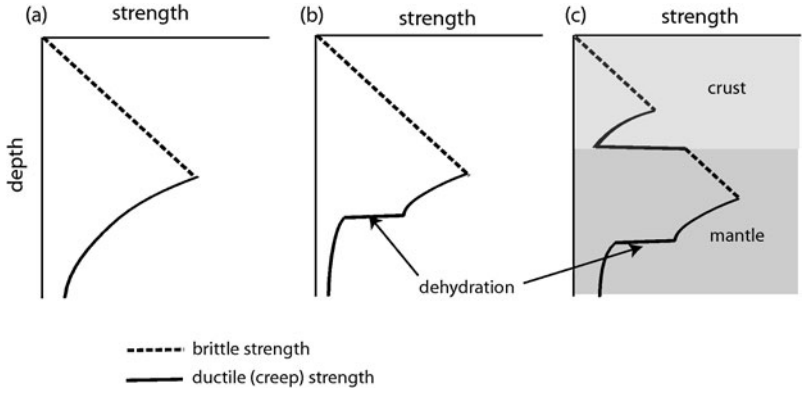

Fig. 7 Schematic diagrams showing lithospheric strength-depth profiles. (**a**) Homogeneous lithospheric composition with only temperature and pressure dependent creep strength. (**b**) Same as (**a**), but including the water content dependence of the creep strength. A water-depleted (dehydrated) layer above the indicated depth is assumed. (**c**) Layered lithospheric composition including crust and mantle. A layered water content similar to (**b**) is assumed

which becomes shorter than the time scale of deformation τ. Here, η_{eff} is the effective viscosity, and E is the elastic modulus. For two-dimensional flow, the effective viscosity is defined as (e.g., Karato 2008)

$$\eta_{\text{eff}} = \frac{\sigma}{2\dot{\epsilon}} \tag{2}$$

where σ is stress and $\dot{\epsilon}$ is strain-rate. The latter may be expressed as a power-law relationship, and if the grain-size dependence is ignored for simplicity, $\dot{\epsilon}$ is given by

$$\dot{\epsilon} = \left(A_{\text{dry}} + A_0 C_W^r\right) \exp\left(-\frac{H^*}{RT}\right) \sigma^n \tag{3}$$

where A_{dry} and A_0 are deformation constants, T is temperature, R is the gas constant, C_W is water content, r is a non-dimensional parameter representing the water sensitivity of deformation (close to 1–1.2 for high temperature creep in olivine), H^* is activation enthalpy, and n is the stress exponent. Consequently, the lithosphere will appear thick for deformation at a low stress level and thin for deformation at high stress levels.

The dependence of the effective viscosity on water content is caused by hydrogen, which enhances transport properties if dissolved in silicates such as olivine. The precise mechanisms of enhancement are not well understood, but enhancement is partly due to the increased population of point defects such as atomic vacancies created by hydrogen (e.g., Chapter 10 of Karato 2008). In many cases, even a small amount of hydrogen can significantly affect transport properties, and the critical water content above which viscosity is significantly reduced can be estimated by comparing the relative importance of A_{dry} and $A_0 C_W^r$ in Eq. (3). For high-temperature (dislocation) creep in olivine, the critical water content at which $A_{\text{dry}} = A_0 C_W^r$ is only 2 ppm wt (~30 ppm H/Si) (Mei and Kohlstedt 2000a). This implies that if the water content is close to 100 ppm wt, then the viscosity is reduced by a factor of ~50 from the completely dry situation. Therefore, a few tens of ppm water can be rheologically significant, but the exact value depends on the operating deformation mechanism. As limiting cases, viscosities of 10^{19} and 10^{21} Pa s at a temperature of 1600 K are generally assumed to represent wet and dry mantle rheologies.

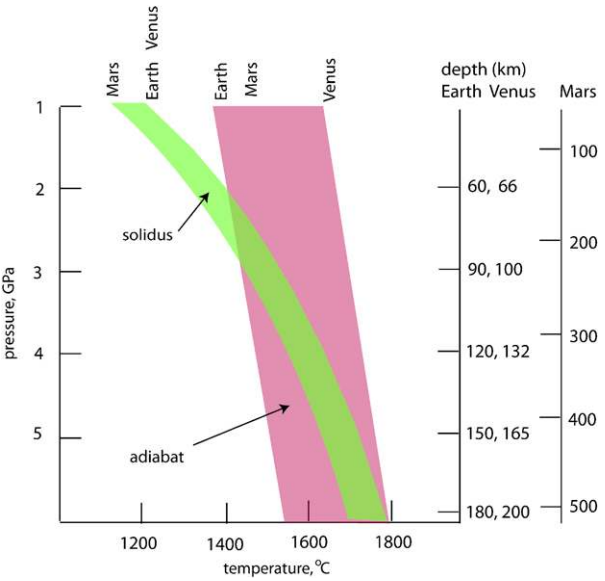

Fig. 8 A diagram illustrating the extent of a potentially dehydrated zone in the mantles of Earth, Venus, and Mars. Substantial dehydration will occur if mantle materials undergo a large degree of partial melting, and assuming a partitioning coefficient of 0.01, the residual mantle will be more than 90 % dehydrated at melt fractions larger than 10 %. The depth of partial melting corresponds to the depth at which the solidus intersects the adiabat. Due to the iron-rich composition, the dry solidus of the martian mantle is lower than that for the Earth

The water content of the martian mantle is poorly constrained, but it seems likely that the minimum estimates of water concentrations (see Sect. 3.3.5) are sufficient for rheological weakening. In addition, the water content in the martian mantle may be stratified, as has been proposed for Earth's upper mantle (e.g., Karato 1986; Hirth and Kohlstedt 1996), and this stratification would be associated with a large change in the effective viscosity as a function of depth. A potential stratification in water content on Mars could be the consequence of partial melting, which results in dehydration of the mantle minerals. The depth range of melting depends on the relative positions of the adiabat and the solidus, and the depth to which a potential stratification in water content would occur on Mars is expected to be deeper than on either Earth or Venus (Fig. 8). Furthermore, dehydration stiffening only becomes efficient near the dry solidus, as even small amounts of water can significantly reduce the viscosity (Hirth and Kohlstedt 1996; Karato and Jung 1998).

4.2 Mantle Rheology

Below the lithosphere, much of the deformation occurs via plastic flow through thermally activated motion of atoms, and the rheological properties of the martian mantle play a key role for the thermal and chemical evolution of the planet. Rheology influences processes like crustal production and possibly also the history of the magnetic field (Breuer and Spohn 2006). The interpretation of lithosphere thickness (Sect. 4.4) also requires some knowledge of rheological properties. The rheological properties of minerals in the ductile regime depend on temperature, pressure, water content, grain-size and mineralogy (major element chemistry and crystal structure) (Karato 2008), with water having a significant influence on the strength of mantle minerals.

Mantle mineralogy is similar on Mars and Earth, with a modest increase in Fe content (e.g., Ohtani and Kamaya 1992; Bertka and Fei 1997), which reduces the viscosity at a given stress by a factor of ∼3–5 (see Fig. 4 of Zhao et al. 2009). In addition, a higher Fe content

reduces the pressure at which a phase transformation from olivine to wadsleyite or ringwoodite occurs by up to ∼0.5 GPa. Consequently, the rheological properties of the martian mantle likely follow a trend similar to the Earth's mantle, with minor modifications caused by the influence of Fe content and potentially larger modifications caused by differences in water content.

For mantle minerals of the Earth, detailed data sets on olivine (and olivine-dominated rocks) exist that can be applied to a depth of ∼1000 km on Mars. From a depth of ∼1000 to ∼1800 km, the martian mantle is mainly composed of wadsleyite, ringwoodite and majorite, for which experimental data on rheological properties are sparse (e.g., Nishihara et al. 2008; Kawazoe et al. 2010). At the very bottom of the martian mantle (from ∼1800 to ∼2000 km), a thin layer made mostly of perovskite and (Mg,Fe)O may exist, depending on core size, and the rheological properties of materials below ∼1000 km must be viewed as highly uncertain. In addition, a possible difference between the rheological behaviour of the martian and terrestrial mantle could be related to the larger fraction of the martian mantle that is composed of wadsleyite and ringwoodite, which can store a large quantity of water. In such a case, a large regional variation in rheological properties may occur associated with the regional variation in water content.

4.3 Tidal Dissipation

The tidal environment of Mars allows to infer the rheological properties of the martian interior from the orbital evolution of the planet's two tiny moons, Phobos and Deimos, which are rotationally locked into a 1:1 spin-orbit resonance. The satellites' orbital evolution is closely connected to the dissipation of tidal energy within the martian interior, and a phase lag between the tidal-bulge direction and the direction to the tide-generating satellite causes exchange of angular momentum between planetary rotation and satellite orbital motion. The mean specific dissipation factor of Mars Q_p is then related to the tidal lag angle γ by $Q_p = \cot 2\gamma$.

While Deimos' almost circular orbit is close to synchronous with Mars' present rotation rate and subject to less secular deceleration, Phobos's highly eccentric orbit is well within the synchronous distance and, therefore, the satellite undergoes notable secular acceleration. The orbital evolution of Phobos is mainly affected by the degree-two semidiurnal tide, while the third-order tide is expected to contribute less than 10 % to the secular acceleration of Phobos (Zharkov and Gudkova 1997). The latter is now known with high accuracy due to long-term monitoring of Phobos' orbital longitude (see Jacobson 2010 for a review). From long-term observations of the secular accelerations of the martian satellites $\dot{n}_i/n_i$ or equivalent time rates of change of their semi-major axes, $\dot{a}_i/a_i = -2\dot{n}_i/3n_i$, the ratio k_2/Q_p of the elastic Love number k_2 and the planet's mean specific dissipation factor Q_p can be inferred according to

$$\dot{a}_i = 3m_i \frac{k_2}{Q_p} \left(\frac{\mathrm{G}}{a_i (M_p + m_i)} \right)^{1/2} \left(\frac{r_p}{a_i} \right)^5, \tag{4}$$

where G is the gravitational constant, M_p is the planet's mass, and m_i, a_i, and n_i are mass, semimajor axis, and mean motion of each satellite, respectively. As a measure for Mars' gravitational response to tides exerted by the Sun, k_2 is dependent on the planet's interior structure, rheological layering, and tidal forcing period. Together with the mean density and axial moment-of-inertia of Mars, k_2 imposes additional constraints on the size and physical state of the martian core (e.g., Sohl et al. 2005; Verhoeven et al. 2005; Rivoldini et al. 2011).

Based on the analysis of radial weighting functions for the distribution of elastic strain energy, Zharkov and Gudkova (1997) conclude that the tidal phase lag is not sensitive to the martian crust and uppermost mantle. Dissipation of tidal energy mainly occurs at greater depth in the middle or lower mantle. Furthermore, dissipation in the middle or lower mantle supports the view that the martian mantle cannot be completely dry.

This analysis is consistent with recent radar sounder observations of lithospheric deflection beneath the north polar units of Mars. These measurements indicate that the geodynamic response of the martian lid, i.e., the lithosphere and uppermost mantle to the loading history of the north polar layered deposits (NPLD) is less than previously expected (Phillips et al. 2008). Deposition of the NPLD is believed to be driven by climate variations on timescales of several 10,000 of years. This is sufficiently short that the corresponding geodynamic creep response of the martian mantle could be dominated by time-dependent or transient rheological behavior (e.g., Faul and Jackson 2005).

4.4 Elastic Lithosphere Thickness

In the absence of direct heat flow measurements (see Sect. 6.2), the evolution of the elastic lithosphere thickness T_e is one of the few clues we have to reconstruct the thermal history of the planet. The elastic thickness is a measure for the stiffness of the lithospheric plates and can be estimated by analyzing the response of the lithosphere to loading. Given a rheological model, the mechanical thickness of the lithosphere can be derived from the elastic thickness, and mechanical thickness can in turn be identified with an isotherm (McNutt 1984). In this way, elastic thickness estimates can be used to test the predictions of thermal evolution models (e.g., McGovern et al. 2002; Montési and Zuber 2003; Grott and Breuer 2008, 2010; Ruiz et al. 2011).

Most T_e estimates have been derived from gravity and topography data (McGovern et al. 2004; Kiefer 2004; Belleguic et al. 2005; Hoogenboom and Smrekar 2006; Wieczorek 2008; Grott et al. 2011), but some geological features allow for more direct approaches. Phillips et al. (2008) have modeled the lithospheric deflection due to polar cap loading, and analysis of rift flank uplift has been used by Barnett and Nimmo (2002), Grott et al. (2005), and Kronberg et al. (2007) to constrain T_e at the Tempe Terra, Coracis Fossae, and Acheron Fossae rift systems, respectively, while the position of Nili Fossae has been modeled by assuming these circumferential graben to be a tectonic feature caused by mascon loading at the Isidis basin (Comer et al. 1985; Ritzer and Hauck 2009). Furthermore, T_e has been constrained from the seismogenic layer thickness T_s, which is defined as that part of the lithosphere which deforms in a brittle fashion when exposed to tectonic stresses. T_s usually is of the same order as T_e or slightly smaller, and T_s has been determined at thrust faults by Schultz and Watters (2001), Grott et al. (2007a), and Ruiz et al. (2009), who modeled lobate scarp topography by varying depth of faulting and slip distribution on the fault surface. Other more indirect methods to estimate T_e include modeling of fault spacing using localization instabilities (Montési and Zuber 2003), and modeling of the thermal state in chaotic terrain (Schumacher and Zegers 2011).

The times corresponding to the observed paleo-flexure are usually assumed to be given by the age of the deformed surfaces, but this assumption may not always be valid. Age assignments at the Tharsis volcanoes are particularly difficult, as these have been active throughout the history of the planet (see Sect. 2.4). While the Tharsis volcanoes exhibit Amazonian surface ages, loading was likely mainly finished by the end of the Hesperian, and the observed paleo-flexure might correspond to either of these periods, resulting in age uncertainties of up to 3 Gyr. Further complications arise due to the fact that although paleo-flexure is generally assumed to be frozen-in at the time of loading, stresses in the lithosphere will decay

as a function of time due to viscous relaxation. As a result, the elastic thickness T_e will also decrease as a function of time, and the time corresponding to the observed paleo-flexure is determined by a competition between loading rate, lithospheric cooling rate, and stress relaxation rate (Albert and Phillips 2000). While stress relaxation is of limited importance for single-layer rheologies, it may become important for multi-layer configurations (Brown and Phillips 2000). Furthermore, while the strength of the Noachian lithosphere was almost exclusively carried by the crust, mantle contributions to lithospheric strength became important in the cooler Hesperian and Amazonian lithospheres. Therefore, care must be taken when interpreting mantle temperatures derived from loading models, as these may not easily be associated with a given point in time.

An overview of published elastic thickness estimates is compiled in Fig. 9, where the spatial distribution of analyzed features is given in the top panel, while T_e is given as a function of time in the bottom panel. Elastic thicknesses were small and between 0 and 20 km during the Noachian period, but quickly increased to values above 50 km during the Hesperian. Values in the Amazonian range from 40 to 150 km, and best estimates for the present day elastic thickness are above 150 km. In particular, lithospheric deflection due to loading at the north polar cap locally constrains present day T_e to values greater than 300 km at this location (Phillips et al. 2008).

This evolution is in general agreement with planetary cooling models (McGovern et al. 2004; Grott and Breuer 2008), and small elastic thicknesses during the earliest evolution are consistent with higher than present-day mantle temperatures and an associated high Noachian heat flux (McGovern et al. 2002; Grott and Breuer 2010). Thermal evolution models typically predict Noachian heat fluxes above 60 $\mathrm{mW\,m^{-2}}$, with slightly lower values around 50 $\mathrm{mW\,m^{-2}}$ during the Hesperian period. Heat flows then steadily decline to around 20 $\mathrm{mW\,m^{-2}}$ today (Morschhauser et al. 2011). However, higher heat fluxes alone are insufficient to explain the small elastic thicknesses derived for the Noachian period, and rheological layering also seems to play an important role (Grott and Breuer 2008, 2009). Decoupling of the crust and mantle lithosphere as indicated by reduced strength at the base of the crust in Fig. 7(c) can significantly reduce the overall lithospheric thickness, and the disappearance of this layer due to planetary cooling then results in a sudden increase of T_e (Burov and Diament 1995; Grott and Breuer 2008).

In order for an incompetent layer to exist, a weak crustal rheology is required (Grott and Breuer 2008, 2010), and given the absence of large-scale felsic deposits, it seems likely that water is responsible for rheological weakening (see Sect. 4.2). Furthermore, small T_e require relatively thin thermal boundary layers in the upper mantle, indicating that mantle convection was active and vigorous during this time period. Therefore, any stable mantle stratification following magma ocean solidification and mantle overturn (Elkins-Tanton et al. 2003) could not have survived longer than 300–500 Myr. Thin thermal boundary layers also require small mantle viscosities, indicating that the convecting mantle is best described by a wet or only partially dehydrated rheology with viscosity around 10^{19} Pa s at 1600 K.

An open question concerns the large elastic thickness values derived from polar cap loading, which require lithospheric temperatures to be colder than expected. This could either imply a sub-chondritic bulk composition in terms of heat producing elements (Phillips et al. 2008), or a large degree of spatial heterogeneity of the mantle heat flow (Phillips et al. 2008; Grott and Breuer 2009, 2010; Kiefer and Li 2009), which—potentially lacking upwellings in the polar regions—could be below the average there. These hypotheses are difficult to test by models, but in-situ heat flow measurements could help to discriminate between the two (see Sect. 6.2).

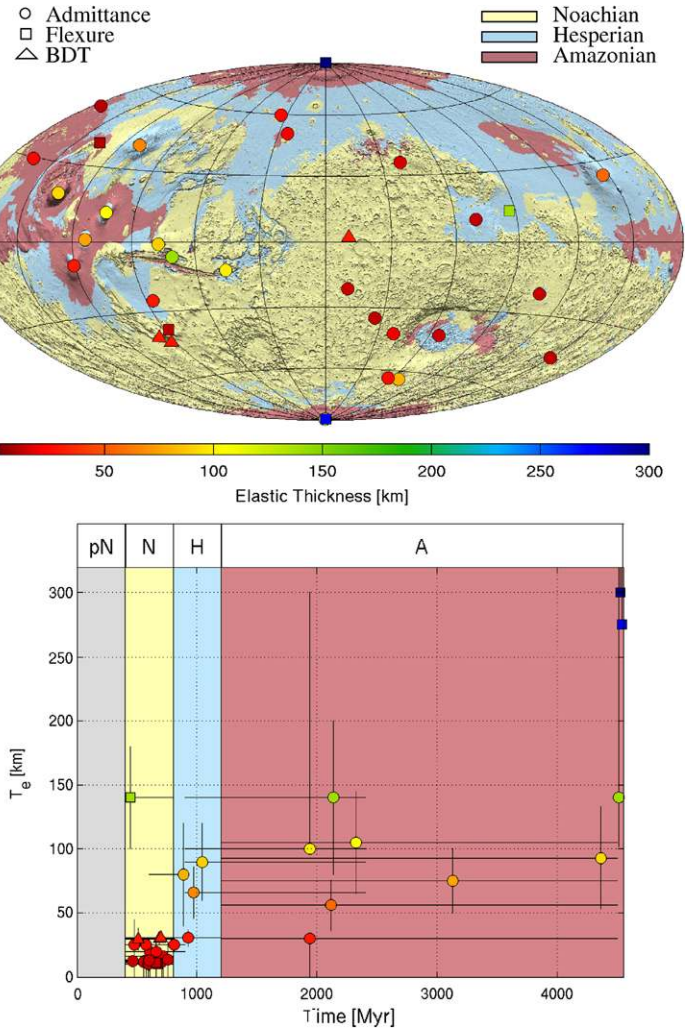

Fig. 9 *Top*: Compilation of published elastic thickness estimates overlaid over a MOLA shaded relief topographic map. The major martian geological epochs derived from the maps of Scott et al. (1986, 1987a, 1987b) are indicated by color. Elastic thicknesses are given in color code, and the methods used to estimate T_e are indicated by symbols (see text for details). *Bottom*: Same dataset as above, but shown as a function of surface age for the corresponding geological units. Errorbars for the individual data points are indicated. Times of loading were assigned based on the surface ages of the corresponding features

5 Thermo-Chemical Evolution

5.1 Partial Melting

Partial melting is one of the most important processes for the chemical evolution of terrestrial planets, controlling the redistribution of various elements among molten materials and residual solids, chemical differentiation occurring via melt transport and element diffusion. The composition of melts and residual solids has been thoroughly studied under shallow

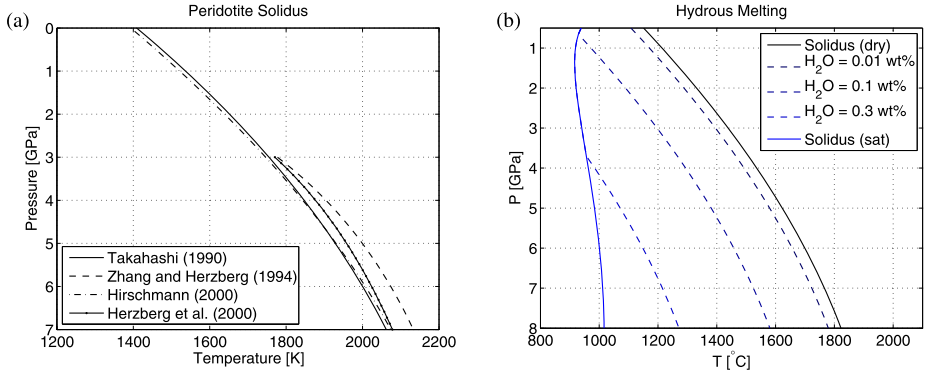

Fig. 10 (**a**) Different parameterizations of the peridotite solidus as a function of pressure. Note that the parameterizations by Zhang and Herzberg (1994) and Herzberg et al. (2000) are only valid above pressures of 3 GPa. (**b**) Influence of water content on the solidus of peridotite as a function of pressure. Cf. Fig. 3 in Katz et al. (2003)

mantle conditions (e.g., Kushiro 2001), and an extensive literature on the melting behaviour of terrestrial KLB-1 peridotite exists (e.g., Hirschmann 2000 and references therein). Apart from the parameterization by McKenzie and Bickle (1988), current solidus parameterizations (Takahashi 1990; Zhang and Herzberg 1994; Herzberg et al. 2000; Hirschmann 2000; Katz et al. 2003) agree to within 50 K, a difference attributed to varying experimental techniques and differences in sample compositions (Hirschmann 2000). Fits to the experimentally derived terrestrial solidi are shown in Fig. 10(a), where curves by Herzberg et al. (2000) and Zhang and Herzberg (1994) are only valid at pressures greater than 3 GPa.

Water can have a significant influence on the solidus of mantle materials (Hirth and Kohlstedt 1996; Asimow and Langmuir 2003; Katz et al. 2003; Hirschmann 2006), and a bulk water content of 250 ppm (0.025 wt%) can lower the peridotite solidus by 100 K. The effect of water on the solidus of the terrestrial mantle is summarized in Fig. 10(b), where the pressure dependent water saturation curve is indicated to the left of the diagram. As discussed above, the bulk water content of the martian mantle is still a matter of debate, and while dry scenarios would not result in a significant reduction of the mantle solidus, the presence of petrologically significant amounts of water of a few hundred ppm cannot be ruled out.

In the absence of a broad experimental database for melting of martian mantle materials, the KLB-1 peridotite solidus derived for the Earth's mantle is usually also applied to Mars. However, it should be pointed out that alkali content and, to a lesser extent Mg# too, influence the mantle solidus (Herzberg et al. 2000; Hirschmann 2000). The solidus decreases by about 100 K when increasing the total $Na_2O + K_2O$ content from 0.2 to 0.75 wt%, while the solidus is increased by a similar amount when increasing Mg# from 85 to 91. Therefore, a firmer experimental basis to parametrize mantle melting on Mars is clearly desirable.

The composition of melts produced under deep mantle conditions ($P > 14$ GPa) is less well constrained than shallow melting (Bertka and Holloway 1994a, 1994b) and melt compositions can be distinctly different in the deep mantle (e.g., Litasov and Ohtani 2002). High pressure melts tend to be Fe-rich and silica-poor, and hence heavier than the surrounding minerals. In such a case, melts may sink to the core-mantle boundary rather than ascend to the surface. These melts are dense and water-rich and can play an important role as a water reservoir in the deep interior.

During partial melting, incompatible elements like water (hydrogen), or the heat producing elements K, Th, and U will preferentially partition into the liquid, thus being extracted from the mantle along with the melt. The degree to which hydrogen and other elements are removed from the minerals and rocks by partial melting depends on the process of melting, and two modes of melt-solid separation are often considered: (1) Fractional melting is the melting process in which chemical equilibrium between the melt and the mineral is attained only at the interfaces between the two. The majority of the melt is assumed to be removed quickly from the source, such that a majority of the melt does not reach equilibrium with the residual solids. This mode of melting occurs when the time scale of melt extraction is faster than the time scale of element diffusion. (2) If all the melt produced by partial melting is in equilibrium with the solids, a batch melting model is appropriate to describe the melting process. In this case, the time scale of melt extraction is slower than the element's diffusion time scale, such that chemical equilibrium is reached for the entire melt volume.

The mode of melt-solid separation can be evaluated using the non-dimensional number ξ (e.g., Iwamori 1992, 1993)

$$\xi = 2\sqrt{\frac{DL}{d^2 v}} \tag{5}$$

where D is the diffusion coefficient of a relevant atomic species, L is the characteristic length scale of the melting region, d is the grain-size, and v is the velocity of mantle convection. The diffusion coefficients D differ significantly among different species, and D is close to 10^{-10} m^2/s for hydrogen (Kohlstedt and Mackwell 1998), while it is about 10^{-20} m^2/s for Th and U (Van Orman et al. 1998). Choosing $L \sim 100$ km, $d \sim 1$ cm, $v \sim 1$ cm/yr, we find that for hydrogen equilibrium melting (batch melting) is likely, whereas Th and U are better described by disequilibrium (fractional) melting. In numerical models of the martian thermo-chemical evolution, both melting models have been applied irrespective of the different diffusion coefficients (Hauck and Phillips 2002; Fraeman and Korenaga 2010; Morschhauser et al. 2011). While this has only a minor influence on the bulk extraction of K, Th, and U, the reduced concentration of residual hydrogen and the associated dehydration stiffening of the mantle rheology may play an important role in spatially resolved convection models. However, experimental data on fractional melting is sparse, because melting phase relationships change continuously as melt is extracted. Therefore, fractional melting experiments are usually limited to a few discrete jumps in composition. It is also worth noting that melt extracted at depth by fractional melting might equilibrate with its surroundings at shallower depth, resulting in an overall process that is closer to batch melting.

5.2 Parameterized Thermo-Chemical Evolution Models

The thermal evolution of Mars is intimately related to the history of martian volcanism and some insight into the evolution of the crust-mantle system may be gained from parameterized convection models. These models calculate the thermo-chemical evolution starting from an initial state after core formation and solve the energy balance equations for core, mantle, and lithosphere as a function of time (see Fig. 11) (Spohn 1991; Hauck and Phillips 2002; Breuer and Spohn 2006; Parmentier and Zuber 2007). Mantle differentiation is treated by comparing mantle temperatures to the peridotite solidus and the degree of partial melting is calculated by a linear interpolation between solidus and liquidus (Hauck and Phillips 2002; Schumacher and Breuer 2006; Morschhauser et al. 2011). Although the degree of partial melting is a non-linear function of temperature, the linear approximation is in satisfactory agreement with the experimental data for melt fractions below

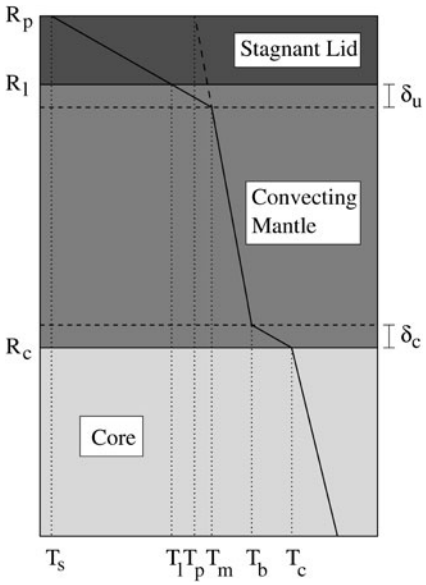

Fig. 11 Schematic diagram showing the reservoirs considered in parameterized thermal evolution models, which comprise the stagnant lid, the convecting mantle including the thermal boundary layers, and the core. The planetary radius R_p, stagnant lid radius R_l, and core radius R_c are indicated. δ_u and δ_c are the upper and CMB boundary layer thickness, respectively. Temperatures shown are the surface temperature T_s, the stagnant lid temperature T_l, the potential mantle temperature T_p, the upper mantle temperature T_m, the lower mantle temperature T_b, and the core temperature T_c. Together, these quantities define the thermal state of the planet

30 % (McKenzie and Bickle 1988; de Smet et al. 1999). In this way the degree of partial melting as well as the amount of partial melt extracted from the mantle can be calculated.

Thermo-chemical evolution models parametrize planetary heat loss in terms of the mantle Rayleigh number and while earliest models used scaling laws derived from boundary layer theory (Stevenson et al. 1983; Schubert and Spohn 1990; Spohn 1991), it was later recognized that the temperature dependence of the mantle viscosity can result in the development of a stagnant lid (Solomatov and Moresi 1997; Grasset and Parmentier 1998; Reese et al. 1998). Current parameterizations either treat the stagnant lid separately and consider the mantle to convect like an isoviscous fluid (Grasset and Parmentier 1998), or they parametrize surface heat flow in terms of the whole mantle Rayleigh number including the lid (Solomatov and Moresi 1997; Reese et al. 1998). While the former approach enables the modeling of feedback-mechanisms between lithosphere and mantle dynamics, the latter approach has been extended to treat non-Newtonian rheologies. In addition, latest models also try to parametrize the influence of mantle melting on the efficiency of mantle energy transport (Korenaga 2009; Fraeman and Korenaga 2010).

It has been noted early on that the single most important parameter in these calculations is the mantle viscosity (Schubert et al. 1979), but few a priori constraints exist from mineral physics. Major uncertainties are related to the unknown water content of the martian mantle (see Sects. 3.3.5 and 4.2), and plausible mantle viscosities span at least two orders of magnitude. As a consequence, a large parameter space needs to be studied. A second poorly constrained parameter is the initial temperature profile, but a feedback mechanism between temperature and mantle viscosity reduces the range of admissible present day thermal scenarios: While high temperatures result in low mantle viscosities and fast cooling, low temperatures result in high viscosities and heat accumulation. Consequently, mantle temperatures will tend to similar present day values and heat transport today will be equally efficient almost irrespective of the initial temperature profile. On the other hand, reconstructing the thermal history of the planet from present day measurements is very challenging for the same reasons. Also note that different mantle temperatures during the early evolution have important implications for mantle melting and crustal production.

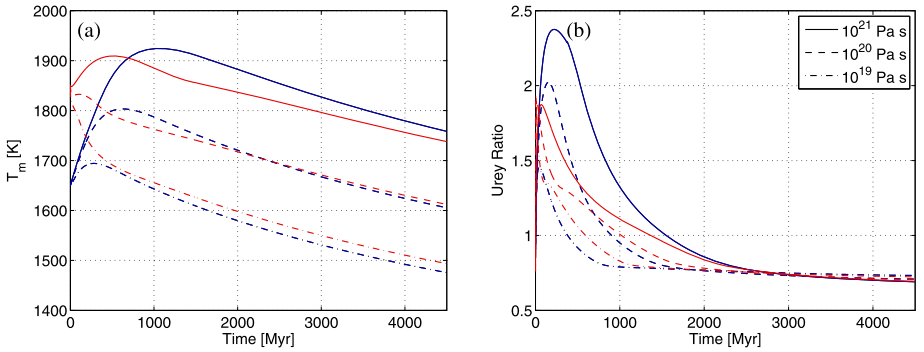

Fig. 12 (**a**) Upper mantle temperature as a function of time for parameterized thermo-chemical evolution models using three different mantle reference viscosities and two different initial upper mantle temperatures. Cold models (*blue curves*) correspond to an initial upper mantle temperature of 1650 K, while hot models (*red curves*) correspond to initial mantle temperatures of 1850 K. (**b**) Urey ratio, i.e., the ratio between the radiogenically generated heat flow and the surface heat flow for the same models

In addition to viscosity and initial temperature, energy transport is influenced by the mode of mantle convection. While Mars is currently in the stagnant lid mode of mantle convection (Solomatov and Moresi 1997; Grasset and Parmentier 1998; Reese et al. 1998), plate tectonics might have been operating during its earliest evolution. The thin crust of the northern lowlands has been taken as an indication for seafloor spreading (Sleep 1994), and the growth of the southern highlands could have then inhibited subduction, resulting in a transition to the stagnant lid mode of mantle convection (Lenardic et al. 2004). Parallel faults offsetting magnetic field contours in a way similar to transform faults on Earth have been taken as support for the plate tectonics hypothesis (Connerney et al. 2000, 2005), and planetary cooling driven by plate tectonics could have powered a core dynamo (Nimmo and Stevenson 2000; Breuer and Spohn 2003). In addition, folds and thrusts in the Thaumasia Plateau, Daedalia Planum, and Aonia Terra have been interpreted as orogenic belts (Anguita et al. 2006), a possible remnant of convergent plate margins, and the lineations in Terra Cimmeria have also been hypothesized to have been formed by convergent plates through collision and accretion of terranes (Fairén et al. 2002).

On the other hand, thermal evolution models have shown that the transition from the plate tectonics to the stagnant lid mode of mantle convection would have resulted in considerable heating and melting of the mantle (Breuer and Spohn 2003), leading to a late peak in crustal production. As a result, a substantial part of the martian crust would have been produced around 2 Gyr, contrary to observations (Norman 1999; Halliday et al. 2001; Nyquist et al. 2001; Phillips et al. 2001, see also Sect. 2.4). This, together with the persistent absence of evidence for subduction zones, argues against the plate tectonics hypothesis.

The unresolved issue of the existence or absence of plate tectonics on early Mars notwithstanding, the thermo-chemical evolution of Mars is generally modeled assuming that Mars has been in the stagnant lid mode of mantle convection ever since the onset of mantle convection (Spohn 1991; Hauck and Phillips 2002; Breuer and Spohn 2006; Parmentier and Zuber 2007; Fraeman and Korenaga 2010; Morschhauser et al. 2011). Typical cooling models are shown in Fig. 12(a), where reference viscosities spanning the range from wet (10^{19} Pa s) to dry (10^{21} Pa s) olivine have been considered. As pointed out above, the exponential dependence of mantle viscosity on temperature acts as a thermostat, and temperature profiles are similar irrespective of the initial temperature. Models predict

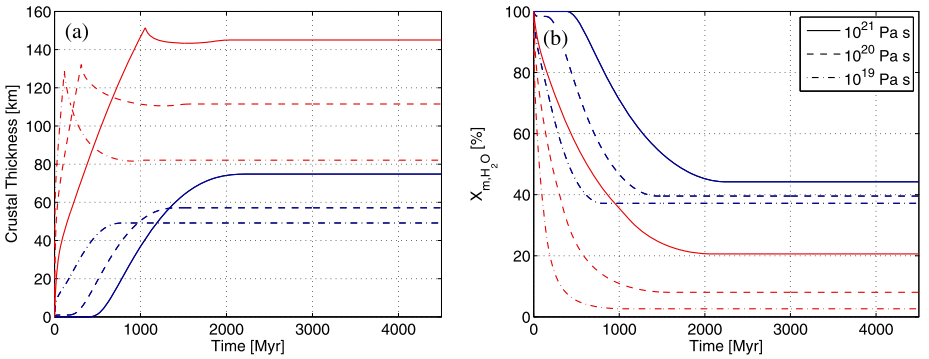

Fig. 13 (**a**) Crustal thickness as a function of time for the same models as in Fig. 12. Models showing crustal erosion are usually considered to be incompatible with observations (see text). (**b**) The bulk mantle water content as a percentage of the initial water content

present day mantle cooling rates of 40 to 50 K Gyr^{-1}, irrespective of mantle viscosity. These values are in general agreement with geochemical observations from which cooling rates of 30–40 K Gyr^{-1} have been derived (Baratoux et al. 2011a).

The rate of mantle cooling can also be described by the Urey ratio, which is given by the proportion of the radioactively produced energy output to the total energy loss of the planet. Thermal insulation by the stagnant lid makes heat loss inefficient and results in Urey ratios above unity during the early evolution, but Urey ratios tend towards their present day value close to 0.7 after the self-adjustment of mantle temperature and viscosity (Fig. 12(b)). This value is typical for stagnant lid planets, but much larger than the Urey ratio of the Earth, which is estimated to be 0.3–0.5 (Korenaga 2008; Nakagawa and Tackley 2012).

The chemical evolution of the mantle is characterized by the removal of crustal components and the extraction of incompatible elements during partial melting. Thermochemical evolution models with high initial temperatures possess voluminous melt zones, and crustal thicknesses quickly reach values in excess of 120 km (Fig. 13(a)). Due to the crustal enrichment of heat producing elements and the relatively low thermal conductivity of the crustal layer, these models accumulate heat in the stagnant lid, which can result in an erosion of the lid from below. In this way, crustal material can be delaminated and recycled back into the mantle (Morschhauser et al. 2011). However, isotopic anomalies in the martian meteorites (Chen and Wasserburg 1986; Harper et al. 1995; Borg et al. 1997; Brandon et al. 2000; Halliday et al. 2001) indicate an early mantle differentiation event and the formation of distinct geochemical reservoirs about 4.5 Ga ago, and insignificant reservoir mixing thereafter (Mezger et al. 2012, this issue). Therefore, crustal recycling is generally believed to be incompatible with this observation, and models showing crustal recycling are usually not considered (Morschhauser et al. 2011; Grott et al. 2011).

Crustal recycling is absent in models with low initial temperatures, and extracted crustal volumes are generally smaller. Models typically predict crustal thicknesses between 40 and 80 km (Hauck and Phillips 2002; Breuer and Spohn 2006; Morschhauser et al. 2011; Grott et al. 2011), and small crustal thicknesses are compatible with estimates derived from gravity and topography data, which predict the crust to be 57 ± 24 km thick on average (Wieczorek and Zuber 2004). The timing of crustal production is mainly a function of the reference viscosity. For large viscosities, convection is relatively sluggish and melt zones are pushed to greater depth, such that the mantle needs to heat up before partial melt can be produced.

On the other hand, low mantle viscosities allow for the production of partial melt during the early evolution. As most of the martian crust probably formed before 4 Gyr (Nimmo and Tanaka 2005), wet rheologies resulting from bulk mantle water contents of at least a few tens of ppm H_2O are generally preferred (Hauck and Phillips 2002; Breuer and Spohn 2006; Fraeman and Korenaga 2010; Morschhauser et al. 2011; Grott et al. 2011).

Apart from the bulk crustal thickness, parameterized models can give a first order estimate of the depth and degree of partial melting, the latter of which has a large influence on the efficiency of incompatible element removal. For small melt fractions, heat producing elements and water are efficiently removed from the deep interior, and melt fractions predicted by parameterized models are between 10 and 20 % during the early evolution, but drop below 10 % between 1 and 1.5 Gyr after accretion (cf. Figs. 12 and 13). Thereafter, large scale crustal production ceases, and present day melting is not predicted by parameterized models as melting is inhibited by the thick stagnant lid. Present day magmatism would be driven by a locally thickened crust (Schumacher and Breuer 2007), or the penetration of mantle plumes into the stagnant lid (Li and Kiefer 2007; Grott and Breuer 2009), but these processes are not considered in parameterized models. Ruling out models which show crustal recycling, about 50 % of the total inventory of incompatible elements is typically extracted from the interior (Fig. 13(b)). Successive depletion of the mantle is consistent with surface thorium abundances of the Hesperian and Amazonian volcanic provinces, which indicate that Hesperian volcanism was fed from a non-depleted mantle source, while Amazonian volcanics point towards a depleted mantle source during this time period (Baratoux et al. 2011a).

The link between planetary cooling models and the depth of partial melting is not straight-forward to make, as stagnant lid planets primarily cool by growth of the stagnant lid, while at the same time keeping the interior relatively warm. Depending on the initial temperature profile and mantle viscosity, stagnant lid planets can experience phases of mantle heating during the early evolution, and stagnant lid thickness need not increase monotonously (Breuer and Spohn 2003, 2006; Schumacher and Breuer 2006; Morschhauser et al. 2011). Therefore, there is no one-to-one correspondence between depth of melting and crystallization age. However, the situation is less complex during the later evolution following the Hesperian, when planetary cooling and growth of the stagnant lid push the zone of melting to ever increasing depths.

Taken together, results of thermo-chemical evolution calculations indicate that a wet mantle rheology is consistent with the martian crustal and elastic thickness evolution, where it should be noted that as little as a few tens of ppm water are rheologically significant. Hydrous melting becomes important if the mantle water content exceeds a few hundred ppm and is currently not considered in most models. Evolution models with low initial upper mantle temperatures are generally preferred, as these do not give rise to crustal erosion. The produced crustal volumes are in general agreement with estimates from gravity and topography studies (Wieczorek and Zuber 2004). Initial upper mantle temperatures on Mars were probably close to 1700 K, and secular cooling of 40–50 $\mathrm{K\,Gy^{-1}}$ resulted in average present day upper mantle temperatures of 1500 K, inhibiting global magmatic activity, that is furthermore hindered by the presence of a stagnant lid. However, localized activity may still be feasible in regions of a locally thickened crust or in the heads of uprising mantle plumes. Furthermore, approximately 50 % of the incompatible elements were likely removed from the mantle in the course of its entire evolution.

5.3 The Crustal Dichotomy

The surface of Mars shows specific features such as the prominent crustal dichotomy, whose formation cannot be addressed using one-dimensional models. The southern highlands and northern lowlands of Mars differ markedly in average elevation (Smith et al. 1999) and crustal thickness (Zuber et al. 2000; Neumann et al. 2004), the crust being about 25 km thicker in the highlands than in the lowlands. It is generally accepted that this crustal dichotomy is one of the oldest features on Mars, but the exact timing of the dichotomy formation is still debated. Estimates vary between the first 50 Ma after solar system formation (Solomon et al. 2005) and the Early Noachian period (>3.9 Ga) (Frey et al. 2002; Nimmo and Tanaka 2005). Possible explanations of the origin of the dichotomy invoke either exogenic (Wilhelms and Squyres 1984; Frey and Schultz 1988) or endogenic processes (Wise et al. 1979), but none of the proposed formation mechanisms appears to be fully convincing, which is in part due to the uncertainty in the timing of the dichotomy formation.

Proposed exogenic processes include formation by one (Wilhelms and Squyres 1984) or several (Frey and Schultz 1988) large impacts, and this idea has recently been revived in a series of articles explaining the observed elliptical shape of the lowlands (Andrews-Hanna et al. 2008; Nimmo et al. 2008; Marinova et al. 2008). However, an endogenic origin of the dichotomy cannot be ruled out.

In this respect, different mechanisms associated with (1) an early phase of plate tectonics (Sleep 1994); (2) an episode of degree-one (one-ridge) mantle convection (Schubert and Lingenfelter 1973; Wise et al. 1979; Zhong and Zuber 2001; Keller and Tackley 2009); (3) the evolution of an early magma ocean (Hess and Parmentier 2001; Elkins-Tanton et al. 2003); and (4) a thermal anomaly following a giant impact in the southern hemisphere (Reese et al. 2010; Golabek et al. 2011) have been proposed. As the plate tectonics hypothesis has been discussed in the previous chapter, we will focus the discussion here on points 2–4.

Low-degree mantle convection could be responsible for the formation of the dichotomy if a single large upwelling plume were present underneath the southern hemisphere. Such a flow structure can be obtained for particular mantle viscosity profiles, and an episode of long-wavelength mantle convection has been suggested to be the consequence of a layered mantle viscosity including a viscosity jump of more than a factor of 25 in the mid-mantle and a relatively low viscosity in the upper mantle (Zhong and Zuber 2001; Roberts and Zhong 2006). Alternatively, a mid-mantle viscosity jump linked to the martian mineralogical transition zone below 1000 km depth also promotes large scale (low-degree) flow (Keller and Tackley 2009). The time required to develop degree-one or low-ridge convection ranges from 100 Ma to several hundred Ma and is consistent with most assumptions about the timing of the dichotomy formation. However, these models result in continuous magmatic resurfacing of the southern hemisphere, thereby destroying the initially dichotomous crustal structure in the long-term.

Furthermore, such models implicitly assume the martian mantle to be homogeneous, but the existence of distinct geochemical reservoirs is suggested by isotopic anomalies in the martian meteorites (Chen and Wasserburg 1986; Harper et al. 1995; Borg et al. 1997; Brandon et al. 2000; Halliday et al. 2001). These data indicate an early mantle differentiation event about 4.5 Ga ago, and insignificant reservoir mixing thereafter. It seems unlikely that long-wavelength flow could maintain the separation of reservoirs to the present day, and dynamic models still need to be improved to be consistent with all observations.

One possible mechanism to form distinct and separate geochemical reservoirs is magma ocean solidification by fractional crystallization, which likely results in an unstable density stratification in the martian mantle. Late-stage silicates that crystallize at shallow depths are

denser than earlier cumulates that crystallize near the base of the magma ocean (Hess and Parmentier 2001; Elkins-Tanton et al. 2003, 2005), and a potential long-wavelength overturn of this unstable situation may account for the crustal dichotomy (Hess and Parmentier 2001).

Although such a process would form distinct geochemical reservoirs, models of the interior evolution after mantle overturn indicate that different reservoirs remain dynamically strictly separated, because the density differences between different layers are large. This contradicts the small elastic lithosphere thicknesses derived for the Noachian period (Sect. 4.4), which require the lithosphere to be warm and the upper thermal boundary layer to be thin. Furthermore, a potential reservoir in the deep mantle would have no surface expression and thereby would remain'invisible', contrary to observations. Therefore, alternative explanations for the early formation of reservoirs that did not mix significantly during the subsequent evolution are needed. One such model includes the rapid formation of a harzburgite layer (Schott et al. 2001; Ogawa and Yanagisawa 2011) by early crustal formation, which would be less dense than the primordial mantle, and would remain stable as a consequence of dehydration and subsequent stiffening.

5.4 The Tharsis and Elysium Volcanic Provinces

Other surface features which cannot be understood using one dimensional models are the two large volcanic provinces of Tharsis and Elysium, which show longstanding and stable volcanic activity. Their presence argues for only a limited number of mantle plumes and the operation of low degree mantle convection. While activity in Tharsis and Elysium took place throughout martian history, these provinces likely acquired their present shape relatively early (e.g., Phillips et al. 2001; Solomon et al. 2005; Nimmo and Tanaka 2005), and as both Tharsis and Elysium are located near or at the dichotomy boundary, a dynamic link between these two features has been suggested (Wenzel et al. 2004; Zhong 2009; Šrámek and Zhong 2010, 2012). Taking the presence of a hemispheric lithospheric keel representing a depleted mantle reservoir into account, Šrámek and Zhong (2012) demonstrated that a stiff keel can induce a rotation of the entire lithosphere relative to the underlying mantle, until the upwelling is stabilized near the edge of the keel. This edge corresponds to the dichotomy boundary, thus accounting for the location of the Tharsis rise.

In addition to the aforementioned viscosity structure, low-degree mantle convection may also be caused by mantle phase changes like the olivine to spinel and spinel to perovskite transitions (e.g., Weinstein 1995; Harder and Christensen 1996; Breuer et al. 1998; Harder 2000; Buske 2006). In particular, the endothermic spinel to perovskite phase transition that might be located close to the core-mantle boundary (Sohl and Spohn 1997) would stabilize upwelling plumes and reduces their number to one or two. Although the long timescale necessary to form a single upwelling in most models is inconsistent with an early formation of either the dichotomy or the volcanic provinces (Roberts and Zhong 2006), more recent three dimensional convection models with strongly temperature dependent rheology suggest a shorter formation time scale, consistent with the observations (Buske 2006). Other models capable of generating longstanding plumes consider chemical layering (Schott et al. 2001; Wenzel et al. 2004), but these models do not predict volcanic provinces to be at the dichotomy boundary. Rather, volcanic activity is predicted to be focused in the center of regions with a thickened crust, contrary to observations.

6 Future Investigations

The combined analysis of data from orbiting and landed spacecraft, laboratory investigations of the martian meteorites, and theoretical modeling, have revealed a complex evolu-

tion of the crust-mantle system and much has been learned about the geological history of the planet. With the presently ongoing debates concerning the age of the shergottites and the water content of the martian mantle, a considerable range of scenarios for the magmatic history of Mars seems plausible, and the link between thermal models and petrological investigations remains non-unique. To make significant progress in quantifying the martian geochemical reservoirs, a new suite of space missions focusing on the geophysical exploration of Mars is needed. Furthermore, the return of carefully selected samples would be extremely valuable. In the following, we outline what observations are needed and what may be expected from future exploration and modeling efforts.

6.1 Mars Science Laboratory

The Mars Science Laboratory (MSL) called Curiosity has landed at the Hesperian aged Gale Crater, in which sediments showing evidence of sulfates and phyllosilicates can be accessed by the rover (Grotzinger 2011). Although the mission is dedicated to the search for possible traces of biological activity and the characterization of the surface environment, new in-situ observations of ancient igneous materials are possible. For example, the rover began the mission by traversing an alluvial fan and is at the time of writing providing new observations of igneous rocks. The payload, which includes an APXS instrument similar to that of the MERs, a remote laser-induced breakdown spectrometer (ChemCam) for chemical analyses, and an X-ray diffractometer (CheMin) for mineralogical analyses, is well suited to providing new information to address magmatic processes from these new samples.

6.2 Heat Flow

The average heat flow from a planet reflects the bulk abundance of heat producing elements in the planetary interior. In the absence of direct measurements, martian heat flow has been estimated from the deformation of the lithosphere as discussed above (e.g., Schultz and Watters 2001; McGovern et al. 2004; Grott et al. 2005; Ruiz et al. 2009 amongst others), yet large uncertainties are associated with this method. Heat flow estimates are then related to the time of deformation, which is again poorly known and may not be represented by the crater retention age of the corresponding surfaces (Beuthe et al. 2012).

In order to constrain the bulk abundance of heat producing elements in the martian interior, a suite of direct heat flow measurements is needed (Grott et al. 2007a; Dehant et al. 2012a). While a large number of measurements was needed to constrain the heat flow of the Earth (e.g., Pollack et al. 1993) the situation on Mars is probably less complex, and average surface heat flow can likely be constrained from measurements at only a few well chosen sites. Being a one-plate planet, heat flow variations on Mars are expected to be smaller than those on the Earth, although some geographical variation depending on factors like local concentration of radioactive elements and crustal thickness can be expected (Grott and Breuer 2010, see also Fig. 14). As such, heat flow around Terra Sirenum is expected to be elevated due to a local enrichment of heat producing elements in the crust, whereas heat flow in large impact basins is probably lower due to small crustal thicknesses. In order to quantify the average heat flow, measurements in three to four geologically representative regions (e.g., the northern lowlands, southern highlands, Tharsis, and Hellas) are needed, and given the average heat flow it is then straightforward to estimate the average heat production rate in the martian interior. This is due to the fact that the present day Urey ratio is almost independent of the planet's cooling history and close to 0.7 (see Sect. 5.2), and the bulk abundance of radioactive elements in the planetary interior can thus be linked to the surface heat flow.

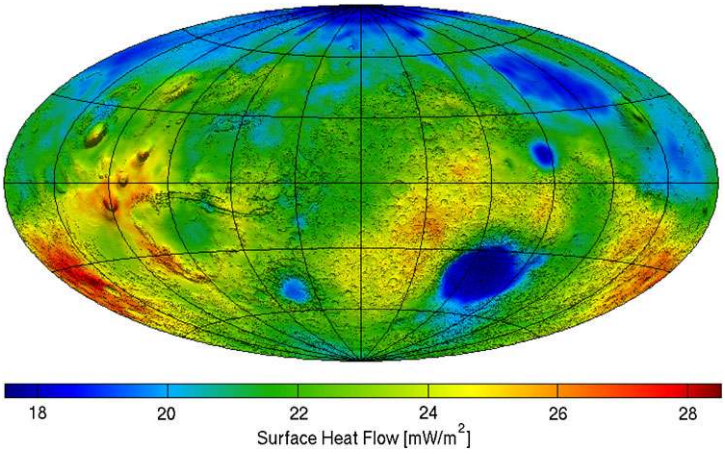

Fig. 14 Expected present day surface heat flow on Mars assuming bulk radioactive heat source abundances corresponding to the compositional model of Wänke and Dreibus (1994), crustal heat source abundances derived from gamma ray spectroscopy (Taylor et al. 2006), and crustal thicknesses derived from gravity and topography data (Neumann et al. 2004). Surface abundances of heat producing elements have been assumed to be representative for the entire crustal column (Taylor et al. 2006), and mantle heat flow has been calculated from a thermal evolution model resulting in a Urey ratio of 0.7 (Grott and Breuer 2010)

A comparison of heat flow in regions with locally thin and thick crust would furthermore indicate the crustal enrichment of heat producing elements with respect to the mantle. It is currently assumed that the crustal thickness inside the Hellas basin is extremely small and probably close to 5 km (Zuber et al. 2000; Neumann et al. 2004), such that heat flow inside the basin should primarily reflect its mantle value. By comparing heat flow values obtained inside the basin to others obtained in, for example, a representative highland area, much could be learned about processes like mantle melting and differentiation.

Other considerations which need to be taken into account include the possibility of active mantle plumes beneath the Tharsis and Elysium volcanic provinces. Crater counts suggest that some areas of Tharsis may have been volcanically active within the last tens of millions of years (Neukum et al. 2004; Hauber et al. 2011), and if plumes indeed exist underneath these regions, local heat flow would be expected to be elevated by a factor of two (Kiefer and Li 2009; Grott and Breuer 2010). Thus, a plume signature would be clearly visible in the data and heat flow measurements could help constrain the state of mantle convection, adding to the discussion of large scale mixing in the martian interior. The recently selected Discovery-class mission InSight (Banerdt et al. 2012) scheduled to launch in 2016 will carry a heat flow probe (Spohn et al. 2012) to the martian surface. In this way, an important baseline measurement will be conducted to constrain the heat flow from the martian interior.

6.3 Electrical Conductivity

A measurement of the electrical conductivity of the martian mantle would be a valuable indicator of the physical and chemical conditions in the planetary interior, in particular in light of the possible sensitivity to the presence of water (hydrogen) in the mantle (see, e.g., Poe et al. 2010; Karato and Wang 2011). To a lesser extent, electrical conductivity is also sensitive to other parameters such as temperature and iron content (Mg#) but these parameters can be estimated independently with a certain amount of confidence. As the distribution

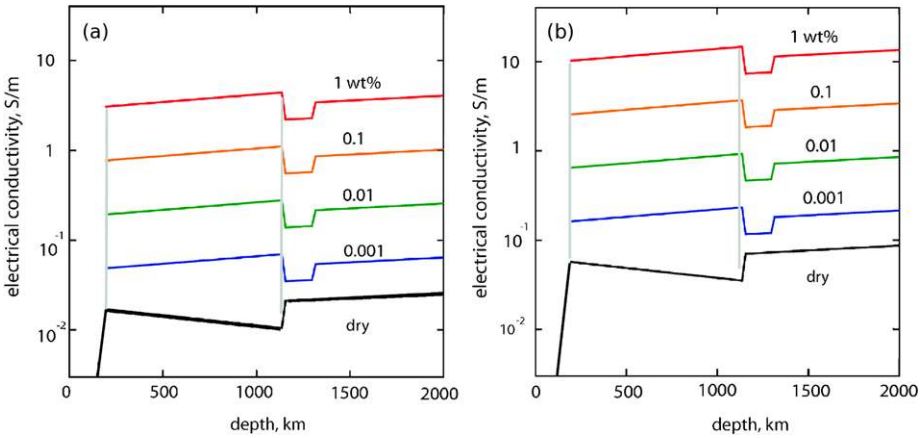

Fig. 15 (**a**) Electrical conductivity as a function of depth for different mantle water contents. The mantle transition zone representing phase changes in olivine is indicated by a kink in the profiles. An upper mantle temperature of 1700 K has been assumed. (**b**) Same as (**a**), but for an upper mantle temperature of 2000 K

of water reflects the history of the chemical evolution of Mars, knowledge of the electrical conductivity has the potential to place constraints on chemical evolution models. Electrical conductivity in the deep interior can be inferred from electromagnetic induction experiments (e.g., Grimm 2002), that can be conducted using a surface magnetometer, as has been done for the Moon (e.g., Sonett et al. 1971).

Electrical conductivity in minerals and rocks is determined by transfer of charged species, and in most minerals the dominant charge carriers are ferric iron- and/or hydrogen-related point defects (Karato and Wang 2011). Extensive laboratory studies have been carried out to determine the dependence of electrical conductivity on temperature, pressure, major element chemistry, water content and oxygen fugacity, and nearly complete data sets are now available for the electrical conductivity of most dominant minerals in the crust and mantle of Mars (olivine, orthopyroxene, clinopyroxene, garnet, wadsleyite and ringwoodite).

Using laboratory data on the influence of temperature, pressure, and water content on the electrical conductivity of mantle minerals (Romano et al. 2006, 2009; Xu et al. 1998, 2000), models of the conductivity-depth profile can be constructed if the temperature-depth profile is known. Figure 15 shows some synthetic profiles as a function of water content using the data compiled in Karato and Wang (2011). A small effect of higher Fe content has been taken into account. A comparison of Figs. 15(a) and (b) demonstrates that the uncertainties introduced by the imperfect knowledge of the mantle temperature are modest. In Fig. 15, water content was assumed to be constant as a function of depth, but layering could in principle be taken into account.

The way in which electrical conductivity depends on mantle water content is the subject of ongoing debate (Yoshino et al. 2006, 2009; Poe et al. 2010; Karato and Wang 2011; Yang 2012), but it is generally accepted that water plays an important role for the mantle conductivity structure. Note, however, that alternative models include the effects of carbonatite melts (Gaillard et al. 2008), which also show high electrical conductivities, indicating that the relationship between conductivity and water content may not be straightforward. Depending on the exact sensitivity to water content compared to other parameters, a measurement of the electrical conductivity in the mantle could yield valuable constraints on the

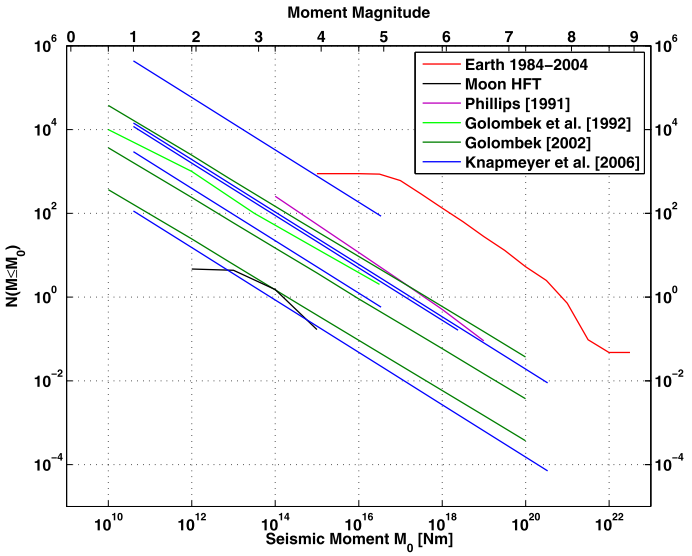

Fig. 16 Number of events per year that exceed a given seismic moment, according to different estimates (see *legend*). Data for the Earth is from the Harvard CMT project (Dziewonski et al. 1983 and annual follow-ups), which provides a source mechanism catalog complete for magnitudes larger than about 5. Data for the Moon (Oberst 1992) is for shallow moonquakes only, the contribution of the deep moonquakes is negligible

water content in the martian interior. In this way, one could start to quantify this fundamental geochemical reservoir, which is otherwise only indirectly constrained.

6.4 Seismology

Seismological experiments have been conducted on Mars using the seismometers onboard the two Viking landers (Anderson et al. 1977), but the experiment did not return a unique detection of any seismic event. This non-detection only supported the conclusion that Mars is likely seismically less active than Earth. Subsequent analysis has shown that the instrument characteristics, the mounting of the instrument on top of the lander bus, and the elastic attenuation within Mars would have prevented the detection of even a magnitude 9 event on Tharsis by the Viking 2 lander in Utopia Planitia (Goins and Lazarewicz 1979), such that the information gathered by the Viking experiments is of limited value.

On the other hand, several authors have shown that a significant seismicity is to be expected on Mars. Phillips (1991) evaluated different sources of elastic deformations and concluded that secular cooling of the martian lithosphere is the most effective one, resulting in a seismic moment release of 4.8×10^{18} Nm/yr (see Fig. 16 for a conversion of seismic moment into magnitudes). Golombek et al. (1992) estimated from an assessment of the total slip of visible faults that the annual moment release is about 10^{18} Nm. Knapmeyer et al. (2006) combined the approach of Phillips (1991) with new results on planetary cooling rates, a magnitude-frequency relation, and a geographic source distribution model. Based on the uncertainties of all input parameters, Knapmeyer et al. (2006) conclude that the moment release is between 3.4×10^{16} Nm/yr and 4.8×10^{18} Nm/yr (Fig. 16). Since Mars lacks the microseismic noise generated by oceans, even magnitude 4 events will be globally detectable by well-deployed modern instrumentation (e.g., Dehant et al. 2012a). If the Tharsis

volcanoes are still active today, as suggested by Neukum et al. (2004), a spatial concentration of seismic activity beyond the distribution model proposed by Knapmeyer et al. (2006) may result. Further indications for seismic activity come from observations of fallen boulder populations in Cerberus Fossae (Roberts et al. 2012), as well as from faults crosscutting young lava flows (Vaucher et al. 2009).

The endogenous seismicity of Mars is complemented by meteorite influx. While Davis (1993) estimated from an upscaled meteorite flux of the Earth that an Apollo-type seismometer on Mars could expect to detect about 116 meteorite impacts per year, Teanby and Wookey (2011) estimated from the rate of direct cratering observations that globally detectable impacts occur only once every few years. The differences between these two estimates and also the flux that could be expected according to the "meteoritic hum" model of Lognonné et al. (2009) reflect the uncertainties of flux scaling between different planets and also of the estimated seismic efficiency of impacts.

Gravity-based models of the crustal thickness (Zuber et al. 2000) would benefit from one or more anchor points of seismological measurements, not only to resolve the thickness-density trade-off, but also to account for lateral variations of crustal density. Using a network of at least three stations, deployed in a seismically active region, this can be achieved using the classical inversion of travel time curves especially for the Moho head wave. A modern standard method that can be applied with teleseismic data recorded at a single three-component station, is the receiver function inversion of Zhu and Kanamori (2000). This approach yields a best fitting value not only for the Moho depth, but also for the Poisson ratio of the crustal rock. It does not necessarily need precise source locations if the crustal scattering is not too strong and thus the slowness of the incoming P wave can be estimated from the computation of the receiver functions themselves (Knapmeyer and Harjes 2000).

Core size is one of the main parameters controlling the existence of the perovskite phase transition in the deep martian mantle (Bertka and Fei 1998; Sohl and Spohn 1997), and knowledge of the core size would thus have important consequences for models of martian mantle dynamics (see Sect. 5.3). Furthermore, knowledge of the core size would constrain the size of the mantle reservoir. If seismic source location and time were known, a single station would suffice to determine the size of the martian core by exploiting the almost linear relationship between core size and the extent of the P wave core shadow (Oldham 1906; Knapmeyer 2011). Source localization could be achieved by monitoring meteorite impacts by camera observation of the flashes that are caused by thermal radiation of vaporized target material (Bouley et al. 2012). Observations of lunar impacts can be conducted with Earth based telescopes (Suggs et al. 2008), and it has been proposed to use impact flashes to localize seismic sources by Mimoun et al. (2012b). In the case of Mars, an orbiter could be parked in the Sun-Mars Lagrange point L2, from which it would always see the martian night side, or in a sun-synchronous orbit, which would be much closer to the martian surface but would also allow to view the surface at a specific local time.

Another approach that can be applied to data from only a single station is the interpretation of free oscillations of the planet. These allow inferring not only the seismic velocities, but also the density structure of the deep interior and the core size. Usually known for being excited by strong earthquakes, it has been found that Earth's free oscillations are continuously excited by dynamic pressures exerted by the atmosphere, and that the atmospheric activity of Mars is also likely to excite free oscillations of the planet (Kobayashi and Nishida 1998). The InSight mission (Banerdt et al. 2012) will carry a seismometer (Mimoun et al. 2012a) to the surface of Mars and establish a first single-station geophysical observatory.

6.5 Radio Science

The mean moment of inertia of Mars provides a global constraint on the radial density profile of Mars and as such contains information on the crust and mantle structure. The moment of inertia with respect to the polar axis has been obtained from radio science measurements in which two-way Doppler and ranging measurements are performed on radio links between ground stations on the Earth and the Mars Pathfinder and Viking landers on the surface of Mars. In addition, radio links between the Earth and orbiters around Mars have been used. From these measurements, the precession rate of Mars, which is inversely proportional to the polar moment of inertia, can be derived. By combining precession estimates with the accurately known degree-two gravitational field of Mars, the mean moment of inertia has been determined with a relative precision of about 0.1 % (Konopliv et al. 2011). Although this result is rather precise, no accurate direct inferences can be made on the size and composition of the mantle and crust because the moment of inertia of Mars also depends on the properties of the core. In particular, the core composition, temperature, and radius are not sufficiently well known to allow for an accurate determination of the core contribution to the moment of inertia. From indirect measurements of the tides on Mars raised by the Sun (Konopliv et al. 2011), the currently most accurate estimate of the core radius is 1794 ± 65 km (Rivoldini et al. 2011), corresponding to 53 % of the planetary radius.

Using radio tracking of a single lander over an extended period of time (one Martian year or more), the error on the precession estimate could be decreased by at least a factor of five (Dehant et al. 2009; Le Maistre et al. 2012). Recent analyses of several months of tracking data of the Mars Exploration Rover Opportunity already lead to an improved estimate of the precession rate (Le Maistre et al. 2010; Kuchynka et al. 2012). Further improvements are expected with multiple landers (Yseboodt et al. 2003) and interferometric techniques (Iess et al. 2012; Dehant et al. 2012b). This would set a stronger global constraint on the radial density profile in Mars, but more importantly the nutation (the periodic changes in the orientation) of Mars could be measured with such a radio science experiment. The main nutations of Mars have annual, semi-annual, and ter-annual periods in inertial space with amplitudes of up to about 500 milliarcsecond, corresponding to a displacement at the surface of Mars of about 8 m (Roosbeek 2000; Dehant et al. 2000). Nutation is particularly interesting since it depends on the moment of inertia of the core and some of the main nutations are amplified by a resonance with a free mode, the Free Core Nutation, representing a rigid rotation of the core around the rotation axis of the mantle. With a single equatorial lander, and one Martian year of Doppler data, the core moment of inertia could be determined with a precision of 30 % (Le Maistre et al. 2012) and significantly better precisions are expected with more advanced radio tracking experiments. The advantage of nutation observations in addition to precession is that the moments of inertia of the core and the silicate mantle and crust can be determined independently, allowing to set improved constraints on the density profile in both the core and the silicate outer part of Mars.

6.6 Sample Return

Returned samples of igneous martian rocks would dramatically increase our understanding of the planet's thermal evolution. Although the 104 martian meteorites provide important insights into critical topics such as mantle mineralogy and water content, the timing of differentiation and the thermal state of the interior (see, e.g., McLennan et al. 2011 and references therein), they have significant shortcomings. Despite several attempts, for example,

the source regions of the SNC meteorites are unknown. Therefore, they lack field context, which limits their use as ground truth for orbital measurements (see Table 2 in McLennan et al. 2011 for a list of main shortcomings of SNCs as representative samples of Mars).

The ability to determine absolute model ages of the martian surface by analysis of crater size-frequency distributions is limited by the lack of radiometrically dated samples of a known origin, which are required to calibrate the crater dating method. For the case of the Moon, this critical knowledge comes from the samples collected and returned by the Apollo missions (e.g., Neukum and Ivanov 1994). For the case of Mars, a fresh igneous sample of early Amazonian age (e.g., 2 Ga) from a surface unit with a one-stage emplacement history would provide an important calibration measurement in the range of the cratering curve that is least constrained (Neukum 1988). Thus, sample return (or in situ dating by landers or rovers) would dramatically improve global dating from orbital imaging (Hartman and Neukum 2001).

Even younger volcanic rocks would also bear information on the range of volcanic processes and the role of water on recent Mars. On the other hand, samples of ancient igneous rocks have the potential to inform on early interior and surface processes. Early Noachian rocks might reveal details on silicate differentiation, on the crystallization of a magma ocean and its possible overturn, the formation of initial reservoirs and a primitive crust (McLennan et al. 2011). Preferred lithologies would include (a) cumulate-free basalts, from the chilled flow margin to the flow interior, to infer the properties of the parent melt, (b) ultramafic rocks with xenoliths from the mantle or lower crust, to study the mantle mineralogy and the thermal state of the martian interior, and (c) evolved igneous rocks, to study the diversity of igneous compositions and test hypotheses on the existence of felsic (granitic) rocks on Mars (e.g., Bandfield et al. 2004).

Paleomagnetic measurements of ancient martian rocks, both in situ or using returned samples, would be a major step towards a better knowledge of the intensity and timing of the magnetic field (Weiss et al. 2008). Such knowledge is essential to understand the thermal evolution of the martian core, the possibility of early plate tectonics, and the atmospheric loss on early Mars (Weiss et al. 2008). Ideally, strategies would focus on the acquisition of oriented samples from coherent bedrock (e.g., bedded basalts) with paleohorizonal indicators (Weiss et al. 2008), containing primary igneous magnetic minerals such as titanomagnetite and pyrrhotite (McLennan et al. 2011).

6.7 Theoretical and Laboratory Studies

The surface of Mars preserves a long-standing record of the planet's thermal evolution and this situation may be unique in the solar system. Estimates of lithospheric thicknesses, numerical modeling of mantle convection, mineralogical and chemical observations of igneous rocks (in-situ, from orbit, and in the lab) help reconstruct the planet's volcanic history, and geomorphological observations provide complementary insight into the magmatic evolution of the crust-mantle system. However, integrating the different observations into a consistent picture remains a challenging goal, which requires discrimination between global trends and local diversity, which naturally results from mantle heterogeneities and small-scale processes.

A major challenge for integrating different approaches is related to age determinations and there may be considerable timing discrepancies when characterizing a site using geophysical and petrological methods. While estimates of the local elastic thickness and heat flow usually date the time the bulk of a load was emplaced onto the surface (e.g., McGovern et al. 2002; Belleguic et al. 2005; Grott et al. 2005, 2011; Ruiz et al.

2009, 2011) petrological (Monders et al. 2007; Filiberto et al. 2010, 2011; Baratoux et al. 2011a) and geomorphological (e.g., Werner 2009; Robbins et al. 2011; Vaucher et al. 2009; Hauber et al. 2011) studies tend to date the last resurfacing events. Therefore, it is difficult to link the derived thermal state to the observed petrology, and a better understanding of the timing for the construction of volcanic surfaces is required.

Problems encountered when modeling the thermal evolution of the martian mantle include a lack of knowledge of the involved transport parameters, which generally have relatively large uncertainties. In particular, the thermal conductivity of the crust and lithospheric mantle are only known to within a factor of 2 for the deeper part (Breuer and Moore 2009), and due to their dependence on porosity, pore size, and cementation (Piqueux and Christensen 2009a, 2009b) their values are even more uncertain for the upper crust (<1 km). This range may be narrowed down by experimental studies of the thermal properties of iron-rich materials, analogous to the martian crust and mantle, and a determination of the regolith thickness. Thermodynamic relations and the process of melting in the iron-rich martian mantle also need to be addressed and validated by experimental investigations.

A major shortcoming when trying to link morphological observations to the nature of the lavas is the lack of experimental data on extra-terrestrial silicate melts such as the iron- and phosphorous-rich martian magmas (Chevrel et al. 2011a, 2011b). Lava rheology also bears on the process of magma ascent, which influences the chemistry of primitive melts by crustal contamination and fractional crystallization. Although geochemical observations suggest that a large proportion of the volcanically emplaced surfaces is in appearance consistent with primary melts of the primitive martian mantle (Baratoux et al. 2011a), the SNCs emphasize that details of the petrological processes need to be considered to explain the large range of Mg# and REE content (Meyer 2009). In addition, real primary melts are rare on Earth, which might indicate that spatial averaging on the regional scale might also mask the petrological complexity of crustal sections on Mars as inferred from orbit.

Evidence from remote sensing, in-situ analysis, and the analysis of the SNC meteorites suggests that primary and evolved liquids, crustal contamination, and cumulate rocks are present on Mars. The resolution of remote sensing instruments is now able to reveal, for instance, the magmatic signature of dikes along with that of their host rocks in the walls of Valles Marineris (Flahaut et al. 2011), and this opens up the possibility to explore the process of intrusive magma emplacement in more detail. In addition, the mineralogical analysis of a wide range of magmatic ages is important to confirm mineralogical trends, such as the change in pyroxene compositions at the Noachian/Hesperian boundary. Global changes in mineral chemistry may then be linked to the evolution of conditions for partial melting, and thus, to the thermal evolution of the martian mantle.

7 Summary and Conclusions

Present-day Mars operates in the stagnant lid mode of mantle convection, and geological evidence suggests that this has been the case since the planet's earliest evolution. In addition, isotopic ratios in the martian meteorites indicate that no significant mixing of early established geochemical reservoirs occurred (Chen and Wasserburg 1986; Harper et al. 1995; Borg et al. 1997; Brandon et al. 2000; Halliday et al. 2001), implying that crustal rock was not recycled back into the mantle. Therefore, the evolution of the crust-mantle system was driven by partial mantle melting, silicate differentiation, and volcanism. The martian surface bears witness to a rich history of volcanic processes and volcanism appears to have been a global process during the early evolution of the planet (Werner 2009). As planetary cooling

progressed, activity became more and more focused, and the youngest volcanic surfaces are found exclusively in the Tharsis and Elysium volcanic provinces. Crater retention ages of these surfaces indicate a relatively recent emplacement, a possible indication that the process of mantle differentiation is ongoing today.

The total amount of mantle differentiation is poorly constrained and geophysical studies estimate the martian crust to be 57 ± 24 km thick on average (Wieczorek and Zuber 2004). Other information to constrain the amount of mantle differentiation is derived from photogeological estimates of crustal production rates (Greeley and Schneid 1991), but these estimates suffer from the fact that old surfaces are often covered by younger flows and are thus not accessible to investigation. In this sense, the scarcity of observed Noachian volcanic material is almost certainly an observational bias. In addition, only a minor part of the magma is expected to be extruded onto the surface, and intruded volumes are generally believed to be 5 to 10 times larger than extruded volumes (Lillis et al. 2009). Therefore, the crustal thickness must be viewed as uncertain to within a factor of two, a situation which could be improved by future seismological investigations (Dehant et al. 2012a).

The thickness of the martian crust is an indicator for the total amount of mantle differentiation, which remains equally uncertain. As the amount of incompatible elements removed from the mantle is proportional to the amount of produced crust, this uncertainty also affects the distribution of H_2O, K, Th, and U between crust and mantle. Numerical models indicate that about 50 % of these elements were removed from the mantle to the crust if an average crustal thickness of 50 km is assumed (Kiefer 2003; Morschhauser et al. 2011; Grott et al. 2011), but this value might need to be revised when better estimates of the total crustal thickness become available.

Information on the differentiation products, i.e., igneous rocks, comes from a variety of sources including remote sensing, in-situ analysis, and laboratory investigations. Martian igneous rocks are predominantly mafic in composition, and SiO_2 contents of 41–44 wt% and 44–47 wt% have been reported on the basis of gamma ray data for Amazonian and Hesperian surface units, respectively (Baratoux et al. 2011a; Gasnault et al. 2010). The composition of the Noachian crust is less well constrained, as it has been heavily altered. Unaltered representative units detectable at the scale of the gamma ray data resolution have not been unambiguously identified, and the composition of the Noachian crust is difficult to quantify from orbit. In-situ data generally agree with a mafic composition of the martian crust, and few more felsic compositions have been identified (Foley et al. 2003; Brückner et al. 2003).

Geochemical analysis of the SNC meteorites as well as remote sensing data indicate that igneous rocks on Mars may have crystallized from primary melts, with little magma storage at depth (Bertka and Fei 1997; Schmidt and McCoy 2010; Baratoux et al. 2011a). Although evidence for magmatic differentiation exists, it appears to be volumetrically minor. TES and THEMIS measurements of Nili Patera indicate a dacitic composition, enriched in SiO_2 relative to the basaltic composition that dominates Syrtis Major (Christensen et al. 2005), and even more extreme magmatic differentiation products rich in quartz may be present in other areas of the Syrtis Major region (Bandfield et al. 2004; Christensen et al. 2005; Bandfield 2006). Although these examples appear to be isolated, they nevertheless indicate that magmatic differentiation has occurred on Mars.

The composition of the martian crust as observed by gamma ray spectroscopy indicates that mantle melting during the Hesperian likely took place at temperatures between 1650 and 1700 K, and that magma source regions were located at depths between 90 and 110 km (Baratoux et al. 2011a). The degree of partial melting is estimated to have been 10–15 %, and a general trend from old, high temperature, high melt fraction melting to young, lower

temperature, small melt fraction melting is observed. Accordingly, Amazonian volcanism is associated with temperatures between 1600 and 1670 K, source region depths around 150 km, and melt fractions between 5 and 12 % (Baratoux et al. 2011a). These estimates are consistent with depths derived from the Gusev crater basalts, which indicate source region depths around 85 km for these likely Hesperian aged rocks. Estimates of mantle temperature, source region depth, and melt fraction are in general agreement with numerical models of the thermo-chemical evolution of Mars, which predict magma source region depths around 100–200 km and melt fractions between 20 and 5 % during the Hesperian and Amazonian periods (Morschhauser et al. 2011; Grott et al. 2011).

Our understanding of the process of mantle differentiation is hampered by our lack of knowledge of the mantle water content, which has a large influence on the efficiency of mantle convection (Karato 2011) and could strongly affect the mantle solidus (e.g., Hirschmann 2000). Estimates of the mantle water content range from relatively dry (1–36 ppm H_2O) (Wänke and Dreibus 1994; Mysen et al. 1998; Filiberto and Treiman 2009) to moderately wet conditions (55–220 ppm H_2O) (McSween et al. 2001; McCubbin et al. 2010), but given that only small amounts of water are needed to be rheologically significant (Mei and Kohlstedt 2000a; Mei and Kohlstedt 2000b), the martian mantle is best described by a wet or only partially dehydrated rheology. Independent evidence for rheologically significant amounts of water in the martian crust and mantle comes from elastic thickness studies (Grott and Breuer 2010), and wet mantle rheologies are also preferred by thermo-chemical evolution models (Hauck and Phillips 2002; Grott et al. 2011; Morschhauser et al. 2011; Fraeman and Korenaga 2010). Geochemical analysis of the SNC meteorites indicates an upper limit of 220 ppm water in the martian mantle (McSween et al. 2001; McCubbin et al. 2010), which could result in a solidus reduction of $\sim$100 K (Katz et al. 2003). It therefore remains to be investigated whether petrologically significant amounts of water (in excess of $\sim$100 ppm) are present in the martian interior. While the bulk mantle water content remains poorly constrained, electro-magnetic sounding experiments would help to better quantify this value (Grimm 2002).

The thermo-chemical evolution of Mars is largely driven by the heat liberated in its interior, and the bulk abundance of heat producing elements has been estimated from the SNC meteorites. The most widely accepted compositional model (WD94, Wänke and Dreibus 1994) predicts abundances of 16 ppb U, 56 ppb Th, and 305 ppm K, and the predicted abundance ratio of K/Th closely matches the observed ratio of K/Th on the martian surface (Taylor et al. 2006). Radioactive elements in the WD94 model produce heat at a rate comparable to heat production in chondritic meteorites, and numerical models using these abundances are in good agreement with the inferred thermo-chemical evolution of the planet (Hauck and Phillips 2002; Grott et al. 2011; Morschhauser et al. 2011; Fraeman and Korenaga 2010). However, recent estimates of the elastic lithosphere thickness at the polar caps indicate a very cold lithosphere (Phillips et al. 2008), which could either imply a spatially heterogeneous mantle heat flow (Kiefer and Li 2009; Grott and Breuer 2010), or a sub-chondritic heat production rate in the martian interior. If the latter were true, models for the thermo-chemical evolution of Mars would need to be revisited, and in-situ heat flow measurements are needed to directly address this question (Kömle et al. 2011; Dehant et al. 2012a).

Acknowledgements M. Grott, E. Hauber, D. Breuer, and F. Sohl acknowledge funding by the Helmholtz Association through the research alliance "Planetary Evolution and Life". D. Baratoux and M.J. Toplis acknowledge funding from the Programme National de Planétologie of INSU. T. Van Hoolst acknowledges funding from the Belgian PRODEX program managed by the European Space Agency in collaboration with the Belgian Federal Science Policy Office.

References

M.H. Acuña, G. Kletetschka, J.E.P. Connerney, in *The Martian Surface: Composition, Mineralogy, and Physical Properties*, ed. by J.F. Bell III (Cambridge University Press, Cambridge, 2008), pp. 242–262, Chap. 11

J.B. Adams, J. Geophys. Res. **79**, 4829–4836 (1974)

R.A. Albert, R.J. Phillips, Geophys. Res. Lett. **27**(16), 2385–2388 (2000)

D.L. Anderson, W.F. Miller, G.V. Latham et al., J. Geophys. Res. **82**, 4524–4546 (1977)

J.C. Andrews-Hanna, M.T. Zuber, W.B. Banerdt, Nature **453**(7199), 1212–1215 (2008)

F. Anguita, C. Fernández, G. Cordero et al., Icarus **185**(2), 331–357 (2006)

R.E. Arvidson, S.W. Ruff, R.V. Morris et al., J. Geophys. Res. **113**, E12S33 (2008)

R.D. Ash, S.F. Knott, G. Turner, Nature **380**(6569), 57–59 (1996)

P.D. Asimow, C.H. Langmuir, Nature **421**, 815–820 (2003)

J.L. Bandfield, J. Geophys. Res. **107**, E6 (2002)

J.L. Bandfield, Geophys. Res. Lett. **33**, L06203 (2006)

J.L. Bandfield, V.E. Hamilton, P.R. Christensen, Science **287**, 1626–1630 (2000)

J.L. Bandfield, V.E. Hamilton, P.R. Christensen, H.Y. McSween, J. Geophys. Res. **109**(10), E10009 (2004)

W.B. Banerdt, S.E. Smrekar, L. Alkalai et al., *43rd Lunar and Planetary Science Conference*, abstract 2838 (2012)

A.R. Baptista, N. Mangold, V. Ansan et al., J. Geophys. Res. **113**(E12), E09010 (2008)

D. Baratoux, P. Pinet, A. Gendrin et al., J. Geophys. Res. **112**(E11), E08S05 (2007)

D. Baratoux, M.J. Toplis, M. Monnereau et al., Nature **472**, 338–341 (2011a)

D. Baratoux, N. Mangold, O. Arnalds et al., Earth Surf. Process. Landf. **36**, 1789–1808 (2011b)

D.N. Barnett, F. Nimmo, Icarus **157**(1), 34–42 (2002)

E.A. Basilevskaya, G. Neukum, Sol. Syst. Res. **40**, 375–383 (2006)

P. Beck, J.-A. Barrat, P. Gillet et al., Geochim. Cosmochim. Acta **70**, 2127–2139 (2006)

J.F. Bell III, T.B. McCord, P.D. Owensby, J. Geophys. Res. **95**, 14447–14461 (1990)

V. Belleguic, P. Lognonne, M. Wieczorek, J. Geophys. Res. **110**, E11005 (2005)

C.M. Bertka, Y. Fei, J. Geophys. Res. **107**, 5251–5264 (1997)

C.M. Bertka, Y. Fei, Science **281**, 1838–1840 (1998)

C.M. Bertka, J.R. Holloway, Contrib. Mineral. Petrol. **115**(3), 313–322 (1994a)

C.M. Bertka, J.R. Holloway, Contrib. Mineral. Petrol. **115**(3), 323–338 (1994b)

M. Beuthe, S. Le Maistre, P. Rosenblatt et al., J. Geophys. Res. **117**, E04002 (2012)

J.-P. Bibring, M. Combers, Y. Langevin et al., Nature **341**, 591–593 (1989)

J.-P. Bibring, A. Soufflot, M. Berthé et al., in *Mars Express: the Scientific Payload*, ed. by A. Wilson (ESA Publications, Noordwijk, 2004), pp. 37–49. ISBN:92-9092-556-6

J.-P. Bibring, Y. Langevin, A. Gendrin et al., Science **307**, 1576–1581 (2005)

J.-P. Bibring, Y. Langevin, J.F. Mustard et al., Science **312**, 400–404 (2006)

J.L. Bishop, M. Parente, C.M. Weitz et al., J. Geophys. Res. **114**(E13), E00D09 (2009)

J.E. Bleacher, R. Greeley, D.A. Williams et al., J. Geophys. Res. **112**, 9005 (2007)

D.D. Bogard, P. Johnson, Science **221**, 651–654 (1983)

L.E. Borg, L.E. Nyquist, L.A. Taylor et al., Geochim. Cosmochim. Acta **61**, 4915 (1997)

L.E. Borg, L.E. Nyquist, H. Wiesmann et al., *31 Lunar and Planetary Institute Science Conference*, abstract 1036 (2000)

L.E. Borg, L.E. Nyquist, H. Wiesmann, Y. Reese, Geochim. Cosmochim. Acta **66**, 2037–2053 (2002)

L.E. Borg, J.E. Edmunson, Y. Asmeron, Geochim. Cosmochim. Acta **69**, 5819–5830 (2005)

S. Bouley, D. Baratoux, J. Vaubaillon, Icarus **218**, 115–124 (2012)

A. Bouvier, J. Blichert-Toft, J.D. Vervoort, F. Albarède, Earth Planet. Sci. Lett. **240**, 221–233 (2005)

A. Bouvier, J. Blichert-Toft, J.D. Vervoort et al., Earth Planet. Sci. Lett. **266**, 105–124 (2008)

A. Bouvier, J. Blichert-Toft, F. Albarède, Earth Planet. Sci. Lett. **280**, 285–295 (2009)

W.V. Boynton, G.J. Taylor, L.G. Evans et al., J. Geophys. Res. **112**, E12S99 (2007)

W.V. Boynton, G.J. Taylor, S. Karunatillake et al., Elemental abundances determined via the Mars Odyssey GRS, in *The Martian Surface: Composition, Mineralogy, and Physical Properties*, ed. by J.F. Bell III (Cambridge University Press, Cambridge, 2008), pp. 105–124

W.V. Boynton, D.W. Ming, S.P. Kounavas et al., Science **325**(5936), 61–64 (2009)

A.D. Brandon, R.J. Walker, J.W. Morgan et al., Geochim. Cosmochim. Acta **64**, 4083–4095 (2000)

A.D. Brandon, I.S. Puchtel, R.J. Walker et al., Geochim. Cosmochim. Acta **76**, 206–235 (2012)

D. Breuer, W.B. Moore, in *Treatise of Geophysics*, vol. 10, (2009), pp. 299–341

D. Breuer, T. Spohn, J. Geophys. Res. **108**(E7), 507 (2003)

D. Breuer, T. Spohn, Planet. Space Sci. **54**, 153–169 (2006)

D. Breuer, D.A. Yuen, T. Spohn et al., Geophys. Res. Lett. **25**(3), 229–232 (1998)

J.C. Bridges, P.H. Warren, J. Geol. Soc. **163**, 229–251 (2006)
C.D. Brown, R.J. Phillips, J. Geophys. Res. **105**(B6), 13221–13238 (2000)
P. Brož, E. Hauber, Icarus **218**, 88–99 (2012)
J. Brückner, G. Dreibus, R. Rieder et al., J. Geophys. Res. **108**(E12), 8094 (2003)
R.G. Burns, *Mineralogical Applications of Crystal Field Theory*, 2nd edn. (Cambridge University Press, Cambridge, 1993a), 551 pp.
R.G. Burns, Origin of electronic spectra of minerals in the visible-near infrared region, in *Remote Geochemical Analysis: Elemental and Mineralogical Composition*, ed. by C. Pieters, P. Englert (Cambridge University Press, Cambridge, 1993b), pp. 3–29
E.B. Burov, M. Diament, J. Geophys. Res. **100**(B3), 3905–3927 (1995)
M. Buske, *Three-dimensional thermal evolution models for the interior of Mars and Mercury*, Ph.D. Thesis, University of Göttingen (2006)
M.H. Carr, R. Greeley, *Volcanic features of Hawaii*, NASA pub. SP-403 (1980), 211 pp.
M. Chen, A. El Goresy, Earth Planet. Sci. Lett. **179**, 489–502 (2000)
J.H. Chen, G.J. Wasserburg, Geochim. Cosmochim. Acta **50**, 955–968 (1986)
M. Chevrel, D. Dingwell, D. Baratoux, D. Giordano, *42nd International Union for Geodesy and Geophysics Conference*, Melbourne, Australia, abstract 4031 (2011a)
M. Chevrel, T. Platz, E. Hauber, D. Dingwell, *42nd International Union for Geodesy and Geophysics Conference*, Melbourne, Australia, abstract 4029 (2011b)
V. Chevrier, J.-P. Lorand, V. Sautter, Meteorit. Planet. Sci. **46**, 769–784 (2011)
F. Christen, O. Eugster, H. Buseman, Antarct. Meteor. Res. **18**, 117 (2005)
P.R. Christensen, H.J. Moore in *Mars*, ed. by H.H. Kieffer et al.(University of Arizona Press, Tucson, 1992) pp. 686–729
P.R. Christensen, J.L. Bandfield, V.E. Hamilton et al., J. Geophys. Res. **106**(E10), 23823–23872 (2001)
P.R. Christensen, J.L. Bandfield, J.F. Bell et al., Science **300**, 2056–2061 (2003)
P.R. Christensen, M.B. Wyatt, T.D. Glotch et al., Science **306**(5702), 1733–1739 (2004)
P.R. Christensen, H.Y. McSween, J.L. Bandfield et al., Nature **436**(7050), 504–509 (2005)
R.N. Clark, in *Spectroscopy of rocks and minerals and principles of spectroscopy, in Manual of Remote Sensing*, ed. by A.N. Rencz (Wiley, New York, 1999), pp. 3–58
R.N. Clayton, T.K. Mayeda, Geochim. Cosmochim. Acta **60**, 1999–2017 (1996)
E.A. Cloutis, M.J. Gaffey, T.L. Jackowski, J. Geophys. Res. **91**, 11641–11653 (1986)
R.P. Comer, S.C. Solomon, J.W. Head, Rev. Geophys. **23**, 61–92 (1985)
J.E.P. Connerney, M.H. Acuña, P.J. Wasilewski et al., Science **284**(5415), 794–798 (2000)
J.E.P. Connerney, M.H. Acuña, N.F. Ness et al., Proc. Natl. Acad. Sci. USA **102**(42), 14970–14975 (2005)
J.A. Crisp, J. Volcanol. Geotherm. Res. **20**, 177–211 (1984)
D.A. Crown, R. Greeley, J. Geophys. Res. **98**, 3431–3451 (1993)
L.S. Crumpler, J.W. Head, J.C. Aubele, Calderas on Mars: Characteristics, Structure, and Associated Flank Deformation, in *Volcano Instability on the Earth and Other Planets*, vol. 110, ed. by W.C. McGuire, A.P. Jones, J. Neuberg (Geological Society Special Publication, London, 1996), pp. 307–347
P.M. Davis, Icarus **105**, 469 (1993)
J.M.D. Day, L.A. Taylor, C. Floss et al., Meteorit. Planet. Sci. **41**, 581–606 (2006)
R.A. De Hon, in *5th Proc. Lunar Planet. Sci. Conf.*, (1974), pp. 2553–2561
R.A. De Hon, J. Geophys. Res. **87**, 9821–9828 (1982)
J.H. de Smet, A.P. van den Berg, N.J. Vlaar, Lithos **48**, 153–170 (1999)
V. Debaille, Q.-Z. Yin, A.D. Brandon, Earth Planet. Sci. Lett. **269**, 186–199 (2008)
V. Dehant, P. Defraigne, T. Van Hoolst, Phys. Earth Planet. Inter. **117**, 385–395 (2000)
V. Dehant, W. Folkner, E. Renotte et al., Planet. Space Sci. **57**, 1050–1067 (2009)
V. Dehant, B.W. Banerdt, P. Lognonné et al., Planet. Space Sci. (2012a). doi:10.1016/j.pss.2011.10.016
V. Dehant, M. Yseboodt, M. Mitrovic et al, Abstract EGU (2012b)
B. Diez, W.C. Feldman, N. Mangold et al., Icarus **200**, 19–29 (2009)
G. Dreibus, H. Wänke, Meteoritics **20**, 367–381 (1985)
A.M. Dziewonski, A. Friedman, D. Giardini et al., Phys. Earth Planet. Inter. **33**, 76–90 (1983)
B.L. Ehlmann, J.F. Mustard, G.A. Swayze et al., J. Geophys. Res. **114**(E13), E00D08 (2009)
M.R. El Maarry, O. Gasnault, M.J. Toplis et al., J. Volcanol. Geotherm. Res. **185** (2009)
L.T. Elkins-Tanton, E.M. Parmentier, P.C. Hess, Meteorit. Planet. Sci. **38**(12), 1753–1771 (2003)
L.T. Elkins-Tanton, P.C. Hess, E.M. Parmentier, J. Geophys. Res. **110**, E12S01 (2005)
R.E. Ernst, E.B. Grosfils, D. Mège, Annu. Rev. Earth Planet. Sci. **29**, 489–534 (2001)
L.G. Evans, R.C. Reedy, R.D. Starr et al., J. Geophys. Res. **111**, E03S04 (2006)
L.G. Evans, R.C. Reedy, R.D. Starr et al., *Lunar and Planetary Science Conference*, abstract 1875 (2008)
A.G. Fairén, J. Ruiz, F. Anguita, Icarus **160**(1), 220–223 (2002)
W.H. Farrand, L.R. Gaddis, L. Keszthelyi, J. Geophys. Res. **110**(E9), E05005 (2005)

W.H. Farrand, M.D. Lane, B.R. Edwards et al., Icarus **211**, 139–156 (2011)
C.I. Fassett, J.W. Head, Icarus **195**, 61–89 (2008)
U.H. Faul, I. Jackson, Earth Planet. Sci. Lett. **234**, 119–134 (2005)
W.C. Feldman, A. Pathare, S. Maurice et al., J. Geophys. Res. **116**(E11), E11009 (2011)
J.R. Filiberto, R. Dasgupta, Earth Planet. Sci. Lett. **304**, 527–537 (2011)
J.R. Filiberto, A.H. Treiman, Geology **37**(12), 1087–1090 (2009)
J.R. Filiberto, A.H. Treiman, L. Le, Meteorit. Planet. Sci. **43**, 1137–1146 (2008)
J.R. Filiberto, R. Dasgupta, W.S. Kiefer, A.H. Treiman, Geophys. Res. Lett. **37**, L13201 (2010)
J. Fink, J. Volcanol. Geotherm. Res. **4**, 151–170 (1978)
J. Flahaut, J.F. Mustard, C. Quantin et al., Geophys. Res. Lett. **38**, L15202 (2011)
R.J. Floran, M. Prinz, P.F. Hlava et al., Geochim. Cosmochim. Acta **42**, 1213–1229 (1978)
C.N. Foley, T. Economou, R.N. Clayton, J. Geophys. Res. **108**(E12), 8096 (2003)
A.A. Fraeman, J. Korenaga, Icarus **210**, 43–57 (2010)
H.V. Frey, R.A. Schultz, Geophys. Res. Lett. **15**, 229–232 (1988)
H.V. Frey, J.H. Roark, K.M. Shockey et al., Geophys. Res. Lett. **29**(10), 1384 (2002)
A.M. Gaffnee, L.E. Borg, Y. Asmeron et al., Meteorit. Planet. Sci. **46**, 35–52 (2011)
F. Gaillard, M. Malki, G. Iacono-Marziano et al., Science **322**, 1363–1365 (2008)
O. Gasnault, G.J. Taylor, S. Karunatillake et al., Icarus **207**, 226–247 (2010)
C. Goetze, B. Evans, Geophys. J. R. Astron. Soc. **59**, 463–478 (1979)
N.R. Goins, A.R. Lazarewicz, Geophys. Res. Lett. **6**, 368–370 (1979)
G.J. Golabek, T. Keller, T.V. Gerya et al., Icarus **215**(1), 346–357 (2011)
M.P. Golombek, W.B. Banerdt, K.L. Tanaka et al., Science **258**(5084), 979–981 (1992)
C.A. Goodrich, Meteorit. Planet. Sci. **37**, 31 (2002)
J.A. Grant, P.H. Schultz, Icarus **84**, 166–195 (1990)
O. Grasset, E.M. Parmentier, J. Geophys. Res. **103**, 18171–18181 (1998)
R. Greeley, D.A. Crown, J. Geophys. Res. **95**, 7133–7149 (1990)
R. Greeley, S.A. Fagents, J. Geophys. Res. **106**, 20527–20546 (2001)
R. Greeley, B.D. Schneid, Science **254**, 996–998 (1991)
R. Greeley, P.D. Spudis, Rev. Geophys. Space Phys. **19**, 13–41 (1981)
R. Greeley, N.T. Bridges, D.A. Crown et al., Volcanism on the Red Planet: Mars, in *Environmental Effects on Volcanic Eruptions: from Deep Oceans to Deep Space*, ed. by J. Zimbelman, T. Gregg (Kluwer Academic/Plenum Publishers, New York, 2000), pp. 75–112
R. Greeley, B.H. Foing, H.Y. McSween et al., J. Geophys. Res. **110**, E05008 (2005)
T.K.P. Gregg, S.N. Williams, Icarus **122**, 397–405 (1996)
R.W. Griffiths, J.H. Fink, J. Geophys. Res. **97**, 19739–19748 (1992)
R.E. Grimm, J. Geophys. Res. **107**(E2), 5006 (2002)
J. Gross, J. Filiberto, A.H. Treiman et al. *43rd LPSC*, abstract 2693 (2012)
M. Grott, D. Breuer, Icarus **193**(2), 503–515 (2008)
M. Grott, D. Breuer, Icarus **201**(2), 540–548 (2009)
M. Grott, D. Breuer, J. Geophys. Res. **115**, E03005 (2010)
M. Grott, M.A. Wieczorek, Icarus **221**, 43–52 (2012)
M. Grott, E. Hauber, S.C. Werner et al., Geophys. Res. Lett. **32**, L21201 (2005)
M. Grott, E. Hauber, S.C. Werner et al., Icarus **186**, 517–526 (2007a)
M. Grott, A. Morschhauser, D. Breuer, E. Hauber, Earth Planet. Sci. Lett. **308**(3–4), 391–400 (2011)
J.P. Grotzinger, The Mars Science Laboratory Mission. Abstr. Program - Geol. Soc. Am. **43**(5), 411 (2011)
J.P. Grotzinger, R.E. Milliken, The Sedimentary Rock Record of Mars: Distribution, Origins, and Global Stratigraphy, in *Sedimentary Geology of Mars*, ed. by J.P. Grotzinger, R.E. Milliken (SEPM Special Publication, Tulsa, 2011)
J.P. Grotzinger, R.E. Arvidson, J.F. Bell III et al., Earth Planet. Sci. Lett. **240**, 11–72 (2005)
A.N. Halliday, H. Wanke, J.L. Birck, R.N. Clayton, Space Sci. Rev. **96**, 197–230 (2001)
V.E. Hamilton, P.R. Christensen, Geology **33**, 433 (2005)
V.E. Hamilton, P.R. Christensen, H.Y. McSween et al., Meteorit. Planet. Sci. **38**, 871–885 (2003)
H. Harder, Geophys. Res. Lett. **27**(3), 301–304 (2000)
H. Harder, U.R. Christensen, Nature **380**, 507–509 (1996)
C.L. Harper, L.E. Nyquist, B. Bansal et al., Science **267**(5195), 213–217 (1995)
W.K. Hartman, G. Neukum, Space Sci. Rev. **96**, 165–194 (2001)
W.K. Hartmann, M.C. Malin, A.S. McEwen et al., Nature **397**, 586–589 (1999)
E. Hauber, S. van Gasselt, B. Ivanov et al., Nature **434**, 356–361 (2005)
E. Hauber, J. Bleacher, K. Gwinner et al., J. Volcanol. Geotherm. Res. **185**, 69–95 (2009)
E. Hauber, P. Brož, F. Jagert et al., Geophys. Res. Lett. **38**, L10201 (2011)
S.A. Hauck, R.J. Phillips, J. Geophys. Res. **107**(E7), 5052 (2002)

E.H. Hauri, T. Weinreich, A.E. Saal et al., Science **333**, 213–215 (2011)
J.W. Head, R. Greeley, M.P. Golombek et al., Space Sci. Rev. **96**, 263–292 (2001)
C.D.K. Herd, L.E. Borg, J.H. Jones, J.J. Papike, Geochim. Cosmochim. Acta **66**, 2025–2036 (2002)
C. Herzberg, P. Raterron, J. Zhang, Geochem. Geophys. Geosyst. **1**, 1051 (2000)
P.C. Hess, E.M. Parmentier, 32nd Annual Lunar and Planetary Science Conference, abstract 1319 (2001)
H. Hiesinger, J.W. Head, J. Geophys. Res. **109**, E01004 (2004)
H. Hiesinger, J.W. Head, G. Neukum, J. Geophys. Res. **112**, E05011 (2007)
M.M. Hirschmann, Annu. Rev. Earth Planet. Sci. **34**, 629–653 (2006)
M.M. Hirschmann, Geochem. Geophys. Geosyst. **1**, 1042 (2000)
G. Hirth, D.L. Kohlstedt, Earth Planet. Sci. Lett. **144**(1–2), 93–108 (1996)
C. Hodges, H. Moore, *Atlas of Volcanic Landforms on Mars*, US Geological Survey (1994)
T.M. Hoefen, R.N. Clark, J.L. Bandfield et al., Science **302**, 627–630 (2003)
T. Hoogenboom, S.E. Smrekar, Earth Planet. Sci. Lett. **248**(3–4), 830–839 (2006)
B.H. Horgan, J.F. Bell III, Geology **40**, 391–394 (2012)
W. Hsu, Y. Guan, H. Wang, Meteorit. Planet. Sci. **39**, 701–709 (2004)
G. Hulme, Geophys. J. R. Astron. Soc. **39**, 361–383 (1974)
B.M. Hynek, R.J. Phillips, R.E. Arvidson, J. Geophys. Res. **108**, 5111 (2003)
L. Iess, S. Giuliani, V. Dehant, Abstract EGU (2012)
P.J. Isaacson, C.M. Pieters, Icarus **210**, 8–13 (2009)
H. Iwamori, Geophys. Res. Lett. **19**, 309–312 (1992)
H. Iwamori, Earth Planet. Sci. Lett. **114**, 301–313 (1993)
R.A. Jacobson, Astron. J. **139**, 668–679 (2010)
W.L. Jaeger, L.P. Keszthelyi, A.S. McEwen et al., Science **317**, 1709 (2007)
E. Jagoutz, H. Wänke, Geochim. Cosmochim. Acta **50**, 939–953 (1986)
E. Jagoutz, A. Sorowka, J.D. Vogel, H. Wänke, Meteoritics **290**, 478–479 (1994)
R. Jaumann, G. Neukum, T. Behnke et al., Planet. Space Sci. **55**, 7–8, 928–952 (2007)
H.J. Jefffreys, Philos. Mag. **49**(6), 793–807 (1925)
J.R. Johnson, P.R. Christensen, P.G. Lucey, J. Geophys. Res. **107**(E6), 5035 (2002)
L.C. Kanner, J.F. Mustard, Icarus **187**, 442–456 (2007)
S. Karato, Nature **319**, 309–310 (1986)
S. Karato, *Deformation of Earth Materials: Introduction to the Rheology of the Solid Earth* (Cambridge University Press, Cambridge, 2008)
S. Karato, Rheological properties of minerals and rocks, in *Physics and Chemistry of the Deep Earth*, ed. by S. Karato (Wiley-Blackwell, New York, 2011)
S. Karato, H. Jung, Earth Planet. Sci. Lett. **157**, 193–207 (1998)
S. Karato, D. Wang, Electrical conductivity of minerals and rocks, in *Physics and Chemistry of the Deep Earth*, ed. by S. Karato (Wiley-Blackwell, New York, 2011)
S. Karunatillake, J.M. Keller, S.W. Squyres et al., J. Geophys. Res. **112**, E08S90 (2007)
S. Karunatillake, J.J. Wray, S.W. Squyres et al., J. Geophys. Res. **114**(E12), E12001 (2009)
S. Karunatillake, S.W. Squyres, O. Gasnault et al., J. Sci. Comput. **46**, 439–451 (2011)
R.F. Katz, M. Spiegelman, C.H. Langmuir, Geochem. Geophys. Geosyst. **4**(9), 1073 (2003)
T. Kawazoe, S. Karato, J. Ando et al., J. Geophys. Res. **115**, B08208 (2010). doi:10.1029/2009JB007096
T. Keller, P.J. Tackley, Icarus **202**(2), 429–443 (2009)
J.M. Keller et al., J. Geophys. Res. **111**, E03S08 (2006a)
J.M. Keller, W.V. Boynton, R.M.S. Williams et al., *Lunar and Planetary Science Conference*, abstract 2343 (2006b)
L. Kerber, J.W. Head, J.-B. Madelein et al., Icarus **216**, 212–220 (2011)
L. Keszthelyi, W. Jeager, A. McEwen et al., J. Geophys. Res. **113**, 4005 (2008)
L.P. Keszthelyi, W.L. Jaeger, C.M. Dundas et al., Icarus **205**, 211–229 (2010)
W.S. Kiefer, Meteorit. Planet. Sci. **38**(12), 1815–1832 (2003)
W.S. Kiefer, Earth Planet. Sci. Lett. **222**, 349–361 (2004)
W.S. Kiefer, Q. Li, Geophys. Res. Lett. **36**, L18203 (2009)
M. Knapmeyer, Planet. Space Sci. **59**, 1062–1068 (2011)
M. Knapmeyer, H.-P. Harjes, Geophys. J. Int. **143**, 1–21 (2000)
M. Knapmeyer, J. Oberst, E. Hauber et al., J. Geophys. Res. **111**(E11), E11006 (2006)
N. Kobayashi, K. Nishida, Nature **395**, 357–360 (1998)
W.C. Koeppen, V.E. Hamilton, J. Geophys. Res. **113**, E05001 (2008)
D.L. Kohlstedt, S.J. Mackwell, Z. Phys. Chem. **207**, 147–162 (1998)
N.I. Kömle, E.S. Hütter, W. Macher et al., Planet. Space Sci. **59**(8), 639–660 (2011)
A.S. Konopliv, S.W. Asmar, W.M. Folkner et al., Icarus **211**, 401–428 (2011)
J. Korenaga, Rev. Geophys. **46**, RG2007 (2008)

J. Korenaga, Geophys. J. Int. **179**, 154–170 (2009)
D.A. Kring, J.D. Gleason, T.D. Swindle et al., Meteorit. Planet. Sci. **38**, 1833–1848 (2003)
P. Kronberg, E. Hauber, M. Grott et al., J. Geophys. Res. **112**, E04005 (2007)
P. Kuchynka, W.M. Folkner, R.S. Park et al. DPS abstract 12-RC-598-AAS-DPS, DPS (2012)
I. Kushiro, Annu. Rev. Earth Planet. Sci. **29**, 71–107 (2001)
P.D. Lanagan, A.S. McEwen, L.P. Keszthelyi, T. Thodarson, Geophys. Res. Lett. **28**, 2365–2368 (2001)
N.P. Lang, L.L. Tornabene, H.Y. McSween, P.R. Christensen, J. Volcanol. Geotherm. Res. **185**, 103–115 (2009)
B. Langlais, M.E. Purucker, M. Mandea, J. Geophys. Res. **109**, E2 (2004)
J.K. Lanz, R. Wagner, U. Wolf et al., J. Geophys. Res. **115**, 12019 (2010)
T.J. Lapen, M. Righter, A.D. Brandon et al., Science **328**, 347–350 (2010)
J. Lasue et al., Space Sci. Rev. (2012, this issue). doi:10.1007/s11214-012-9946-5
S. Le Maistre, W.M. Folkner, P. Rosenblatt et al., *European Planetary Science Congress*. Extended abstract EPSC2010-191 (2010)
S. Le Maistre, P. Rosenblatt, A. Rivoldini et al., Planet. Space Sci. **68**(1), 105–122 (2012). doi:10.1016/j.pss.2011.12.020
A. Lenardic, F. Nimmo, L. Moresi, J. Geophys. Res. **109**, E02003 (2004)
R.C.F. Lentz, G.J. Taylor, A.H. Treiman, Meteorit. Planet. Sci. **34**, 919–932 (1999)
L.A. Leshin, Geophys. Res. Lett. **27**, 14 (2000)
L.A. Leshin, S. Epstein, E.M. Stolper, Geochim. Cosmochim. Acta **60**(14), 2635–2650 (1996)
K. Lewis, O. Aharonson, J.P. Grotzinger et al., J. Geophys. Res. **113**, E12S36 (2008)
Q. Li, W.S. Kiefer, Geophys. Res. Lett. **34**(16), L16203 (2007)
R.I. Lillis, H.V. Frey, M. Manga et al., Icarus **194**, 575–596 (2008)
R.J. Lillis, J. Dufek, J.E. Bleacher et al., J. Volcanol. Geotherm. Res. **185**, 123–138 (2009)
K. Litasov, E. Ohtani, Phys. Earth Planet. Inter. **134**, 105–127 (2002)
P. Lognonné, M. Le Feuvre, C.L. Johnson et al., J. Geophys. Res. **114**, E12003 (2009)
D. Loizeau, M. Mangold, F. Poulet, Icarus **205**, 396–418 (2010)
J.-P. Lorand, V. Chevrier, V. Sautter, Meteorit. Planet. Sci. **40**, 1257 (2005)
M.C. Malin, J.F. Bell, B.A. Cantor et al., J. Geophys. Res. **112**(E5), E05S04 (2007)
M. Manga, A. Patel, J. Dufek, E.S. Kyte, Geophys. Res. Lett. **39**, 1202 (2012)
N. Mangold, F. Poulet, J.F. Mustard et al., J. Geophys. Res. **112**(E11), E08S04 (2007)
N. Mangold, D. Loizeau, F. Poulet et al., Earth Planet. Sci. Lett. **294**, 440–450 (2010)
M.M. Marinova, O. Aharonson, E. Asphaug, Nature **453**(7199), 1216–1219 (2008)
S. Maurice, W. Feldman, B. Diez et al., J. Geophys. Res. **116**, E11008 (2011)
F.M. McCubbin, A. Smirnov, H. Nekvasil et al., Earth Planet. Sci. Lett. **292**(1–2), 132–138 (2010)
F.M. McCubbin, E.H. Hauri, S.M. Elardo et al., *LPSC 43*, abstract 1121 (2012)
A.S. McEwen, M. Malin, M. Carr, Nature **397**, 584–586 (1999)
A.S. McEwen, E.M. Eliason, J.W. Bergstrom et al., J. Geophys. Res. **112**(E5), E05S02 (2007)
P.J. McGovern, S.C. Solomon, D.E. Smith et al., J. Geophys. Res. **107**, E12 (2002)
P.J. McGovern, S.C. Solomon, D.E. Smith et al., J. Geophys. Res. **109**, E07007 (2004)
D. McKenzie, M.J. Bickle, J. Pet. **29**, 625–679 (1988)
S.M. McLennan, M.A. Sephton, C. Allen et al., *Planning for Mars Returned Sample Science: Final report of the MSR End-to-End International Science Analysis Group (E2E-iSAG)* (2011). The Mars Exploration Program Analysis Group (MEPAG) at http://mepag.jpl.nasa.gov/reports/, 101 pp.
M. McNutt, J. Geophys. Res. **89**, 11180–11194 (1984)
H.Y. McSween, Rev. Geophys. **23**, 391–416 (1985)
H.Y. McSween, Meteoritics **29**, 757–779 (1994)
H.Y. McSween, Meteorit. Planet. Sci. **36**, 7–25 (2002)
H.Y. McSween, A.H. Treiman, Martian meteorites, in *Planetary Materials*, ed. by J.J. Papike. Revs. Mineral., vol. 36, (1998), pp. 6–53
H.Y. McSween, T.L. Grove, R.C.F. Lentz et al., Nature **409**, 487–490 (2001)
H.Y. McSween et al., Science **305**, 842–845 (2004)
H.Y. McSween, S.W. Ruff, R.V. Morris et al., J. Geophys. Res. **111**, E09S91 (2006)
H.Y. McSween, S.W. Ruff, R.V. Morris et al., J. Geophys. Res. **113**, E06S04 (2008)
H.Y. McSween, G.J. Taylor, M.B. Wyatt, Science **324**, 736–739 (2009)
D. Mège, P. Masson, Planet. Space Sci. **44**, 1499–1546 (1996)
S. Mei, D.L. Kohlstedt, J. Geophys. Res. **105**(B9), 21471–21482 (2000a)
S. Mei, D.L. Kohlstedt, J. Geophys. Res. **105**(B9), 21457–21470 (2000b)
C. Meyer, *The Mars Meteorite Compendium*, Johnson Space Center contribution 27672. Houston, Texas, USA (2009). http://curator.jsc.nasa.gov/antmet/mmc/index.cfm
K. Mezger, V. Debaille, T. Kleine, Space Sci. Rev. (2012, this issue). doif:10.1007/s11214-012-9935-8

J.R. Michalski, R.L. Fergason, Icarus **199**, 24–48 (2009)
T. Mikouchi, M. Miyamoto, in *38th Lunar and Planetary Science Conference*, vol. 1343 (2002)
M.P. Milazzo, L.P. Keszthelyi, W.L. Jaeger et al., Geology **37**, 171–174 (2009)
D. Mimoun, P. Lognonné, W.B. Banerdt et al., *43rd Lunar and Planetary Science Conference*, abstract 1493 (2012a)
D. Mimoun, M. Wieczorek, L. Alkalai et al., Exp. Astron. (2012b). doi:10.1007/s10686-011-9252-3
K. Misawa, C.-Y. Shih, Y. Reese et al., Earth Planet. Sci. Lett. **246**(1–2), 90–101 (2006)
D.W. Mittlefehldt, Meteoritics **29**(2), 214–221 (1994)
A.G. Monders, E. Médart, T.L. Grove, Meteorit. Planet. Sci. **42**, 131–148 (2007)
L.G.J. Montési, M.T. Zuber, J. Geophys. Res. **108**, E6 (2003)
R.V. Morris, H.V. Lauer Jr., C.A. Lawson et al., J. Geophys. Res. **90**, 3126–3144 (1985)
R.V. Morris, G. Klingelhofer, C. Schroder et al., J. Geophys. Res. **113**, E12S42 (2008)
A. Morschhauser, M. Grott, D. Breuer, Icarus **212**(2), 541–558 (2011)
P.J. Mouginis-Mark, J.W. Head, L. Wilson, J. Geophys. Res. **87**, 9890–9904 (1982)
P.J. Mouginis-Mark, A.J.L. Harris, S.K. Rowland, M.G. Chapman (eds.), *Terrestrial Analogs to the Calderas of the Tharsis Volcanoes on Mars the Geology of Mars: Evidence from Earth-Based Analog* (Cambridge University Press, Cambridge, 2007), p. 71
S. Murchie, R. Arvidson, P. Bedini et al., J. Geophys. Res. **112**, E05S03 (2007)
D.S. Musselwhite, H.A. Dalton, W.S. Kiefer, A.H. Treiman, Meteorit. Planet. Sci. **41**(9), 1271–1419 (2006)
J.F. Mustard, J.M. Sunshine, Science **267**, 1623–1626 (1995)
J.F. Mustard, S. Erard, J.-P. Bibring et al., J. Geophys. Res. **98**, 3387–3400 (1993)
J.F. Mustard, S.L. Murchie, S. Erard, J.M. Sunshine, J. Geophys. Res. **102**, 25605–25615 (1997)
J.F. Mustard, F. Poulet, A. Gendrin et al., Science **307**, 1595–1597 (2005)
J.F. Mustard, S.L. Murchie, S.M. Pelkey et al., Nature **454**, 305–309 (2008)
J.F. Mustard, B.L. Ehlmann, S.L. Murchie et al., J. Geophys. Res. **114**(E13), E00D12 (2009)
B.O. Mysen, D. Virgo, R.K. Popp, C.M. Bertka, Am. Mineral. **83**, 942–946 (1998)
T. Nakagawa, P.J. Tackley, Earth Planet. Sci. Lett. **329–330**, 1–10 (2012)
N. Nakamura, D.M. Unruh, M. Tatsumoto, R. Hutchuson, Geochim. Cosmochim. Acta **46**, 155–1573 (1982)
G. Neukum, *Workshop on Mars Sample Return Science* (Lunar Planet. Inst., Houston, 1988), pp. 128-129
G. Neukum, K. Hiller, J. Geophys. Res. **86**, 3097–3121 (1981)
G. Neukum, B.A. Ivanov, in *Hazards due to Comets and Asteroids*, ed. by T. Gehrels et al.(University of Arizona Press, Tucson, 1994), pp. 359–416
G. Neukum, R. Jaumann, H. Hoffmann et al., Nature **432**, 971–979 (2004)
G. Neukum, A.T. Basilevsky, T. Kneissl et al., Earth Planet. Sci. Lett. **294**, 204–222 (2010)
G.A. Neumann, M.T. Zuber, M.A. Wieczorek et al., J. Geophys. Res. **109**, E08002 (2004)
H.E. Newsom, L.S. Crumpler, R.C. Reedy et al., J. Geophys. Res. **112**(E11), E03S12 (2007)
F. Nimmo, D. Stevenson, J. Geophys. Res. **105**(E5), 11969–11979 (2000)
F. Nimmo, K. Tanaka, Annu. Rev. Earth Planet. Sci. **33**, 133–161 (2005)
F. Nimmo, S.D. Hart, D.G. Korycansky et al., Nature **453**(7199), 1220–1223 (2008)
Y. Nishihara, D. Tinker, T. Kawazoe et al., Phys. Earth Planet. Inter. **170**, 156–169 (2008)
M.D. Norman, Meteorit. Planet. Sci. **34**, 439–449 (1999)
L.E. Nyquist, B.M. Bansal, H. Wiesmann, C.-Y. Shih, *26th Lunar and Planetary Institute Science Conference*, abstracts 1065 (1995)
L.E. Nyquist, D.D. Bogard, C.Y. Shih et al., Space Sci. Rev. **96**, 105–164 (2001)
J. Oberst, J. Geophys. Res. **92**(B2), 1397–1405 (1992)
A. Ody, F. Poulet, Y. Langevin et al., J. Geophys. Res. **117**, E00J14 (2012)
M. Ogawa, T. Yanagisawa, J. Geophys. Res. **116**, E08008 (2011)
E. Ohtani, N. Kamaya, Geophys. Res. Lett. **19**, 2239–2242 (1992)
R.D. Oldham, Q. J. Geol. Soc. Lond. **62**, 456–475 (1906)
R. Ostertag, D. Stoffler, in *Proceedings of 13th Lunar and Planetary Science Conference*, (1982), pp. 457–463
E.A. Parfitt, L. Wilson, *Fundamentals of Physical Volcanology* (Blackwell, Oxford, 2008), 230 pp.
J. Park, D.H. Garrison, D.D. Bogard, Geochim. Cosmochim. Acta **73**, 2177–2189 (2009)
E.M. Parmentier, M.T. Zuber, J. Geophys. Res. **112**, E02007 (2007)
R.J. Phillips, LPI Tech. Rep. 91-02 LPI/TR-91-02, pp. 35–38, Lunar Planet. Inst., Houston (1991)
R.J. Phillips, M.T. Zuber, S.C. Solomon et al., Science **291**, 2587–2591 (2001)
R.J. Phillips, M.T. Zuber, S.E. Smrekar et al., Science **320**(5880), 1182–1185 (2008)
S. Piqueux, P.R. Christensen, J. Geophys. Res. **114**, E09005 (2009a)
S. Piqueux, P.R. Christensen, J. Geophys. Res. **114**, E09006 (2009b)
T. Platz, G. Michael, Earth Planet. Sci. Lett. **312**, 140–151 (2011)
T. Platz, G. Michael, G. Neukum, Earth Planet. Sci. Lett. **293**, 388–395 (2010)

T. Platz, S. Münn, T.R. Walter et al., Earth Planet. Sci. Lett. **305**, 445–455 (2011)
J. Plescia, J. Geophys. Res. **109**, E03003 (2004)
B.T. Poe, C. Romano, F. Nestola, J.R. Smyth, Phys. Earth Planet. Inter. **181**, 3–4 (2010)
H.N. Pollack, S.J. Hurter, J.R. Johnson, Rev. Geophys. **31**(3), 267–280 (1993)
F. Poulet, J.-P. Bibring, J.F. Mustard et al., Nature **438**, 623–627 (2005)
F. Poulet, C. Gomez, J.-P. Bibring et al., J. Geophys. Res. **112**, E08S02 (2007)
F. Poulet, J.-P. Bibring, Y. Langevin et al., Icarus **201**, 69–83 (2009a)
F. Poulet, N. Mangold, B. Platevoet et al., Icarus **201**, 84–101 (2009b)
F. Poulet, D.W. Beaty, J.-P. Bibring et al., Astrobiology **9**, 3 (2009c)
M.S. Ramsey, P.R. Christensen, J. Geophys. Res. **103**, 577–596 (1998)
C.C. Reese, V.S. Solomatov, L.N. Moresi, J. Geophys. Res. **103**(E6), 13643–13658 (1998)
C.C. Reese, C.P. Orth, V.S. Solomatov, J. Geophys. Res. **115**(E5), E05004 (2010)
R. Rieder, T. Economou, H. Wänke et al., Science **278**, 1771–1774 (1997)
J.A. Ritzer, S.A. Hauck, Icarus **201**(2), 528–539 (2009)
A. Rivoldini, T.V. Hoolst, O. Verhoeven et al., Icarus **213**, 451–472 (2011)
S.J. Robbins, G.D. Achille, B.M. Hynek, Icarus **211**, 1179–1203 (2011)
J.H. Roberts, S. Zhong, J. Geophys. Res. **111**(E6), E06013 (2006)
G.P. Roberts, B. Matthews, C. Bristow et al., J. Geophys. Res. **117**, E02009 (2012)
P. Rochette, J.P. Lorand, G. Fillion et al., Meteorit. Planet. Sci. **36**, 176 (2001)
P. Rochette, J. Gattacceca, V. Chevrier et al., Meteorit. Planet. Sci. **40**, 529 (2005)
A.D. Rogers, P.R. Christensen, J. Geophys. Res. **112**, E01003 (2007)
C. Romano, B.T. Poe, N. Kreidie et al., Am. Mineral. **91**(8–9), 1371–1377 (2006)
C. Romano, B.T. Poe, J. Tyburczy et al., Eur. J. Mineral. **21**(3), 615–622 (2009)
F. Roosbeek, Celest. Mech. Dyn. Astron. **75**, 285–300 (2000)
S.W. Ruff, P.R. Christensen, D.L. Blaney et al., J. Geophys. Res. **111**, E12S18 (2006)
J. Ruiz, C. Fernández, D. Gomez-Ortiz et al., Earth Planet. Sci. Lett. **270**(1-2), 1–12 (2009)
J. Ruiz, P.J. McGovern, A. Jiménez-Díaz et al., Icarus **215**(2), 508–517 (2011)
S.E.H. Sakimoto, J. Crisp, S.M. Baloga, J. Geophys. Res. **102**, 6597–6614 (1997)
J.W. Salisbury, J.W. Eastes, Icarus **64**, 586–588 (2008)
M.R. Salvatore, J.F. Mustard, M.B. Wyatt et al., J. Geophys. Res. **115**(E14), E07005 (2010)
V. Sautter, M.J. Toplis, J.P. Lorand, M. Macri, Meteorit. Planet. Sci. (2012)
G.G. Schaber, K.L. Tanaka, J.K. Harmon, in *Lunar and Planetary Science Conference*. LPI Contribution, vol. 441, Houston, TX (1981)
M.E. Schmidt, T.J. McCoy, Earth Planet. Sci. Lett. **296**(1–2), 67–77 (2010)
B. Schott, A.P. van den Berg, D.A. Yuen, Geophys. Res. Lett. **28**(22), 4271–4274 (2001)
C. Schröder, D.S. Rodionov, T.J. McCoy et al., J. Geophys. Res. **113**, E06S22 (2008)
G. Schubert, R.E. Lingenfelter, Nature **242**(5395), 251–252 (1973)
G. Schubert, T. Spohn, J. Geophys. Res. **95**(B9), 14095–14104 (1990)
G. Schubert, P. Cassen, R.E. Young, Icarus **38**, 192–211 (1979)
R.A. Schultz, T.R. Watters, Geophys. Res. Lett. **28**, 4659–4662 (2001)
S. Schumacher, D. Breuer, J. Geophys. Res. **111**(E2), E02006 (2006)
S. Schumacher, D. Breuer, Geophys. Res. Lett. **34**(14), L14202 (2007)
S. Schumacher, T.E. Zegers, Icarus **211**, 305–315 (2011)
D. Scott, K. Tanaka, Icarus **45**, 304–319 (1981)
D.H. Scott, K.L. Tanaka, R. Greeley, J.E. Guest, US Geol. Surv. Misc. Invest. Ser. Map, I-1802-A (1986)
D.H. Scott, K.L. Tanaka, R. Greeley, J.E. Guest. US Geol. Surv. Misc. Invest. Ser. Map, I-1802-B (1987a)
D.H. Scott, K.L. Tanaka, R. Greeley, J.E. Guest. US Geol. Surv. Misc. Invest. Ser. Map, I-1802-C (1987b)
M.N. Simon, L.M. Carter, B.A. Campbell et al., *Lunar Planet. Sci., XLIII*, abstract 1595 (2012)
R.B. Singer, T.B. McCord, R.N. Clark, J. Geophys. Res. **84**, 8415–8426 (1982)
J.R. Skok, J.F. Mustard, S.L. Murchie et al., J. Geophys. Res. **115**, E00D14 (2010)
N.H. Sleep, J. Geophys. Res. **99**(E3), 5639–5655 (1994)
J.L. Smellie, L.G. Chapman (eds.), *Volcano-Ice Interaction on Earth and Mars*, vol. 202 (Geological Society Special Publication, London, 2002)
D.E. Smith, M.T. Zuber, S.C. Solomon et al., Science **284**(5419), 1495 (1999)
F. Sohl, T. Spohn, J. Geophys. Res. **102**, 1613–1635 (1997)
F. Sohl, G. Schubert, T. Spohn, J. Geophys. Res. **110**, E12008 (2005)
V.S. Solomatov, L.N. Moresi, Geophys. Res. Lett. **24**(15), 1907–1910 (1997)
S.C. Solomon, O. Aharonson, J.M. Aurnou et al., Science **307**(5713), 1214–1220 (2005)
C.P. Sonett, D.S. Colburn, P. Dyal et al., Nature **230**, 359–362 (1971)
T. Spohn, Icarus **90**, 222–236 (1991)
T. Spohn, M. Grott, J. Knollenberg et al., *43rd Lunar and Planetary Science Conference*, abstract 1445 (2012)

S.W. Squyres, D.E. Wilhelms, A.C. Moosman, Icarus **70**, 385–408 (1987)
S.W. Squyres, R.E. Arvidson, E.T. Baumgartner et al., J. Geophys. Res. **108**(E12), 8062 (2003)
S.W. Squyres, R.E. Arvidson, J.F. Bell III et al., Science **305**(5685), 794–799 (2004a)
S.W. Squyres, R.E. Arvidson, J.F. Bell III et al., Science **306**(5702), 1698–1703 (2004b)
S.W. Squyres, O. Aharonson, B.C. Clark et al., Science **316**, 5825, 738 (2007)
O. Šrámek, S. Zhong, J. Geophys. Res. **115**(E9), E09010 (2010)
O. Šrámek, S. Zhong, J. Geophys. Res. **117**, E01005 (2012)
I.M. Steele, J.V. Smith, in *13th Lunar Plan. Sci. Conf.*, Houston, TX, March 15–19 (1982), pp. A375–A384
D.J. Stevenson, T. Spohn, G. Schubert, Icarus **54**, 466–489 (1983)
K.R. Stockstill-Cahill, F.S. Anderson, V.E. Hamilton, J. Geophys. Res. **113**(E12), E07008 (2008)
R.M. Suggs, W.J. Cooke, R.J. Suggs et al., Earth Moon Planets **102**, 293–298 (2008)
R. Sullivan, R. Arvidson, J.F. Bell III et al., J. Geophys. Res. **113**, E06S07 (2008)
J.M. Sunshine, C.M. Pieters, J. Geophys. Res. **98**, 9075–9087 (1993)
J.M. Sunshine, C.M. Pieters, S.F. Pratt, J. Geophys. Res. **95**, 6955–6966 (1990)
E. Takahashi, J. Geophys. Res. **95**(B10), 15941–15954 (1990)
K.L. Tanaka, J. Geophys. Res. **91**, E139–E158 (1986)
K.L. Tanaka, D.H. Scott, R. Greeley, in *Mars* (University of Arizona Press, Tucson, 1992), pp. 345–382
G.J. Taylor, W. Boynton, J. Brückner et al., J. Geophys. Res. **111**(E3), E03S10 (2006)
G.J. Taylor, L.M.V. Martel, S. Karunatillake et al., Geology **38**, 183–186 (2010)
N.A. Teanby, J. Wookey, Phys. Earth Planet. Inter. **186**, 70–80 (2011)
L.L. Tornabene, J.E. Moersch, H.Y. McSween et al., J. Geophys. Res. **113**(E12), E10001 (2008)
P. Toulmin III, A.K. Baird, B.C. Clark et al., J. Geophys. Res. **82**(28), 4625–4634 (1977)
A.H. Treiman, Meteorit. Planet. Sci. **38**(12), 1849–1864 (2003)
A. Treiman, Chem. Erde **65**, 203–296 (2005)
A.H. Treiman, M.J. Drake, M.-J. Janssens et al., Geochim. Cosmochim. Acta **50**, 1071–1091 (1986)
T. Usui, H.Y. McSween, C. Floss, Geochim. Cosmochim. Acta **72**(6), 1711–1730 (2009)
J.A. Van Orman, T.L. Grove, N. Shimizu, Earth Planet. Sci. Lett. **160**, 505–519 (1998)
J. Vaucher, D. Baratoux, N. Mangold et al., Icarus **204**, 418–442 (2009)
O. Verhoeven, A. Rivoldini, P. Vacher et al., J. Geophys. Res. **110**, E04009 (2005)
M. Wadhwa, H.Y.J. McSween, G. Crozaz, Geochim. Cosmochim. Acta **58**, 4213–4229 (1994)
G.P.L. Walker, R. Croasdale, Bull. Volcanol. **35**, 303–317 (1971)
H. Wänke, G. Dreibus, Philos. Trans. R. Soc. Lond. A **349**, 285–293 (1994)
N.H. Warner, T.K.P. Gregg, J. Geophys. Res. **108**, 5112 (2003)
L.L. Watson, I.D. Hutcheon, S. Epstein, E.M. Stolper, Science **265**(5158), 86–90 (1994)
S.A. Weinstein, J. Geophys. Res. **100**(E6), 11719–11728 (1995)
B.P. Weiss, I. Garrick-Bethell, J.L. Kirschvink, *Workshop on Ground Truth from Mars: Science Payoff from a Sample Return Mission*. LPI Contribution No. 1401, abstract #4024 (2008)
M.J. Wenzel, M. Manga, A.M. Jellinek, Geophys. Res. Lett. **31**(4), L04702 (2004)
S.C. Werner, Icarus **195**, 45–60 (2008)
S.C. Werner, Icarus **201**, 44–68 (2009)
S.M. White, J.A. Crisp, F.J. Spera, Geochem. Geophys. Geosyst. **7**, Q03010 (2006)
J.L. Whitford-Stark, Earth-Sci. Rev. **18**, 109–168 (1982)
M.A. Wieczorek, Icarus **196**, 506–517 (2008)
M.A. Wieczorek, M.T. Zuber, J. Geophys. Res. **109**, E01009 (2004)
D.E. Wilhelms, S.W. Squyres, Nature **309**, 138–140 (1984)
D.A. Williams, R. Greeley, W. Zuschneid et al., J. Geophys. Res. **112**, E10004 (2007)
D.A. Williams, R. Greeley, S.C. Werner et al., J. Geophys. Res. **113**, E11005 (2008)
D.A. Williams, R. Greeley, R. Fergason et al., Planet. Space Sci. **57**, 895–916 (2009)
D.A. Williams, R. Greeley, L. Manfredi et al., Earth Planet. Sci. Lett. **294**, 451–465 (2010)
L. Wilson, J. Geophys. Res. **106**, 1423–1434 (2001)
L. Wilson, J.W. Head, Nature **302**, 663–668 (1983)
L. Wilson, J.W. Head, Rev. Geophys. **32**, 221–263 (1994)
L. Wilson, J.W. Head, J. Geophys. Res. **107**, 5057 (2002)
L. Wilson, J.W. Head, J. Volcanol. Geotherm. Res. **163**, 83–97 (2007)
D.U. Wise, M.P. Golombek, G.E. McGill, J. Geophys. Res. **84**, 7934–7939 (1979)
J.J. Wray, E.Z. Noe Dobrea, R.E. Arvidson et al., Geophys. Res. Lett. **36**, L21201 (2009)
M.B. Wyatt, H.Y. McSween, Nature **417**, 263–266 (2002)
L. Xiao, J. Huang, P.R. Christensen et al., Earth Planet. Sci. Lett. **323–324**, 9–18 (2012)
Y.S. Xu, B.T. Poe, T.J. Shankland et al., Science **280**(5368), 1415–1418 (1998)
Y.S. Xu, T.J. Shankland, B.T. Poe, J. Geophys. Res. **105**(B12), 27865–27875 (2000)
X. Yang, Earth Planet. Sci. Lett. **317–318**, 241–250 (2012)

T. Yoshino, T. Matsuzaki, S. Yamashita, T. Katsura, Nature **443**, 973–976 (2006)
T. Yoshino, T. Matsuzaki, A. Shatskiy, T. Katsura, Earth Planet. Sci. Lett. **288**, 291–300 (2009)
M. Yseboodt, J.-P. Barriot, V. Dehant, J. Geophys. Res. **108**, 5076 (2003)
J. Zhang, C. Herzberg, J. Geophys. Res. **99**(B9), 17729–17742 (1994)
Y.-H. Zhao, M.E. Zimmerman, D.L. Kohlstedt, Earth Planet. Sci. Lett. **287**, 229–240 (2009)
V.N. Zharkov, T.V. Gudkova, Planet. Space Sci. **45**, 401–407 (1997)
S. Zhong, Nat. Geosci. **2**, 19–23 (2009)
S. Zhong, M.T. Zuber, Earth Planet. Sci. Lett. **189**(1–2), 75–84 (2001)
L. Zhu, H. Kanamori, J. Geophys. Res. **105**, 2969–2980 (2000)
J.R. Zimbelman, J. Geophys. Res. **90**, 157–162 (1985)
J.R. Zimbelman, T.K.P. Gregg (eds.), *Environmental Effects on Volcanic Eruptions* (Kluwer Academic/Plenum, New York, 2000), 206 pp.
J. Zipfel, C. Schröder, B.L. Jolliff et al., Meteorit. Planet. Sci. **46**, 1–20 (2011)
M.T. Zuber, S.C. Solomon, R.J. Phillips et al., Science **287**, 1788–1793 (2000)